APPROVAL SHEET

Title of Dissertation: Photolytic fate of organo-selenium and -tin compounds in natural and engineered water systems

Name of Candidate: Mamatha Hopanna
Doctor of Philosophy, 2021

Dissertation and Abstract Approved: _____
Lee Blaney, Ph.D.
Associate Professor
Department of Chemical, Biochemical, and Environmental Engineering

Date Approved: _____

NOTE:*The Approval Sheet with the original signature must accompany the thesis or dissertation. No terminal punctuation is to be used.

CURRICULUM VITAE

Name:	Mamatha Hopanna
Degree and date to be conferred:	Ph.D., 2021
Secondary education:	May 2003 Government Science College Salagame Road, Hassan, Karnataka, India 573201.
Collegiate institutions attended:	Aug 2003- May 2008 Malnad College of Engineering, Karnataka Bachelor of Technology (Civil Engineering) Aug 2014- Aug 2015 (transferred to doctoral degree) University of Maryland Baltimore County Master of Science (Environmental Engineering) Aug 2015- Aug 2021 University of Maryland Baltimore County Doctor of Philosophy (Environmental Engineering)
Major:	Environmental Engineering
Professional publications:	Hopanna, M.; Kelly, L.; Blaney, L., Photochemistry of the organoselenium compound ebselen: direct photolysis and reaction with active intermediates of conventional reactive species sensitizers and quenchers. *Environmental Science & Technology* 2020, *54 (18), 11271-11281*

Chen, S.; Blaney, L.; Chen, P.; Deng, S.; Hopanna, M.; Bao, Y.; Yu, G., Ozonation of the 5-fluorouracil anticancer drug and its prodrug capecitabine: Reaction kinetics, oxidation mechanisms, and residual toxicity. *Frontiers of Environmental Science & Engineering* 2019, *13*, (4), 59.

Hopanna, M.; Mangalgiri, K.; Ibitoye, T.; Ocasio, D.; Snowberger, S.; Blaney, L., Chapter 8 - UV-254 transformation of antibiotics in water and wastewater treatment processes. In *Contaminants of Emerging Concern in Water and Wastewater*, Hernández-Maldonado, A. J.; Blaney, L., Eds. Butterworth-Heinemann: 2020; pp 239-297

Snowberger, S.; Adejumo, H.; He, K.; Mangalgiri, K. P.; Hopanna, M.; Soares, A. D.; & Blaney, L., Direct photolysis of fluoroquinolone antibiotics at 253.7 nm: Specific reaction kinetics and formation of equally-potent fluoroquinolone antibiotics. *Environmental Science & Technology* 2016 50(17), 9533–9542.

Professional positions held:

Graduate Assistant (Aug 2015- Aug 2021)
University of Maryland Baltimore County
1000 Hilltop Circle
Baltimore MD 21250.

Junior Engineer (June 2007-May 2008)
Customer Support and Structural Design Department
Confident Group, India

ABSTRACT

Title of Document:	PHOTOLYTIC FATE OF ORGANO-SELENIUM AND -TIN COMPOUNDS IN NATURAL AND ENGINEERED WATER SYSTEMS
	Mamatha Hopanna Doctor of Philosophy, 2021
Directed By:	Dr. Lee Blaney, Associate Professor Department of Chemical, Biochemical and Environmental Engineering

Organometallic chemicals contain at least one metal atom covalently bound to at least one carbon atom. Due to their sorption, redox, and catalysis properties, organometallics are commonly used as antibiotics, antioxidants, chemotherapy agents, pesticides, and semiconductors in the biomedical, agricultural, and electrical fields. While photochemical degradation is a significant abiotic process that governs the fate of organic pollutants in water, few studies have elucidated the photochemical transformation of organometallics in natural (*i.e.,* 365 nm) and engineered (*i.e.*, 254 nm) systems.

This dissertation (i) assessed the suitability of conventional protocols, which are employed to study the photochemistry of organic contaminants, for organometallics, (ii) measured quantum yields for direct photolysis of organometallics, specifically organo-selenium and -tin, at 254 nm and 365 nm, (iii) determined the second-order rate constants for the reaction of organometallic chemicals with the singlet oxygen ($^1O_2$), hydroxyl radical ($^{\bullet}OH$), and triplet state dissolved organic matter ($^3DOM^*$) reactive species, (iv) the half-lives of organometallics in diverse water sources using the Aqueous Photochemistry of Environmentally occurring Xenobiotics (APEX) modeling tool, and (v) identified the

primary photoproducts and toxicity of organometallics in the UV-254 and UV-H_2O_2 treatment systems.

Atypical phototransformation kinetics were observed for ebselen in the presence of reactive species sensitizers, scavengers, and quenching agents due to ebselen reaction with active intermediates that are not kinetically relevant for most organic contaminants. These findings confirmed that the selenium atom leads to the high photoreactivity of ebselen and informed proper protocols for future study of organoselenium compounds. Triphenyltin hydroxide exhibited negligible direct photolysis at 365 nm, and indirect photolysis by $^1O_2$, $^\bullet$OH, and $^3DOM^*$ were the dominant photodegradation mechanisms. The second-order rate constants for triphenyltin hydroxide reaction with $^1O_2$, $^\bullet$OH, and $^3DOM^*$ were $(3.9 \pm 0.5) \times 10^6$ M^{-1} s^{-1}, $(7.81 \pm 0.37) \times 10^8$ M^{-1} s^{-1}, and $(1.41 \pm 0.06) \times 10^6$ M^{-1} s^{-1}, respectively. APEX model simulations indicated that the of triphenyltin hydroxide half-lives were as follows: 126-262 d in surface water; 77-178 d in wastewater effluent; 55-126 d in stormwater; 51-78 d in wetlands; and, 106-202 d in natural organic matter extracts.

In summary, this dissertation reports critical knowledge on the complex photochemical behavior of ebselen and triphenyltins for UV-254, advanced oxidation systems, and the natural environment. The information reported in this dissertation will assist with (i) understanding the fate of organometallics in natural systems and current water/ wastewater treatment processes and (ii) selecting appropriate photochemical and photocatalytic treatment systems for legacy and emerging organometallic chemicals.

PHOTOLYTIC FATE OF ORGANO-SELENIUM AND -TIN COMPOUNDS IN NATURAL AND ENGINEERED WATER SYSTEMS

By

Mamatha Hopanna

Dissertation submitted to the Faculty of the Graduate School of the
University of Maryland, Baltimore County, in partial fulfillment
of the requirements for the degree of
Doctor of Philosophy
2021

Dedication

This dissertation is dedicated to my daughters, Sana and Hansa.

Acknowledgments

The path towards my doctorate degree has been gratifying. It would be tough to name all the people who have nurtured and helped me during this journey.

I want to begin by expressing deep gratitude to my advisor, Dr. Lee Blaney, for believing in me and giving me a chance to pursue a PhD. I greatly appreciate his dedication to mentorship, which helped me identify my strengths and shortcomings to grow to be the confident researcher I am today. His insightful approach to science has challenged me to expand my ways of thinking through problems. His excellence as an advisor is matched by his empathy, kindness, and generosity, by which he makes his lab a great place to work.

I am grateful to Dr. Brian Reed for his encouragement, which was catalyst to my transfer from the master's program to PhD program. I want to thank Dr. Lisa Kelly for providing access to her lab to use transient absorption spectrometer and helpful advice on several aspects of this dissertation. I want to thank Dr. Brian Reed and Dr. Christopher Hennigan for their time in serving as readers on my committee. I want to thank Dr. Upal Ghosh for serving on my committee and his counsel on professional development. Thanks to Dr. Danmeng Shuai for valuable feedback and timely help in the completion of this dissertation. I am always grateful for the consistent encouragement and support from my committee members, and they have been critical to my success in this work.

I thank members of the Blaney lab, past and present, for creating a fantastic working atmosphere. Ke and Kiran, my mentors in the lab, could not have gained the core knowledge to finish my dissertation without them. Utsav for friendship and always being listening ears. Mike, for being a great support in exploring my future career options. I also sincerely appreciate Ethan, Michael, Jahir, Temi, and Laura, for their support, assistance, and help. I have learned from each of them, and I would not have accomplished this without your contribution.

Many thanks to my colleagues, past and present, in the CBEE department and all my friends at UMBC. To all the beautiful friendships I have gained- Nuzhat, Narendra, Shradha, Vineet, and Jyotsna, you are all the pillars of my strength. I cherish the time spent with you all. I truly appreciate the support and kindness you have shown in my time here.

I want to acknowledge all the CBEE department faculty and staff members, past and present, for their assistance and guidance, and encouragement at every stage of this journey. I specially thank Andrea and Victor for their consistent help and support.

I am also grateful to my family and friends back in India. Thank you, appaji and amma, for believing that l can achieve anything and providing unconditional support. I want to thank my loving and supportive husband, Dileep, and our lovely daughters, Sana and Hansa. They are the most important motivation to pursue this degree, and their

unconditional and encompassing love carries me through every up and down I encounter. Thank you for loving me, cheering with me, and appreciating life with me.

Contents

List of Tables

List of Figures

Chapter 1 Introduction

1.1 Background

The first organometallic chemical, tetramethyldiarsine (Cacodyl), was synthesized by Louis Claude Cadet in 1760 [1]. While a number of other organometallics were produced in the subsequent decades, the remarkable growth of organometallic chemistry did not begin until the twentieth century. Since that time, organometallics have made a significant contribution to scientific progress due to their numerous applications in the catalysis, agricultural, and pharmaceutical industries [2], as evidenced by the Nobel laureates in chemistry from 1912 (Victor Grignard and Paul Sabatier for the discovery of Grignard reagent), 1963 (Karl Ziegler and Giulio Natta for their work on polymers using aluminum catalysts), 1973 (Geoffrey Wilkinson and Ernst Otto Fischer for pioneering work on the chemistry of organometallics), and 2005 (Yves Chauvin, Robert Grubbs, and Richard Schrock for the development of the metathesis method in organic synthesis) [3]. This research paved the way for the introduction of synthetic organometallic compounds into consumer, agricultural, and industrial products starting in the 1960s [4].

Organometallic compounds are molecules that contain one or more metal atoms covalently bound to an organic moiety. This concept has been expanded to include non-metallic elements with metallic properties, such as boron, silicon, arsenic, selenium, and tellurium, by redefining organometallics as compounds that contain a carbon atom bound to a more electropositive element [5]. These chemicals exhibit unique sorption, redox, and catalysis reactions due to the presence of the organic moiety and metal atom [6]. In

addition, organometallics are commonly used as antibiotics [7-9], chemotherapy agents [10,11], antioxidants [12-15], pesticides [16-20], and semiconductors [21]. This dissertation examined the environmental photochemistry of two classes of organometallic chemicals, namely organoselenium and organotin. The specific compounds of interest included ebselen and triphenyltin hydroxide.

The organoselenium compound ebselen is an emerging pharmaceutical that has drawn interest due to its antioxidant, anti-inflammatory, anti-atherosclerotic, and cytoprotective properties [13,22]. Ebselen is a multifunctional chemical that protects cells from oxidative and free radical damage by catalyzing the reduction of reactive oxygen species [14]. The pharmacological relevance of ebselen was elucidated in 1984 when glutathione peroxidase like-activity was first reported by Muller *et al.* [23]. Since then, numerous studies have investigated the pharmacological and biochemical properties of ebselen, highlighting potential applications for treatment of malaria, tuberculosis, reperfusion injury, stroke, hearing loss, bipolar disorder, and multidrug-resistant *Staphylococcus aureus* [24-27]. A number of recent studies have suggested the potential therapeutic use of ebselen for COVID-19 and other respiratory viral infections [28-30]. Overall, the increased interest and use of organoselenium chemicals in organic synthesis and biological, pharmaceutical, and catalysis applications will result in the environmental release of these unique molecules.

Although ebselen has potential pharmacological benefits, this organoselenium chemical is also known to cause cellular toxicity. At elevated concentrations, ebselen induces

cytotoxicity, necrotic cell death, DNA damage, genotoxicity, and apoptosis [31-34]. For example, Meotti *et al.*[35] reported the half-maximal lethal doses of ebselen in rats and mice to be 400 and 340 μmol kg^{-1}, respectively. Due to bioaccumulation of selenium in the food chain and chronic toxicity that can cause reproductive deformities in aquatic organisms, the US Environmental Protection Agency (EPA) developed a new national chronic aquatic life criterion for selenium under the Clean Water Act [36]. In addition, inorganic selenium, such as selenite and selenate, exerts adverse acute and chronic effects on fish and wildlife at concentrations of 1-5 μg L^{-1} [37,38]. Cell-based metabolic studies have suggested that selenium is not released from ebselen [14], but the abiotic fate of organoselenium compounds is unknown. For this reason, the fate of ebselen in engineered (*e.g.*, water/wastewater treatment) and natural systems (*e.g.*, sunlit surface waters) warrants investigation.

Chemicals in the second class of organometallics of interest, namely organotins, are used as biocides, fungicides, insecticides, miticides for wood preservation and crop protection, industrial catalysts, and polyvinyl chloride stabilizers [39,40]. In addition, organotins have been used in antifouling paints for shipyards, marine structures, and ship hulls since the 1960s to inhibit the growth of barnacles, mussels, and snails [41,42]. The tri-substituted organotin compounds, such as tributyltin and triphenyltin, exert major toxicological effects in aquatic organisms and humans [42]. At nanomolar concentrations, tributyltins and triphenyltins cause acute and chronic toxicity, as well as developmental malformations and endocrine disruption in non-target species like algae, zooplankton, mollusks, and fish

larvae [18]. Moreover, triphenyltin chemicals cause reproductive toxicity in mammals and are potential endocrine disruptors in humans [43].

Due to the detrimental effects on non-target organisms, Japan, Germany, the United States, and other countries implemented restrictions on the use of tributyltin and triphenyltin as antifouling agents [44]. In 2001, the International Maritime Organization issued a convention on the Control of Harmful Anti-fouling Systems on Ships to prohibit the application of organotin compounds as antifouling paints on marine vessels. This convention went into effect in January 2008. About two years later (July 2010), the European Union limited the use of organotins in consumer goods to concentrations of less than or equal to 0.1% (g Sn/g) [45,46]. The US EPA placed triphenyltin hydroxide on the Contaminant Candidate List 4 [47] and classified it as a Category B2 carcinogen (*i.e.*, probable human carcinogen with adequate evidence from animal studies).

Despite regulatory pressure to reduce tributyltin pollution in some areas, triphenyltin chemicals are still used as biocides in both mariculture and agriculture [48]. Currently, 16 products that contain triphenyltin hydroxide are registered as pesticides by the US EPA [49]. Application of those pesticides introduces organotins to the environment. In fact, triphenyltin chemicals have been detected in surface water, sediment, marine organisms, and even human bodies [40]. Shiraishi *et al.* highlighted that triphenyltin concentrations in marine organisms are higher than those of tributyltin chemicals, even though 10× more tributyltins are produced each year [48,50]. Due to widespread use, toxicity, persistence, and

potential for human exposure, the fate of triphenyltin chemicals needs to be established in engineered and natural systems.

1.2 Problem Statement

Organic contaminants are released into the environment via various routes. For instance, herbicides, fungicides, and insecticides are directly released to the environment during application to fields, while pharmaceuticals mainly enter the environment through discharge of municipal and industrial wastewater effluent. The rising demand for organometallic chemicals is expected to result in a proportional increase in the environmental loading of these contaminants. The environmental fate of organometallics strongly depends on their chemical and physicochemical properties. Unlike conventional organic compounds, organometallics have unique properties that suggest complex environmental chemistry. For example, environmental degradation processes may release inorganic metals that are more toxic than the original organometallic compound [9,51]. Due to their intrinsic toxicity, biodegradation of organometallics in the environment is a negligible reaction pathway, thereby implicating the critical role of abiotic transformation processes. Photochemical reactions are the primary abiotic processes that govern the fate of organic contaminants in surface water [52]; however, few studies have elucidated the photochemical transformation mechanisms, kinetics, and products of organometallic chemicals in engineered and natural systems.

1.3 Research Objectives

This dissertation evaluated the photochemical transformation of organometallic compounds in engineered and natural water systems. We hypothesized that (i) the presence of metal atoms in these unique organic molecules would increase photoreactivity and (ii) both direct and indirect photolysis mechanisms would be kinetically relevant. Therefore, experiments were designed to determine the contributions of direct photolysis (*i.e.*, 254 nm, 365 nm), indirect photolysis (*i.e.*, reaction with singlet oxygen ($^1O_2$), hydroxyl radicals ($^\bullet OH$), and triplet dissolved organic matter ($^3DOM^*$)), and advanced systems (*i.e.,* UV-H_2O_2 advanced oxidation) to the transformation of organo-selenium and -tin compounds through mechanistic evaluation of the photochemical reaction kinetics. The dissertation had three major objectives with multiple sub-tasks, as indicated below.

1.) Photochemistry of the organoselenium compound ebselen: direct photolysis and reaction with active intermediates of conventional reactive species sensitizers and quenchers
    a.) Determine direct photolysis kinetics of ebselen and its carbon analog at 254 nm (representative of water/wastewater treatment) and 365 nm (representative of solar irradiation)
    b.) Investigate the photochemical reactivity of ebselen with $^1O_2$ and $^\bullet OH$ sensitizers
    c.) Evaluate the effects of reactive species scavenging and quenching agents on the photochemical reaction kinetics of ebselen

2.) Photolysis of triphenyltin chemicals: determination of rate constants and prediction of photodegradation in different source waters

   a.) Measure the phototransformation kinetics of triphenyltin hydroxide by direct photolysis with solar light and indirect photolysis by reaction with $^{1}O_2$, $^{\bullet}OH$, and $^{3}DOM^{*}$

   b.) Employ the Aqueous Photochemistry of Environmentally-occurring Xenobiotics (APEX) model to predict the half-life of triphenyltin hydroxide in different water sources

   c.) Identify the contributions of the direct photolysis, $^{1}O_2$, $^{\bullet}OH$, and $^{3}DOM^{*}$ reaction mechanisms to the overall degradation of triphenyltin hydroxide in various waters

3.) Photochemical fate of triphenyltin pesticides in engineered treatment systems: Reaction kinetics, transformation products, and residual toxicity

   a.) Determine the fate of triphenyltin hydroxide in photochemical water and wastewater treatment processes, including UV-254 and UV-H_2O_2 advanced oxidation

   b.) Identify the influence of water quality parameters, including solution pH, ionic strength, and DOM content, on triphenyltin hydroxide photochemistry

   c.) Characterize the primary photoproducts of triphenyltin hydroxide and confirm the corresponding reaction mechanisms

   d.) Establish the residual toxicity of triphenyltin hydroxide photoproducts formed during UV-254 and UV-H_2O_2 treatment

1.4 Organization of this Dissertation

The above objectives were accomplished through the research reported in Chapters 2-4 of this dissertation. Figure 1.1 illustrates the organizational scheme of the dissertation, and a brief synopsis of each chapter is provided below. To address the proposed hypotheses, the dissertation was organized to answer the following questions: (i) can previously reported protocols used to determine the photochemical fate of organic contaminants be applied to organometallics?; (ii) does the photolytic fate of organometallic chemicals vary in different water sources contaminated by organometallics?; and, (iii) should conventional or advanced photochemical processes be used to treat organometallics in engineered systems?

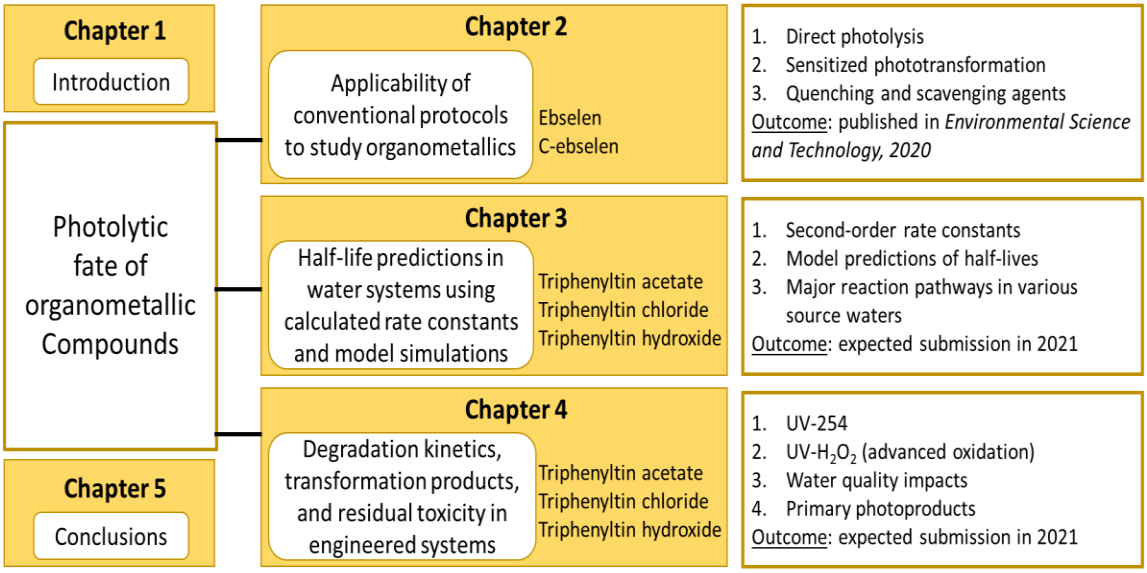

Figure 1.1. Schematic showing the organization of this dissertation.

Chapter 2 evaluates the suitability of commonly used reactive species sensitizers and probes to study the photochemical reaction kinetics of ebselen as a representative

organoselenium chemical. Ebselen is an efficient scavenger of reactive oxygen species (ROS), such as $^1O_2$, superoxide anion radical ($O_2^{\bullet}$), H_2O_2, and peroxynitrite ($OONO^-$). This property complicates the selection of appropriate sensitizers and probes for determination of the bimolecular rate constants for ebselen reaction with ROS. The chapter examined traditional $^1O_2$ (*e.g.*, Rose Bengal, perinapthanone) and $^{\bullet}OH$ (*e.g.*, H_2O_2, nitrate) sensitizers, as well as many ROS probes (*e.g.*, sorbic acid, isopropanol, tert-butanol). The carbon analog of ebselen (C-ebselen), 2-phenyl-3H-isoindol-1-one, was also investigated as a reference compound to establish the role of the selenium atom in ebselen phototransformation. Ebselen exhibited higher photoreactivity than C-ebselen due to interactions with excited triplet sensitizers and intermediate radicals that are kinetically irrelevant for other organic chemicals. These findings confirmed the unique impacts of the selenium atom on photochemical reactivity. The results of this chapter indicated that traditional ROS sensitizers and probes should be carefully evaluated for applications involving organometallic chemicals. This chapter was published in *Environmental Science & Technology* in 2020 [53].

Chapter 3 describes the fate of triphenyltin hydroxide in different water sources through a combination of laboratory experiments and model simulations in APEX. The photodegradation half-lives of triphenyltin hydroxide in surface water, wastewater effluent, stormwater, wetlands, and natural organic matter extracts were predicted using experimentally-determined kinetic parameters (*i.e.*, direct photolysis quantum yield, second-order rate constants for triphenyltin hydroxide reaction with $^1O_2$, $^{\bullet}OH$, and $^3DOM^*$) and literature-reported quantum yields of formation for $^1O_2$, $^{\bullet}OH$, and $^3DOM^*$.

The half-lives ranged from weeks to several months depending on water quality. The contributions of the direct photolysis, $^1O_2$, •OH, and $^3DOM^*$ reaction pathways to the overall triphenyltin hydroxide photodegradation kinetics were determined. Direct photolysis was found to be a negligible reaction mechanism, and $^1O_2$ was found to be the dominant contributor (60-80%) to triphenyltin hydroxide degradation in the environment. This chapter emphasized the role of DOM composition and source for triphenyltin hydroxide degradation in different water systems. Compared to surface water, fast degradation kinetics were observed in wetlands and waters affected by stormwater and wastewater effluent. The quantitative modeling results also emphasized the need for treatment systems to remove triphenyltin chemicals from point sources. This chapter will be submitted for publication in 2021.

Chapter 4 reports the transformation of triphenyltin hydroxide during UV-254 treatment and UV-H_2O_2 advanced oxidation. Experiments were conducted to measure the quantum yield of triphenyltin hydroxide and the second-order rate constants for triphenyltin hydroxide reaction with •OH. The results indicated that the removal efficiencies of triphenyltin hydroxide for typical treatment conditions employed in the UV-254 and UV-H_2O_2 processes were 2-10% and 50-92%, respectively. In addition, the effects of water quality parameters (*e.g.*, solution pH, ionic strength, and DOM) were evaluated to determine the phototransformation kinetics of triphenyltin hydroxide for different water quality conditions. The primary phototransformation products were identified for direct and advanced oxidation of triphenyltin hydroxide and, importantly, bacterial growth inhibition assays demonstrated that photoproducts were more potent than the parent

compound. Importantly, conventional UV-254 processes resulted in higher residual toxicity and more potent phototransformation products compared to UV-H_2O_2 treatment; therefore, advanced oxidation processes are preferred due to both faster kinetics and less toxic products. This chapter is expected to be submitted for publication in 2021.

Chapter 5 summarizes the main findings and conclusions of this dissertation and makes recommendations for future research to further advance understanding of the photochemical fate of organometallics in engineered and natural systems.

1.5 Significance

The primary significance of this dissertation stems from this work being the first comprehensive study of the environmental photolysis of organometallic chemicals. This research combined aspects of environmental chemistry, photochemistry, and photokinetic modeling to investigate the environmental fate of organometallic compounds in both natural and engineered systems. The research plan was designed to systematically determine the following parameters for representative organo-selenium and -tin chemicals: molar absorption coefficients; quantum yields for organometallics in natural (*i.e.*, 365 nm) and engineered (*i.e.*, 254 nm) systems; second-order rate constants for organometallic reactions with reactive species ($^1O_2$, $^{\bullet}OH$, and $^3DOM^*$); impacts of water quality parameters on organometallic photodegradation kinetics; dominant reaction pathways of organometallics in different water sources; and, the structures and toxicological relevance of organometallic phototransformation products. This systematic approach enabled a thorough understanding of the photochemical fate of highly reactive

organometallic compounds in water/wastewater treatment processes and environmental systems. In addition, the experimental results reported in this dissertation will (i) assist with the selection of appropriate photochemical/photocatalytic treatment processes for emerging organometallic chemicals and (ii) inform organometallic product stability for pharmaceutical and pesticide manufacturers. Overall, this dissertation will be a valuable resource on the photochemistry of organometallics in natural systems and engineered treatment processes.

Chapter 2 Photochemistry of the organoselenium compound ebselen: direct photolysis and reaction with active intermediates of conventional reactive species sensitizers and quenchers

Abstract

Ebselen (EBS), 2-phenyl-1,2-benzisoselenazol-3(2H)-one, is an organoselenium pharmaceutical with antioxidant and anti-inflammatory properties. Furthermore, EBS is an excellent scavenger of reactive oxygen species. This property complicates conventional protocols for sensitizing and quenching reactive species due to potential generation of active intermediates that quickly react with EBS. In this study, the photochemical reactivity of EBS was investigated in the presence of (1) $^1O_2$ and $^{\bullet}OH$ sensitizers (Rose Bengal (RB), perinaphthanone, H_2O_2) and (2) reactive species scavenging and quenching agents (sorbic acid, isopropanol, sodium azide, *tert*-butanol) that are commonly employed to study photodegradation mechanisms and kinetics. The carbon analog of EBS, namely 2-phenyl-3H-isoindol-1-one, was included as a reference compound to confirm the impact of the selenium atom on EBS photochemical reactivity. EBS does not undergo acid dissociation, but pH-dependent kinetics were observed in RB-sensitized solutions, suggesting EBS reaction with active intermediates ($^3RB^{2-*}$, $O_2^{\bullet-}$, H_2O_2) that are not kinetically-relevant for other compounds. In addition, the observed rate constant of EBS increased in the presence of sorbic acid, isopropanol, and sodium azide. These findings suggest that conventional reactive species sensitizers, scavengers, and quenchers need to be carefully applied to highly reactive organoselenium compounds to account for reactions that are typically slow for other organic contaminants.

2.1 Introduction

Ebselen (EBS) is an organoselenium compound with anti-inflammatory, anti-atherosclerotic, and cytoprotective properties [13,22]. Currently, EBS is mostly used as an antioxidant and glutathione peroxidase mimic [24,25]. Ongoing clinical trials are investigating EBS as a treatment for reperfusion injury, stroke, hearing loss, and bipolar disorder [54]. EBS has also emerged as a promising treatment for clinical isolates of multidrug-resistant *Staphylococcus aureus* [26,27]. Most recently, Jin *et al.* reported that out of more than 10,000 compounds investigated by structure-based and high-throughput screening, EBS emerged as the only compound with promising antiviral activity against COVID-19 in cell-based assays [55]. A recent PubMed database search found more than 1000 publications on EBS, with many focused on potential therapeutic applications or synthesis of EBS analogs or derivatives. For these reasons, organoselenium compounds represent a new class of contaminants of emerging concern.

The aforementioned pharmaceutical applications stem from the biochemical properties of EBS, including its excellent scavenging of reactive oxygen species, such as singlet oxygen ($^1O_2$), hydrogen peroxide (H_2O_2), and peroxynitrite ($OONO^-$) [13,56,57]. However, EBS can also cause cellular toxicity. For example, EBS induced necrotic cell death, DNA damage, genotoxicity, and apoptosis at high concentrations [14,58,59]. Several studies have also reported acute and chronic effects of selenium on fish and wildlife at concentrations of 1-5 µg L^{-1} [60,61]. Based on recent scientific findings, EPA set a new national chronic aquatic life criterion for selenium in 2016 [62]. Although metabolic studies suggest that

selenium is not immediately released from EBS, the fate of EBS in abiotic environmental systems and water/wastewater treatment processes is unknown. Due to its antioxidant properties, EBS is expected to exhibit fast photodegradation kinetics in natural water bodies, where reactive oxygen species are generated through indirect photolysis. However, the photochemical reactivity and degradation mechanisms of EBS are unknown and warrant investigation.

Previous studies have identified the kinetic relevance of both direct and indirect photolysis mechanisms to photodegradation of organic contaminants in engineered and natural systems [9,63]. The rate constants for photodegradation mechanisms are typically determined in well-controlled laboratory experiments and then applied to calculate the half-lives of contaminants in the natural environment [64-66]. The corresponding experimental protocols employ reactive species sensitizers, such as Rose Bengal (RB; for $^1O_2$), perinaphthanone (PN; for $^1O_2$ and surrogate for triplet dissolved organic matter ($^3DOM^*$)), and Suwannee River Natural Organic Matter (for $^1O_2$, hydroxyl radicals ($^\bullet OH$), and $^3DOM^*$). In addition, reactive species scavengers and quenchers, such as sorbic acid (for triplets, also prevents $^1O_2$ production), sodium azide (NaN_3; for $^1O_2$ and $^\bullet OH$), isopropanol (for $^\bullet OH$), and *tert*-butanol (for $^\bullet OH$), are used to inhibit certain reaction mechanisms and isolate others. Together, these tools facilitate determination of specific rate constants for organic contaminants with individual reactive species.

We hypothesize that the antioxidant properties of EBS [13,56,57] will pose challenges to the use of conventional protocols for sensitizing and quenching reactive species due to

generation of active intermediates that quickly react with EBS. For example, RB forms the following transient species: triplet RB ($^3RB^{2-*}$); $RB^{\bullet 3-}$; $RB^{\bullet -}$; $^1O_2$; and, superoxide anion radical ($O_2^{\bullet -}$) [67,68]. As indicated in Figure 2.2, $^3RB^{2-*}$, $RB^{\bullet 3-}$, and $RB^{\bullet -}$ are not kinetically relevant for many organic chemicals; therefore, many studies do not consider these reactions [69,70]. If reactions between RB active intermediates and the organic chemical are kinetically relevant but not considered, the calculated second-order rate constant for $^1O_2$ reaction with that chemical would be over-estimated by RB-sensitized experiments. Criado *et al.* [67] observed fast reactions between tryptophan and $^3RB^{2-*}$ with rate constants on the order of 10^7 M^{-1} s^{-1}. In solution, $^3RB^{2-*}$ is quenched by molecular oxygen in a reaction that yields 75% $^1O_2$ and 20% $O_2^{\bullet -}$ [69]. While most studies focus on the $^1O_2$ product, select tryptophan derivatives can also react with $O_2^{\bullet -}$ at kinetically-relevant rates [67]. Similarly, Davis *et al.* [71] reported the high reactivity of fenamates with triplet PN, which stems from the use of PN as a $^1O_2$ and triplet sensitizer.

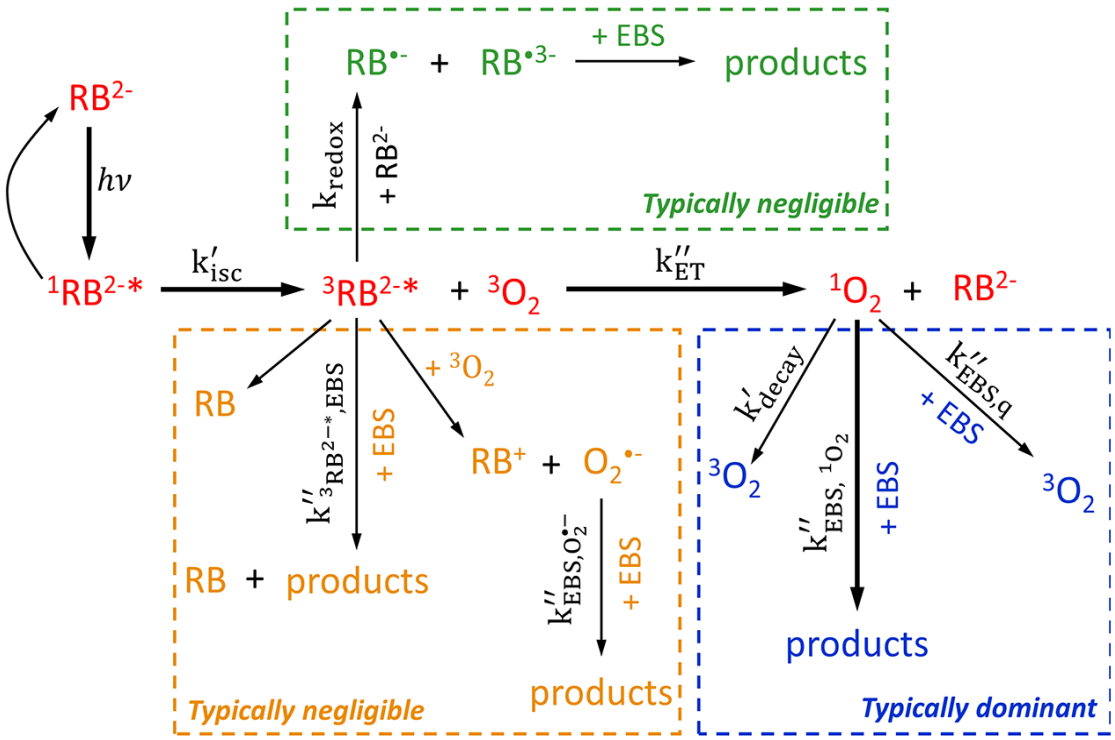

Figure 2.2. Photochemistry of RB and proposed reactions with EBS. The rate constants indicated in the figure are defined as follows: $\mathbf{k'_{isc}}$, rate constant for inter-system crossing of $^1RB^{2-*}$ to $^3RB^{2-*}$; $\mathbf{k''_{ET}}$, rate constant for energy transfer reaction from $^3RB^{2-*}$ to molecular oxygen, $^3O_2$; $\mathbf{k''_{^3RB^{2-*},EBS}}$, rate constant for energy transfer reaction from $^3RB^{2-*}$ to EBS; $\mathbf{k''_{EBS,O_2^{\bullet-}}}$, second-order rate constant for EBS reduction by $\mathbf{O_2^{\bullet-}}$; $\mathbf{k'_{decay}}$, rate constant for $^1O_2$ decay to $^3O_2$; $\mathbf{k''_{EBS,\,^1O_2}}$, second-order rate constant for EBS reaction with $^1O_2$ (chemical quenching); $\mathbf{k''_{EBS,q}}$, second-order rate constant for physical quenching of $^1O_2$ by EBS; and, $\mathbf{k_{redox}}$, rate constant for reduction of $^3RB^{2-*}$ by RB^{2-}. The thick, black reaction arrows emphasize the reactions typically considered in RB-sensitized experiments. The RB photochemistry was adapted from previous literature [67,68] to elucidate potential reaction pathways for EBS.

Other chemicals used to sensitize, scavenge, or quench reactive species also produce triplets and/or active intermediate radicals (see Table S1 in the Supporting Information (SI)) [54,72,73]. As noted above, EBS is an excellent scavenger of reactive species; therefore, secondary reactions must be carefully examined to ensure proper calculation of second-order rate constants for specific reactions. For example, secondary organic radicals (*e.g.*, R$^\bullet$ and ROO$^\bullet$), which are often kinetically negligible, are formed by the reaction of *tert*-butanol with $^\bullet$OH [54]. If EBS reacts with the R$^\bullet$ or ROO$^\bullet$ active intermediates, the use of

tert-butanol to quench $^{\bullet}OH$ can lead to other unaccounted mechanisms. Packer *et al.* [74] reported similar observations when using isopropanol to quench radicals during photodegradation of clofibric acid and diclofenac. Addition of 1% isopropanol (v/v) increased the photodegradation rates for clofibric acid and diclofenac by 1.7× and 1.45×, respectively, compared to those observed in deionized (DI) water. One reason for the enhanced phototransformation kinetics was formation of active isopropanol intermediates. Unless carefully examined, these reactions can lead to calculation of inaccurate rate constants.

The heightened interest in organoselenium pharmaceuticals coupled to the general lack of knowledge regarding the photochemistry of these molecules motivated the present study. We hypothesized that the selenium atom in EBS would participate in complex photochemical reactions that are difficult to capture using conventional sensitization and quenching protocols. The overall goal of this study was to investigate the photochemical reactivity of EBS with (1) $^{1}O_2$ and $^{\bullet}OH$ sensitizers (*i.e.*, RB, PN, and H_2O_2) and (2) reactive species scavenging and quenching agents (*i.e.*, isopropanol, sorbic acid, and *tert*-butanol) that are commonly employed to study the fate of organic contaminants during direct and indirect photolysis. To determine the role of the selenium atom in direct and indirect photochemical reactions, we examined the fate of the EBS carbon analog (*i.e.*, 2-phenyl-3H-isoindol-1-one (C-EBS), namely EBS but with a carbon atom substituted for the selenium atom). To establish the baseline photoreactivity, wavelength-dependent, pseudo-first-order rate constants and quantum yields were evaluated for direct photolysis

of EBS and C-EBS. Although this work specifically focused on EBS, the outcomes contribute to overall understanding of organoselenium photochemistry.

2.2 Experimental Materials and Methods

2.2.1 Chemicals

Details on the chemical reagents used in experiments are included in Text A1 of Appendix 1.

2.2.2 Analytical methods

The analytical methods employed for quantitation of EBS, C-EBS, *para*-chlorobenzoic acid (*p*CBA; $^{\bullet}$OH probe), and furfuryl alcohol (FFA; $^1O_2$ probe) are described in Text A2 of Appendix A.

2.2.3 Photolysis Experiment

All photochemical experiments were performed in an eight-position, merry-go-round Rayonet reactor (Southern New England Ultraviolet Inc.; Branford, CT) equipped with eight bulbs emitting (i) monochromatic light at 254 nm or (ii) across the 310-410 nm range with a peak at 365 nm (labeled 365 nm, below). The 254-nm and 365-nm bulbs were used to sensitize the production of $^{\bullet}$OH and $^1O_2$, respectively. Moreover, the 254-nm and 365-nm light sources were representative of UV disinfection processes in drinking water and wastewater treatment plants and the high-energy solar irradiation that reaches surface water, respectively, providing insight to direct photolysis of EBS in these systems. The average incident photon flux for the 254-nm and 365-nm systems were

calculated to be 2.71 (± 0.18) × 10^{-5} Ein L^{-1} s^{-1} and 1.93 (± 0.40) × 10^{-5} Ein L^{-1} s^{-1}, respectively, using the ferrioxalate actinometer [8,75]; note, error values refer to the standard deviation of three measurements. To determine the direct photolysis kinetics, experimental solutions contained 3.6 µM EBS or C-EBS and 5 mM phosphate buffer in DI water. Experimental solutions were irradiated in quartz tubes with an inner diameter of 1.5 cm. Samples were collected at predetermined times and stored at -20 °C in amber vials prior to analysis by liquid chromatography with triple quadrupole tandem mass spectrometry (LC-MS/MS) or high-performance liquid chromatography with UV absorbance detection. Dark controls were included to account for other reactions, including hydrolysis and direct reaction of EBS with reactive species quenchers, scavengers, and sensitizers. All experiments were conducted at room temperature (*i.e.*, 22 ± 1°C).

2.2.3.1. *Reactivity of EBS with $^1O_2$ sensitizers*

The photoreactivity of EBS in solutions containing the RB and PN $^1O_2$ sensitizers was investigated at 365 nm. Experimental solutions contained 3.6 µM EBS, 5 µM RB or 0.5 µM PN, 0.2 mM FFA, and 5 mM phosphate buffer in DI water. Test conditions included five pH values between 4.4 and 10.2. The experiments were conducted at similar conditions with C-EBS to determine the importance of the selenium atom on EBS reactivity with $^1O_2$; however, the RB concentration was increased to 40 µM for the C-EBS experiments due to the slower reaction between C-EBS and $^1O_2$ observed in preliminary investigations. The steady-state $^1O_2$ concentration (*i.e.*, $[^1O_2]_{ss}$) was calculated by dividing the observed pseudo-first-order rate constant for FFA degradation

by its second-order rate constant with $^1O_2$ (*i.e.*, $k''_{^1O_2,FFA} = 1.0 \times 10^8\ M^{-1}\ s^{-1}$ [76]). In separate experiments, 5 and 10 mM NaN_3 were added to the experimental solutions to quench $^1O_2$ (as it was produced) and investigate EBS degradation by triplets or active intermediates of the RB and PN sensitizers.

2.2.3.2. *Reactivity of EBS with ˙OH sensitizers*

Conventional methods of generating ˙OH, such as UV-H_2O_2, photo-Fenton reactions, and solar irradiation of NO_3^- or NO_2^- [77], may complicate evaluation of EBS degradation kinetics due to secondary reactions with H_2O_2, $ONOO^-$, or other active intermediates [57,78,79]. For this reason, sodium pyruvate was employed as a non-radical-forming H_2O_2 quenching agent. The suitability of pyruvate was investigated in the dark using the following solutions: (i) 0.36-36 µM EBS; (ii) 0.36-36 µM EBS + 7.5 mM sodium pyruvate; (iii) 0.36-36 µM EBS + 0.5 mM H_2O_2; and, (iv) 0.36-36 µM EBS + 0.5 mM H_2O_2 + 7.5 mM sodium pyruvate. These solutions were always generated by first adding EBS, then sodium pyruvate (when applicable), and then H_2O_2 (when applicable). To confirm the extent of H_2O_2 quenching by pyruvate, EBS concentrations in these samples were analyzed immediately after preparation and again after 24 h of storage in the dark.

The second-order rate constant for EBS reaction with H_2O_2 was determined in the dark. The 10-mL experimental solutions contained 3.6 µM EBS, 50 µM H_2O_2, and 5 mM phosphate buffer (pH 7.0 ± 0.1). An excess of H_2O_2 was added to allow calculation of the pseudo-first-order rate constant [64]; in particular, the initial concentration ratio of H_2O_2 to EBS was 15 mol/mol to ensure that residual EBS concentrations were above the

analytical limits of quantitation. Samples (100 µL) were collected at designated times and deposited into vials containing 900 µL of 7.5 mM sodium pyruvate to immediately quench the H_2O_2 residual. The second-order rate constant for EBS reaction with H_2O_2 (k''_{EBS,H_2O_2}) was calculated by dividing the observed pseudo-first-order rate constant of EBS ($k'_{EBS,obs}$) by the molar H_2O_2 concentration ($[H_2O_2]$), as indicated in Eq. 2.1.

$$k''_{EBS,H_2O_2} = \frac{k'_{EBS,obs}}{[H_2O_2]} \quad \text{(Eq. 2.1)}$$

The second-order rate constant for EBS reaction with •OH ($k''_{EBS,\ \cdot OH}$) was measured by competition kinetics with *p*CBA. Experimental solutions containing 3.6 µM EBS, 5 µM H_2O_2, 75 µM *p*CBA, and 5 mM phosphate buffer (pH 7.0 ± 0.1) were irradiated at 254 nm. Samples (100 µL) collected at designated times were mixed with 900 µL of 7.5 mM sodium pyruvate to quench the H_2O_2 residual and inhibit further reactions. EBS could have degraded by direct photolysis, reaction with H_2O_2, or reaction with •OH. The *p*CBA probe molecule can undergo similar reactions, but the H_2O_2 reaction is not kinetically relevant [80]. The integrated mass balance expressions for EBS and *p*CBA in the batch reactors are shown in Eq. 2.2 and Eq. 2.3, respectively.

$$-\ln\frac{[EBS]_t}{[EBS]_0} = k'_{d,EBS}t + k''_{EBS,H_2O_2}[H_2O_2]t + k''_{EBS,\ \cdot OH}\int_0^t [\ ^{\bullet}OH]\,dt \quad \text{(Eq. 2.2)}$$

$$-\ln\frac{[p\mathrm{CBA}]_t}{[p\mathrm{CBA}]_0} = k'_{d,p\mathrm{CBA}}t + k''_{p\mathrm{CBA},\,{}^{\bullet}\mathrm{OH}}\int_0^t [\,{}^{\bullet}\mathrm{OH}]\,dt$$

(Eq. 2.3)

The variables in Eq. 2.2 and 2.3 are defined as follows: t is the irradiation time (s); $[\mathrm{EBS}]_0$ and $[\mathrm{EBS}]_t$ are the EBS concentrations (μM) at time 0 and t, respectively; $[p\mathrm{CBA}]_0$ and $[p\mathrm{CBA}]_t$ are the *p*CBA concentrations (μM) at time 0 and t, respectively; $k'_{d,\mathrm{EBS}}$ and $k'_{d,p\mathrm{CBA}}$ are apparent time-based pseudo-first-order rate constants for direct photolysis of EBS and *p*CBA at 254 nm, respectively; and, $k''_{p\mathrm{CBA},\,{}^{\bullet}\mathrm{OH}}$ is the second-order rate constant for *p*CBA reaction with ·OH (*i.e.*, 5.2×10^9 $M^{-1}s^{-1}$ [81]).

As EBS and *p*CBA were present in the same reactor, the hydroxyl radical exposure (*i.e.*, $\int_0^t [\,{}^{\bullet}\mathrm{OH}]\,dt$) in Eq. 2.2 is equal to that in Eq. 2.3. These expressions can, therefore, be rearranged as shown in Eq. 2.4, which was used to solve for $k''_{\mathrm{EBS},\,{}^{\bullet}\mathrm{OH}}$ [9].

$$\left[\ln\left(\frac{[\mathrm{EBS}]}{[\mathrm{EBS}]_0}\right) + k'_{d,\mathrm{EBS}}t + k''_{\mathrm{EBS},H_2O_2}[H_2O_2]t\right] = \left[\ln\left(\frac{[p\mathrm{CBA}]}{[p\mathrm{CBA}]_0}\right) + k'_{d,p\mathrm{CBA}}t\right]\frac{k''_{\mathrm{EBS},\,{}^{\bullet}\mathrm{OH}}}{k''_{p\mathrm{CBA},\,{}^{\bullet}\mathrm{OH}}}$$

(Eq. 2.4)

A similar experimental design was employed to calculate second-order rate constants for C-EBS with ·OH; however, the H_2O_2 concentration was increased to 5 mM due to the lower observed reactivity of C-EBS with ·OH (compared to EBS).

2.2.3.3 *Reactivity of EBS with scavengers and quenchers*

The reactivity of EBS with reactive species scavenging and quenching molecules, and associated triplets or active intermediates, was investigated by irradiating 3.6 μM EBS in the presence of 0.5 mM sorbic acid (triplet quencher, also prevents $^1O_2$ production) or 50-100 mM isopropanol ($^{\bullet}OH$ quencher) at 365 nm. All solutions were buffered at pH 7.0 ± 0.1 with 5 mM phosphate buffer. Furthermore, the reactivity of EBS in the presence of 0, 1, and 10 mM NaN_3 ($^1O_2$ and $^{\bullet}OH$ quencher) was investigated at 254 nm and 365 nm, with solution pH adjusted to 4, 6, 8, and 10 by 5 mM phosphate buffer.

Secondary organic radicals (*e.g.*, R• and ROO•) formed through *tert*-butanol reaction with $^{\bullet}OH$ [54] might react with EBS. To examine whether these reactions were kinetically relevant, experimental solutions containing 3.6 μM EBS, 5 μM H_2O_2, 10-100 mM *tert*-butanol, and 5 mM phosphate buffer (pH 7.0 ± 0.2) were irradiated at 254 nm. Samples (100 μL) from the above experiments were collected at designated times and deposited into vials containing 900 μL of 7.5 mM sodium pyruvate to quench further reactions.

2.3 Results and Discussion

2.3.1 Direct photolysis of EBS and C-EBS

The apparent molar absorption coefficient and quantum yield dictate the extent of chemical degradation by direct photolysis. The molar absorption coefficients of EBS and C-EBS are shown for 230-380 nm and pH 4.5, 7.0, and 9.5 in Figure A6 of the SI. Due to their aromatic moieties, EBS and C-EBS both absorb UVC light, and the apparent molar

absorption coefficients at 254 nm were 1.22 (± 0.01) × 10^4 M^{-1} cm^{-1} and 6.91 (± 0.11) × 10^3 M^{-1} cm^{-1}, respectively; note, the error corresponds to standard deviation (n = 3). Compared to C-EBS, EBS exhibited extended absorbance into the UVA region (up to 370 nm), presumably due to the presence of the selenium atom, which was the only difference between the two chemicals. Neither compound undergoes acid dissociation, and both compounds are present in solution as neutral molecules. For these reasons, solution pH had a negligible influence on the absorbance spectra (see Figure A6 in Appendix A).

The degradation kinetics of EBS and C-EBS were investigated at pH 7 for direct photolysis at 254 nm and 365 nm. The observed pseudo-first-order rate constants at 254 nm for EBS and C-EBS were 2.74 (± 0.20) × 10^{-3} s^{-1} and 8.50 (± 0.32) × 10^{-4} s^{-1}, respectively. Phototransformation reactions were slower for irradiation with light at 365 nm, wherein the observed rate constant for EBS transformation was 5.17 (± 0.95) × 10^{-5} s^{-1} and C-EBS showed negligible degradation kinetics ($k'_{\mathrm{d,C-EBS}}$ < 2.3 × 10^{-6} s^{-1}). The error values reported above correspond to 95% confidence intervals on the mean rate constant calculated from time-series experiments (n = 14). Using these rate constants, the apparent quantum yield was calculated (see Text S3 and Eq. S1 in the SI). The apparent quantum yields at 254 nm for EBS and C-EBS were 13.6 (± 0.1) × 10^{-2} mol Ein^{-1} and 2.0 (± 0.7) × 10^{-2} mol Ein^{-1}, respectively. For 365 nm, EBS exhibited an apparent quantum yield of 1.4 (± 0.1) × 10^{-3} mol Ein^{-1}; however, the quantum yield of C-EBS at 365 nm was much lower ($\phi_{\mathrm{C-EBS},365}$ < 2.8 × 10^{-5} mol Ein^{-1}). Due to the low extent of degradation, the

reported quantum yield for C-EBS at 365 nm was an upper-bound estimate included to contextualize the differences between EBS and C-EBS reactivity.

The observed pseudo-first-order rate constants for EBS photodegradation are summarized in Table 2-1. At 254 nm, EBS exhibited pH-dependent photodegradation with the observed rate constant increasing from 1.73 (± 0.27) × 10^{-3} s^{-1} at pH 4.4 to 13.50 (± 0.43) × 10^{-3} s^{-1} at pH 10.5. Solution pH exerted a similar effect on EBS photodegradation at 365 nm, but the magnitude of the change in observed rate constant was much lower. The pseudo-first-order rate constants at 254 nm and 365 nm increased by 680% and 73%, respectively, across the pH 4.4-10.5 range. The faster EBS photoreaction kinetics observed at higher pH were not expected because (i) EBS does not dissociate and (ii) the measured molar absorption coefficients were similar for the pH 4.5-9.5 range. A potentiometric titration was conducted and confirmed the absence of environmentally-relevant acid dissociation sites; furthermore, the ChemAxon structure-based algorithm [82] did not identify an acid dissociation site in the pH 0-14 range. Previous studies indicated that phosphate buffer can promote photoreduction and/or photoaddition mechanisms [83,84]; however, Figure A7 in Appendix A highlights insignificant impacts on EBS degradation for solutions containing 0, 10, 20, and 30 mM phosphate buffer at pH 7.2.

Table 2-1. Observed pseudo-first-order rate constants for direct photolysis of EBS with light at 254 nm and 365 nm.

Solution pH	Observed rate constant (s^{-1})	
	254 nm	**365 nm**
4.4	1.73 (± 0.27) × 10^{-3}	3.45 (± 0.36) × 10^{-5}
5.1	1.80 (± 0.58) × 10^{-3}	3.14 (± 0.48) × 10^{-5}
6.3	2.59 (± 0.21) × 10^{-3}	4.77 (± 0.66) × 10^{-5}
6.9	2.74 (± 0.20) × 10^{-3}	5.17 (± 0.95) × 10^{-5}
7.8	4.18 (± 0.10) × 10^{-3}	5.41 (± 0.87) × 10^{-5}
8.3	7.22 (± 0.22) × 10^{-3}	5.60 (± 0.48) × 10^{-5}
9.4	8.88 (± 0.24) × 10^{-3}	5.34 (± 0.64) × 10^{-5}
10.5	13.50 (± 0.43) × 10^{-3}	5.98 (± 0.81) × 10^{-5}

The observed differences in direct photolysis kinetics may also stem from pH-dependent self-sensitized reactions. Photosensitized generation of reactive oxygen species by EBS may involve both type I (electron transfer reactions to produce $O_2^{\bullet -}$) and type II (energy transfer to molecular oxygen to produce $^1O_2$) reactions [69,85], as shown in Eq. 2.5-2.8.

$$EBS + h\nu \rightarrow {}^1EBS^* \rightarrow {}^3EBS^* \quad \text{(Eq. 2.5)}$$

$${}^3EBS^* + O_2 \rightarrow {}^1O_2 + EBS \quad \text{(Eq. 2.6)}$$

$$EBS + h\nu \rightarrow EBS^{\bullet +} + e_{aq}^- \quad \text{(Eq. 2.7)}$$

$$e_{aq}^- + O_2 \rightarrow O_2^{\bullet -}$$

(Eq. 2.8)

In Eq. 2.5-2.8, $^1EBS^*$ is excited singlet state EBS, $^3EBS^*$ is excited triplet state EBS, $EBS^{\bullet +}$ is EBS radical cation, and e_{aq}^- is a solvated electron.

To investigate the aforementioned mechanisms, transient absorption spectroscopy was conducted at 355 nm. Details of the instrument and data analysis are available in previous reports [86,87] and Text S4 of the SI. Figure A8 in Appendix A demonstrates the absence of spectroscopic evidence for $^3EBS^*$ and $EBS^{\bullet +}$ production at pH 4.4-11.2. These results suggest (i) low quantum yields of EBS transients at the 355 nm excitation wavelength and/or (ii) low molar absorption coefficients of transient species. The transient absorption spectroscopy results support the lower pH-dependence of EBS rate constants at 365 nm reported in Table 2-1. However, the higher photoreactivity of EBS at 254 nm, which stemmed from a 31× higher molar absorption coefficient and a 96× higher quantum yield (compared to 365 nm), suggested that self-sensitized reactions may be more evident for irradiation at 254 nm. While a detailed evaluation of the reaction mechanisms involved with direct photolysis was outside of the scope of this study, the importance of evaluating self-sensitized reactions and the influence of solution pH was identified for organoselenium chemicals.

2.3.2. EBS interactions with reactive species sensitizers

2.3.2.1. *Active intermediates of $^1O_2$ sensitizers react with EBS*

To sensitize the generation of $^1O_2$, solutions containing EBS were spiked with RB or PN and irradiated at 365 nm. The observed pseudo-first-order rate constants for EBS degradation in the RB-sensitized solutions are shown in Figure 2.3a. The observed rate constant increased from 7.03 (± 1.20) × 10^{-4} s^{-1} at pH 4.4 to 6.74 (± 1.80) × 10^{-3} s^{-1} at pH 10.2, corresponding to a 859% increase; however, the steady-state $^1O_2$ concentrations were comparable, 3.1 (± 0.5) × 10^{-12} M, for all pH conditions. The drastic change in observed rate constant coupled to the consistent $^1O_2$ concentration suggests the importance of other reaction mechanisms. While the rate constants for direct photolysis at 365 nm also increased at higher solution pH, the magnitude (*i.e.*, 3-6 × 10^{-5} s^{-1}) was about 100× lower than the observed rate constants for RB-sensitized experiments. Given the absence of acid dissociation reactions and the relatively minor contribution of direct photolysis at 365 nm, the faster photodegradation kinetics observed at higher pH in Figure 2.3a were attributed to EBS reaction with triplets or active intermediates of RB (see Figure 2.2). Similar results were observed in solutions containing PN (Figure A9 in Appendix A). Unlike EBS, C-EBS exhibited low reactivity in RB-sensitized solutions, and the measured degradation was negligible under all pH conditions (Figure A10 in Appendix A). These results suggest that the selenium atom played a crucial role in the faster reaction kinetics observed at higher pH.

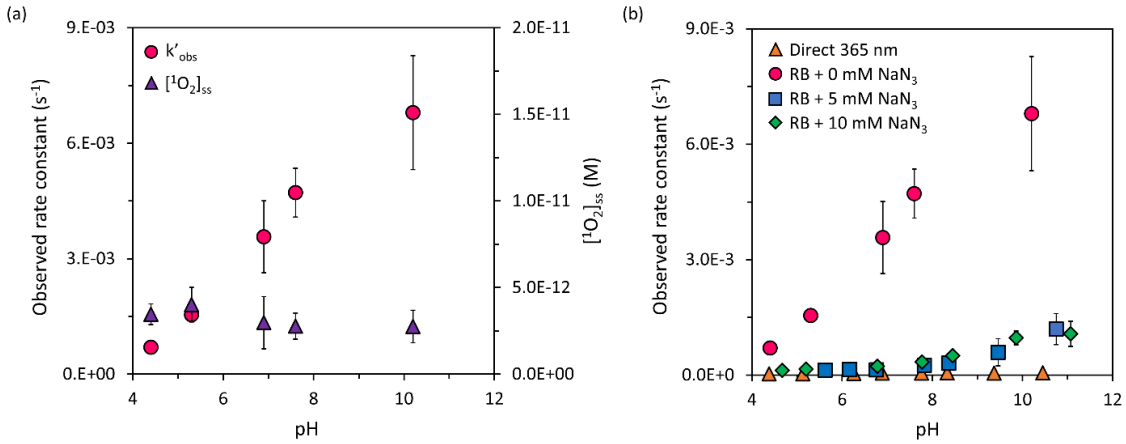

Figure 2.3. Observed pseudo-first-order rate constants for EBS photodegradation at 365 nm in (a) solutions that initially contained 3.6 µM EBS, 5 µM RB, and 0.2 mM FFA and (b) 5 µM RB-sensitized solutions with 3.6 µM EBS and 0, 5, and 10 mM NaN_3 (no FFA). Solution pH was maintained with 5 mM phosphate buffer. The secondary y-axis in (a) shows steady-state $^1O_2$ concentrations. The symbols correspond to rate constants calculated from time series experiments (n = 7). Error bars represent 95% confidence intervals on the mean rate constant from the time series experiments.

To confirm whether $^3RB^{2-}$* or active intermediates contributed to EBS photodegradation, 5 and 10 mM NaN_3 were added to experimental solutions to quench $^1O_2$ produced by the RB system. Even though NaN_3 quenches both $^1O_2$ and •OH, the quenching reaction is associated with $^1O_2$ as the expected •OH yield is low due to (1) the multistep reactions involved in •OH generation (electron transfer from $^3RB^{2-}$* to $^3O_2$ to form $O_2^{\bullet-}$ → self-dismutation of $O_2^{\bullet-}$ → H_2O_2 irradiation (254 nm)→ •OH), (2) the low initial concentration of RB (5 µM), and (3) the wavelength employed in these experiments (365 nm). Based on the EBS and NaN_3 concentrations, the rate constant for $^1O_2$ quenching by NaN_3 (1.5×10^9 M^{-1} s^{-1} [88,89]), and the rate constant for $^1O_2$ reaction with EBS (4.16×10^6 M^{-1} s^{-1} [56]), NaN_3 quenched more than 99.99% of $^1O_2$. Direct EBS reaction with NaN_3 was kinetically negligible. Figure 2.3b indicates that the addition of NaN_3 suppressed EBS photodegradation kinetics at all pH conditions, although the observed rate constants for EBS degradation still increased from pH 7 to pH 11. No significant differences were

identified between the observed rate constants for the 5 and 10 mM NaN_3 conditions at any pH ($p > 0.10$, ANCOVA), suggesting that these concentrations were sufficient to quench $^1O_2$ formed by the RB sensitizer. With 10 mM NaN_3, the observed rate constant for EBS photodegradation was suppressed (compared to the 0 mM NaN_3 condition) by 82% at pH 4.4, 90% at pH 7.0, and 86% at pH 10.2; however, the observed rate constant for EBS degradation was enhanced (compared to direct photolysis) by 72% at pH 4.4, 85% at pH 7.0, and 94% at pH 10.2. These results support the kinetic relevance of other active intermediates produced by irradiation of RB (see Figure 2.2) and/or NaN_3 (see section 2.3.3 for more details).

To further investigate the potential contributions of $^3RB^{2-*}$ to EBS degradation, transient absorption studies were conducted under anoxic conditions, at varying solution pH, and with incremental addition of EBS (see Text S4 of the SI). An excitation wavelength of 532 nm was employed to (1) selectively excite RB (note, EBS does not absorb light at 532 nm, see Figure A6 in Appendix A) and (2) avoid generation of other RB reactive intermediates (note, Allen *et al.* [90] reported generation of RB radicals at 313 nm but not above 514 nm). The experimental data confirmed that EBS reacts with $^3RB^{2-*}$. RB triplets can sensitize chemical degradation by energy transfer (E_T = 171-176 kJ mol^{-1}) [68,91] and/or electron transfer (reduction potential, $E°^*(^3RB^*/RB^{-\bullet}) = 1.23\ V_{SHE}$) [91]. Schöneich *et al.* [92] reported the oxidation potential of EBS to be 1.59 V, higher than the reduction potential of $^3RB^{2-*}$. Based on these findings, the electron transfer reaction mechanism of EBS with $^3RB^{2-*}$ is unlikely, and the energy transfer mechanism is proposed. The Stern-Volmer plot in Figure A11 of Appendix A was used to determine the second-order rate

constant of $^3RB^{2-*}$ with EBS (*i.e.*, 4.30 (± 0.15) × 10^8 $M^{-1}s^{-1}$). Importantly, solution pH did not influence the reaction kinetics (see Table S2 of the SI for second-order rate constants for EBS reaction with $^3RB^{2-*}$). Criado *et al.* [67] highlighted the important role of $^3RB^{2-*}$ in the photochemical degradation of tryptophan and its derivatives, which exhibited second-order reaction rate constants with $^3RB^{2-*}$ on the order of 10^7 $M^{-1}s^{-1}$. Another study reported second-order rate constants of 10^7- 10^8 $M^{-1}s^{-1}$ for neonicotinoids with $^3RB^{2-*}$ [93].

The pH-independent photoreaction kinetics of EBS with $^3RB^{2-*}$ (Figure A11 in Appendix A) and $^1O_2$ (postulated from the lack of acid dissociation and the consistent $^1O_2$ steady-state concentrations in Figure 2.3a) suggest another mechanism contributes to the observed rate constants for EBS degradation at high pH. While mechanistic evaluation of this reaction was beyond the scope of this study, one possible explanation for the pH-dependent photodegradation kinetics observed in Table 2-1 and Figure 2.3 may involve $O_2^{\bullet-}$. Previous pharmacological studies have indicated that EBS undergoes reduction by $O_2^{\bullet-}$ [94,95]. Lee *et al.* [69] reported that $^3RB^{2-*}$ quenching by molecular oxygen yields 75% $^1O_2$ and 20% $O_2^{\bullet-}$. While $O_2^{\bullet-}$ can undergo self-dismutation to form H_2O_2 [96], the rate of reaction exponentially decreased from pH 4.8 to pH 11 [97]. The effective concentration of $O_2^{\bullet-}$, therefore, increases at higher pH, potentially explaining the faster EBS photodegradation kinetics in RB-sensitized solutions at high pH. This hypothesis is supported by results from Chen *et al.* [98], who reported that a one-electron transfer mechanism for acetaminophen with $O_2^{\bullet-}$ was 1.1× faster at pH 10.0 than at pH 8.0. Given

the faster EBS photodegradation kinetics at higher pH, the contribution of H_2O_2 generated through $O_2^{\bullet-}$ self-dismutation to EBS degradation was negligible.

Overall, the reported data suggest that investigation of the environmental photochemistry of organoselenium chemicals requires careful consideration of the protocols used to identify transformation mechanisms and calculate rate constants. Due to the higher reactivity of EBS with $^3RB^{2-*}$ (4.30 (± 0.15) × 10^8 $M^{-1}s^{-1}$) than $^1O_2$ (4.16 × 10^6 M^{-1} s^{-1} [56]), the common strategy of using RB-sensitized solutions to directly calculate $^1O_2$ reaction kinetics would result in overestimation of the second-order rate constant for EBS with $^1O_2$ and underestimation of the EBS half-life in the natural environment. Findings from this study emphasize the importance of $^3RB^{2-*}$, $^1O_2$, $O_2^{\bullet-}$, H_2O_2, and solution pH to the reaction mechanisms and kinetics of EBS, and presumably other organoselenium chemicals, in RB- and PN-sensitized solutions.

2.3.2.2 *EBS reacts with ˙OH sensitizers*

Previous antioxidant studies have determined that EBS is an excellent scavenger of H_2O_2, $OONO^-$, and other nitrite radicals [57,78,79]. As a result, conventional methods to generate ˙OH, including UV-H_2O_2, photo-Fenton, and solar irradiation of NO_3^- or NO_2^-, may complicate the evaluation of EBS kinetics due to secondary reactions with H_2O_2 and $OONO^-$. These methods of sensitizing ˙OH cannot, therefore, be applied to determine the second-order rate constant for EBS reaction with ˙OH without a means to prevent EBS reaction with H_2O_2 or $OONO^-$. While ascorbic acid [99], dehydroascorbic acid [99], thiosulfate [100], horseradish peroxidase [101,102], and sodium pyruvate [103] have been used to

quench H_2O_2, some of these chemicals generate intermediate radicals that may react with EBS [99,100]. The reaction between sodium pyruvate and H_2O_2, however, yields non-radical products (see Eq. 2.9) and was, therefore, used to deconvolute the reaction kinetics of EBS with H_2O_2 and $^{\bullet}OH$.

$$CH_3COCOOH + H_2O_2 \rightarrow CH_3COOH + H_2O + CO_2 \quad \text{(Eq. 2.9)}$$

Dark experiments were conducted with EBS and H_2O_2 at pH 7.1. Upon collection, the samples were immediately mixed with 7.5 mM sodium pyruvate to quench the reaction; note, Figure A12 of Appendix A demonstrates that sodium pyruvate was an efficient quencher of residual H_2O_2. The pseudo-first-order reaction kinetics expression in Eq. 2.1 was applied to calculate k''_{EBS,H_2O_2}, which was determined to be 79.8 ± 0.8 M^{-1} s^{-1}. Using the calculated k''_{EBS,H_2O_2} and the second-order rate constant for sodium pyruvate quenching of H_2O_2 (*i.e.*, 0.75 M^{-1} s^{-1} [104]), the quenching reaction was verified to be 95% efficient. Two different k''_{EBS,H_2O_2} values have been reported in the literature: 1100 M^{-1} s^{-1} [105]; and, 4.83 M^{-1} s^{-1} [106]. The inconsistency in previously reported values might stem from interference by EBS transformation products during spectrophotometric analysis of EBS. In those studies, the normalized absorbance at 330 nm was linearly correlated to the normalized EBS concentration, and the second-order rate constant for EBS was calculated according to Eq. 2.1. Under the tested conditions, the reaction between EBS and H_2O_2 forms ebselen selenoxide [107], which interferes with spectrophotometric analyses (Figure A6 of Appendix A). This interference was not observed during the LC-

MS/MS analysis used in the present study (see Figure A13 of Appendix A), providing higher confidence in the reported second-order rate constant.

Competition kinetics experiments with *p*CBA were conducted to calculate the second-order rate constants for $^{\bullet}OH$ reaction with EBS and C-EBS. The observed degradation trends for direct photolysis at 254 nm, UV-H_2O_2 treatment, and (dark) reaction with H_2O_2 are shown in Figure 2.4 (EBS and C-EBS) and Figure A14 in Appendix A (*p*CBA). In Figure 2.4, the reaction between EBS and H_2O_2 is negligible in the dark due to pyruvate quenching of residual H_2O_2. The second-order rate constants for EBS and C-EBS with $^{\bullet}OH$ were calculated to be 4.33 (± 0.26) × 10^{10} M^{-1} s^{-1} and 1.76 (± 0.32) × 10^{8} M^{-1} s^{-1}, respectively, at pH 7.1. The high rate constant of EBS with $^{\bullet}OH$ reinforces the reactivity of EBS with reactive oxygen species. The selenium atom enhanced the chemical reactivity by two orders of magnitude. Although k''_{EBS,H_2O_2} (*i.e.*, 79.8 ± 0.8 M^{-1} s^{-1}) is orders of magnitude lower than the rate constants for EBS reaction with $^1O_2$, $^{\bullet}OH$, and other reactive species, the H_2O_2 concentration was much higher. Therefore, the reaction of EBS with H_2O_2 during sample preparation (prior to irradiation) and after sample collection (during storage) can lead to inaccurate rate constants if a suitable H_2O_2 scavenger is not used.

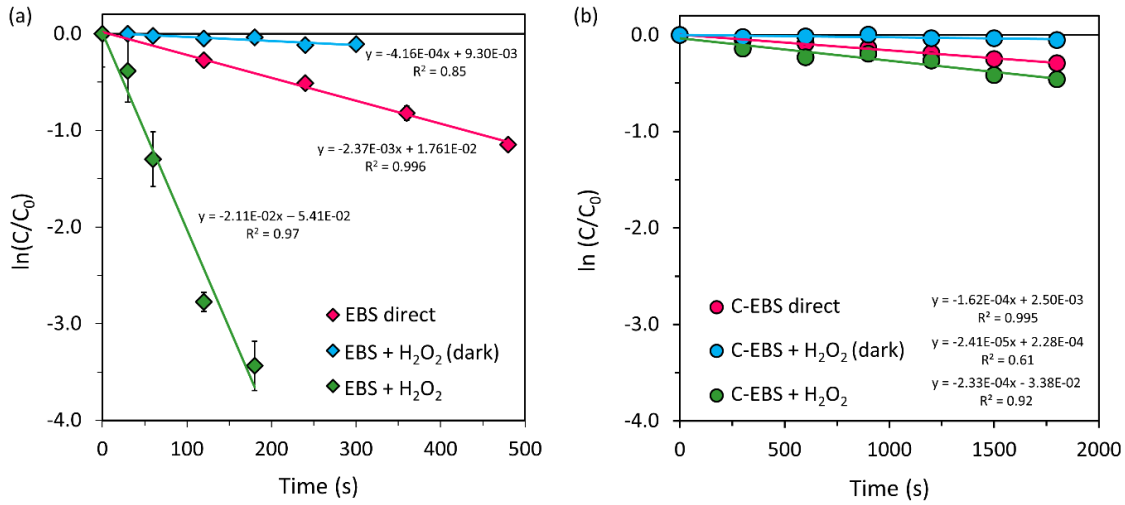

Figure 2.4. Degradation of 3.6 µM (a) EBS and (b) C-EBS at pH 7.1 for direct photolysis at 254 nm, UV-H_2O_2 treatment (254 nm), and reaction with H_2O_2 in the dark. The initial H_2O_2 concentrations were 5 µM for EBS and 5 mM for C-EBS to generate higher steady-state ˙OH concentrations. Due to its high reactivity with EBS, residual H_2O_2 was quenched by 7.5 mM sodium pyruvate for solutions in (a). The plotted symbols represent the mean of triplicate experiments, and the error bars are standard deviation.

2.3.3 Interaction of EBS with reactive species quenchers

The effects of select reactive species quenchers and scavengers on EBS photodegradation were evaluated. Since C-EBS is not a contaminant of interest, the confounding effects of reactive species quenchers and scavengers were not investigated. Figure 2.5a shows that when 0.5 mM sorbic acid was added to investigate the self-sensitized degradation of EBS at 365 nm and pH 6.8, the measured rate constant (*i.e.*, 2.36 (± 0.49) × 10^{-4} s^{-1}) was greater than the direct photolysis rate constant for EBS (*i.e.*, 4.86 (± 1.00) × 10^{-5} s^{-1}). With addition of sorbic acid, the observed rate constants for EBS degradation were expected to be similar (if no self-sensitization) or lower (if self-sensitization). The unexpected enhancement in EBS degradation kinetics can be explained by energy quenching from excited sorbic acid. Grebel *et al.* [108] indicated that sorbic acid can undergo direct photoisomerization at high concentrations due to a small overlap in the

sorbic acid absorbance spectrum (which extended beyond 310 nm) and the emission spectrum of lamps. Here, the lamp spectrum spanned 310-410 nm, and 0.5 mM sorbic acid was used. According to Grebel *et al.* [108], these conditions are expected to generate triplets in the experimental solutions. Moor *et al.* [73] reported the triplet excited energy of sorbic acid to be in the 187-217 kJ mol^{-1} range. As indicated in section 2.3.2.1, EBS undergoes an energy transfer mechanism with $^3RB^{2-}$*, which has a triplet excited energy of 171-176 kJ mol^{-1} [68,91]; therefore, a similar energy transfer reaction mechanism is expected to occur with sorbic acid triplets.

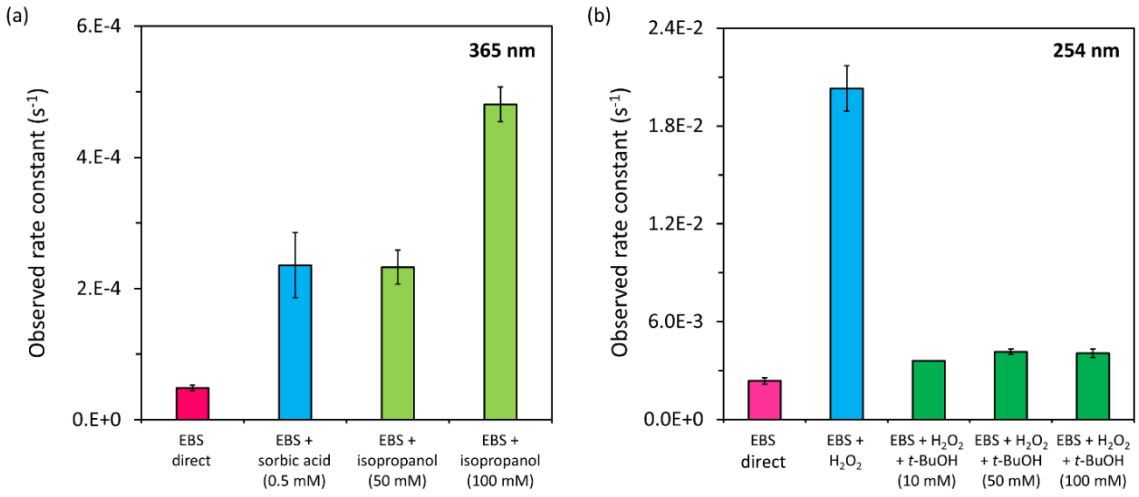

Figure 2.5. Comparison of observed rate constants for EBS degradation at (a) 365 nm with 0.5 mM sorbic acid and 50-100 mM isopropanol and (b) 254 nm with 5 µM H_2O_2 and 0, 10, 50, and 100 mM tert-butanol. The solution pH was 6.8. Error bars represent 95% confidence intervals on the mean rate constant from triplicate time series experiments (n = 7 × 3 = 21).

As suggested by Figure 2.5a, EBS reacted with isopropanol and active intermediates of isopropanol that was produced during irradiation. The rate constant for EBS degradation was dependent on the isopropanol concentration, with calculated values of 2.33 (± 0.26) × 10^{-4} s^{-1} and 4.81 (± 0.27) × 10^{-4} s^{-1} for 50 mM and 100 mM isopropanol, respectively.

The observed rate constants were one order of magnitude faster than direct photolysis of EBS at 365 nm (*i.e.*, 4.86 (± 1.00) × 10^{-5} s^{-1}). EBS also reacted with isopropanol in the dark, and the second-order rate constant was calculated to be 4.6 (± 1.2) × 10^{-4} $M^{-1}s^{-1}$. Packer *et al.* [74] reported similar observations with diclofenac and clofibric acid, namely isopropanol increased the photodegradation rate. Enhanced degradation of diclofenac and clofibric acid was attributed to active intermediates of isopropanol and photoreduction mechanisms [74]. If $EBS^{\bullet+}$ is formed upon irradiation, hydrogen atom transfer from isopropanol might lead to secondary reactions between hydroxyisopropyl radicals and EBS [109].

Figure A15 in Appendix A reports EBS degradation with 0, 1, and 10 mM NaN_3 at pH 4, 6, 8, and 10. These experiments were primarily designed to investigate the potential involvement of self-sensitized degradation of EBS at 254 nm and 365 nm with respect to the pH dependencies observed in section 2.3.1. At 365 nm, the addition of NaN_3 demonstrated no effect on EBS degradation. However, convoluted effects, similar to those reported for sorbic acid and isopropanol, were observed with NaN_3 at 254 nm. In particular, EBS exhibited enhanced degradation in the presence of NaN_3, and not the similar (if no self-sensitization) or lower (if self-sensitization) reaction rates that were expected. At pH 4, the addition of 1 mM and 10 mM NaN_3 increased photodegradation rates of EBS by 1.4× and 2.5×, respectively, compared to the 0 mM NaN_3 condition (see Figure A15 in the Appendix). At pH 10, the observed rate constants for EBS degradation in solutions containing 0, 1, and 10 mM NaN_3 were 2.9×, 6.0×, and 20.1× faster, respectively, than for pH 4 solutions with 0 mM NaN_3. Note that the apparent molar

absorption coefficient of NaN_3 at 254 nm was 84.6 M^{-1} cm^{-1}, and screening corrections were applied to the measured rate constants. Previous studies have reported azide radical (strong oxidant) formation through azide anion reaction with reactive oxygen species (*e.g.*, $^1O_2$, $O_2^{\bullet-}$, $^{\bullet}OH$) [89,110,111], potentially explaining the faster EBS rate constants observed at higher NaN_3 concentrations. Future investigations are necessary to further deconvolute the observed reaction kinetics of EBS with NaN_3, but these efforts were outside of the scope of this study. The reported findings suggest that NaN_3 should be avoided when studying EBS degradation kinetics; note, these results are also relevant to biological systems where NaN_3 is often used to inactivate microbial growth [111,112] .

In the absence of H_2O_2, interactions between EBS and *tert*-butanol were not observed during irradiation experiments with 0 and 50 mM *tert*-butanol (p = 0.71, ANCOVA). In the UV-H_2O_2 process, however, enhanced degradation of EBS was observed when *tert*-butanol was used as a $^{\bullet}OH$ quencher. Schewe [54] and Kamigata *et al.* [113] suggested that the secondary organic radicals (*e.g.*, $R^{\bullet}$ and $ROO^{\bullet}$) formed by *tert*-butanol reaction with $^{\bullet}OH$ would react with EBS. From Figure 2.5b, the observed rate constants for direct photolysis of EBS at 254 nm, UV-H_2O_2 treatment of EBS, and UV-H_2O_2 treatment of EBS in the presence of *tert*-butanol were 2.37 (± 0.20) × 10^{-3} s^{-1}, 2.03 (± 0.13) × 10^{-2} s^{-1}, and 4.16 (± 0.16) × 10^{-3} s^{-1}, respectively. Three concentrations of *tert*-butanol, namely 10, 50, and 100 mM, were used to ensure that the enhanced degradation was not from residual $^{\bullet}OH$. In all three cases, the observed rate constants were similar (see Figure 2.5b), suggesting efficient quenching of $^{\bullet}OH$ by *tert*-butanol and confirming EBS reaction with secondary organic radicals.

The reported data highlight the complex photochemistry of organoselenium compounds, which are being increasingly used for pharmaceutical applications and represent unique contaminants of emerging concern. More studies on EBS occurrence in water resources and fate in biological and photochemical processes are needed to determine EBS persistence, and potential toxicity outcomes, in the environment. The fast phototransformation kinetics reported here suggest EBS does not persist in engineered or natural systems. However, conventional protocols would have overestimated EBS degradation because the chemicals used for sensitizing and quenching reactive species exhibited convoluted effects on EBS photodegradation due to generation of kinetically-relevant active intermediates (*i.e.*, isopropanol, NaN_3, PN, RB, sorbic acid, *tert*-butanol) or direct reaction with EBS (*i.e.*, H_2O_2, isopropanol). These complications stem from the antioxidant properties of organoselenium chemicals. RB- and PN-sensitized reactions were partially quenched with NaN_3, but the quenching efficiency was lower at higher pH for both $^1O_2$ sensitizers, potentially due to EBS reduction by $O_2^{\bullet-}$. The high reactivity of EBS with active intermediates will also affect the assessment of EBS degradation during photocatalysis [114], ozonation [114], and other processes involving reactive species. Overall, the complex reactions of EBS with commonly employed reactive species sensitizers, scavengers, and quenchers presented in this study will provide insight into future research of organoselenium chemicals in the environment. For the same reasons, EBS may serve as an advantageous quenching agent that can be adopted for a variety of reactive oxygen species.

2.4 Acknowledgments

We acknowledge funding from the National Science Foundation (CHE 1508090).

Chapter 3 Photolysis of triphenyltin chemicals: determination of rate constants and prediction of photodegradation in different source waters

Abstract

Triphenyltin hydroxide (TPTH) is an organotin fungicide on the Environmental Protection Agency's contaminant candidate list that causes endocrine disruption and developmental malformations in aquatic organisms. The objective of this study was to determine TPTH photodegradation mechanisms and kinetics in different water sources. For solar irradiation, direct photolysis of TPTH was negligible due to its low absorbance at wavelengths greater than 270 nm. Indirect photolysis of TPTH proceeded through reactions with photogenerated singlet oxygen ($^1O_2$), hydroxyl radicals (•OH), and excited triplet states of dissolved organic matter ($^3DOM^*$). The apparent second-order rate constants for TPTH reaction with $^1O_2$ and $^3DOM^*$ were calculated to be $(3.9 \pm 0.5) \times 10^6$ M^{-1} s^{-1} and $(1.41 \pm 0.06) \times 10^6$ M^{-1} s^{-1}, respectively, at pH 7; note, the TPTH rate constant for reaction with •OH was previously reported. Based on the calculated rate constants and typical reactive species concentrations in surface water, $^1O_2$, •OH, and $^3DOM^*$ were determined to be important reaction mechanisms for TPTH photodegradation. The measured rate constants were input to the Aqueous Photochemistry of Environmentally occurring Xenobiotics (APEX) photochemical model to predict TPTH photodegradation kinetics in surface water, wastewater effluent, stormwater, wetlands, and natural organic matter (NOM) extracts. The half-lives and pseudo-first-order rate constants for TPTH photodegradation were assessed as a function of DOM content and water depth for 1380 different DOM sources. Under summertime irradiation conditions at mid-latitudes in 1 m

deep water with 5 mg_C L^{-1} DOM, the median half-lives of TPTH followed the order: wetlands (60 sunny summer days, or SSD) < stormwater (74 SSD) < wastewater effluent (95 SSD) < NOM extracts (151 SSD) < surface water (157 SSD). Therefore, the DOM in water bodies subjected to TPTH contamination, namely agricultural wetlands, wastewater effluent, and harbors affected by stormwater runoff, facilitates relatively fast TPTH photodegradation.

3.1 Introduction

Triphenyltin chemicals are broadly used as fungicides and miticides in agriculture to protect beets, pecans, potatoes, rice, and other food crops [20,115,116]. Along with butyltin compounds, triphenytins have been added to antifouling paints as non-target biocides that prevent the growth of algae and barnacles on ship hulls [117-119]. Due to the toxic effects of organotins on marine organisms, the use of these chemicals in shipping paints has been banned in several locations, including the European Union, Japan, United States (US), and others [45,117]. However, organotins, such as triphenyltin acetate (TPTA), triphenyltin chloride (TPTC), and triphenyltin hydroxide (TPTH), are still registered as fungicides by the US Environmental Protection Agency (EPA) and widely used as pesticides around the world [120]. As a result of their legacy use in shipping paints and ongoing use as pesticides, triphenyltin compounds have been detected in surface water, sediment, and aquatic organisms [121,122]. A recent survey by Gao *et al.* [123] identified triphenyltin concentrations as high as 11.3 ng Sn L^{-1} in the Three Gorges Reservoir (China), which serves as an important source of drinking and irrigation water. Harino *et al.* [124] reported 0.97 μg Sn kg^{-1} (dry weight) of triphenyltin in sediment from Otsuchi Bay, Japan. Triphenyltin levels

ranged from 0.3 to 3.1 μg Sn kg^{-1} (wet weight) in clams (*Meretrix* spp.) collected from coastal areas of Vietnam [125]. These detections suggest that even after restricted use, triphenyltin chemicals are persistent in the environment and accumulate in the food web [126]. The occurrence of triphenyltins in the environment warrants investigation of critical knowledge gaps on the fate of these unique chemicals in water systems.

Understanding the fate of triphenyltin compounds in the environment is essential because these chemicals cause developmental malformations and endocrine disruption, such as imposex in gastropods, fish, and frogs, at nanomolar concentrations [127-130]. For example, in a 96-h exposure study with a marine copepod (*Tigriopus japonicus*), Yi *et al.* [131] reported a half-maximal lethal concentration of 6.3 μg L^{-1} for TPTC. The authors also observed delayed development and reduced population growth in a chronic full-lifecycle experiment conducted with 1.0 μg L^{-1} of TPTC [131]. Adding to these concerns, triphenyltin chemicals cause reproductive toxicity in mammals and are potential endocrine disruptors in humans [43]. Recently, the US EPA added TPTH to the Contaminant Candidate List 4 [47] and recognized TPTH as a group B2 (probable human) carcinogen [47,120]. These toxicity concerns reinforce the need to improve understanding of triphenyltin fate in aquatic systems to protect both ecological and human health.

A few studies have explored the environmental fate of triphenytin compounds by hydrolysis [132,133], biodegradation [134], and phototransformation [135,136]. Importantly, the literature has indicated that TPTA and TPTC undergo rapid hydrolysis to form TPTH [132,133], suggesting that the environmental fate of the dominant triphenyltin chemicals can

be determined via targeted study of TPTH. Compared to biodegradation, phototransformation was identified as the faster degradation pathway for triphenyltins in surface water [117]. However, previous studies did not identify the reaction mechanisms or deconvolute the apparent degradation kinetics [135-137]. For these reasons, a detailed evaluation of the photochemical reaction mechanisms and kinetics is warranted to improve understanding of direct and indirect photolysis of triphenyltins in the environment.

Given the various routes by which triphenyltin chemicals can enter environmental systems (*e.g.,* direct release from antifouling paints, agricultural runoff, wastewater effluent, landfill leachate, and stormwater), the photochemistry of the water source also plays a significant role in the fate of organtin chemicals. Dissolved organic matter (DOM) present in the source water affects the fate and transport of aquatic contaminants through a variety of processes [91]. Upon irradiation, a number of photochemically generated reactive intermediates, such as excited triplet states of DOM ($^3DOM^*$), singlet oxygen ($^1O_2$), and hydroxyl radicals ($^\bullet OH$), are produced from DOM or other constituents (*e.g.*, nitrate/nitrite) [8,138]. The yield of these reactive species depends on the DOM content, DOM composition, and other water quality parameters (*e.g.*, nitrite (NO_2^-), nitrate (NO_3^-), bicarbonate (HCO_3^-), and carbonate (CO_3^{2-}) concentrations) that differ between water sources [139,140]. Photochemically generated reactive species can degrade organometallic chemicals [8,9,53], but the degradation kinetics of triphenyltin compounds with $^3DOM^*$, $^1O_2$, and $^\bullet OH$, and the corresponding influence of source water photochemistry, have not been established.

To fill these knowledge gaps, photochemical experiments and the Aqueous Photochemistry of Environmentally occurring Xenobiotics (APEX) model were cohesively employed to investigate the reaction mechanisms and degradation kinetics of triphenyltin chemicals in different source waters. The overall goals of this study were as follows: (1) determine the phototransformation kinetics of TPTH by measuring the direct photolysis quantum yield and second-order rate constants for reaction with $^1O_2$, •OH, and $^3DOM^*$; (2) employ the APEX model to predict the photochemical fate of TPTH and calculate the half-lives ($t_{½}$) and pseudo-first-order rate constants ($k'_{app,TPTH}$) of TPTH in surface water, wastewater effluent, stormwater, wetlands, and natural organic matter (NOM) extracts; and, (3) identify the influence of source water photochemistry and the overall contributions of direct photolysis, $^1O_2$, •OH, and $^3DOM^*$ to TPTH degradation. The outcomes of this study will improve understanding of TPTH fate in water sources impacted by both point (*e.g.*, harbors containing triphenyltin from antifouling paint, wastewater effluent) and non-point sources (*e.g.*, agricultural runoff into wetlands and streams).

3.2 Material and Methods

3.2.1 Chemicals and materials

TPTA (> 96%), TPTC (> 95%), and TPTH (> 98%) were purchased from Sigma-Aldrich (St. Louis, MO, USA), and a 1 g L^{-1} stock solution was generated for each triphenyltin in high-performance liquid chromatography (HPLC) grade methanol. Sodium phosphate monobasic monohydrate (> 98%), sodium phosphate dibasic heptahydrate (> 98%), and

sodium phosphate tribasic dodecahydrate (> 98%) were obtained from Fisher Scientific (Hampton, NH, USA) and used to control the pH of experimental solutions. A number of other chemicals were acquired for use in photochemical experiments: furfuryl alcohol (> 95%) from Fisher Scientific; and, 4-benzoylbenzoic acid (99%, CBBP), Rose Bengal (88%), and sodium anthraquinone-2-sulfonate (> 98%, AQ2S) from Sigma-Aldrich.

3.2.2 Analytical methods

TPTA, TPTC, and TPTH were analyzed by liquid chromatography with triple quadrupole tandem mass spectrometry (LC-MS/MS; Thermo UltiMate 3000 with Quantum Access Max). Samples (10 μL) were injected onto a Waters Symmetry C18 column (2.1×150 mm, 3.5 μm) maintained at 40 °C. The isocratic mobile phase was comprised of a 40:60 (v/v) mixture of (A) 0.1% formic acid in LC-MS-grade water and (B) LC-MS-grade methanol with 0.1% formic acid. The flow rate was 200 μL min^{-1}. The electrospray ionization unit was operated in positive mode for TPTA, TPTC, and TPTH. Other MS/MS operating parameters for TPTA, TPTC, and TPTH analysis were as follows: capillary temperature, 270 °C; spray voltage, 3000 V; sheath gas pressure, 40 (arbitrary units); auxiliary gas pressure, 15 (arbitrary units); and, collision gas (argon) pressure, 1.5 Torr. The monitored ion transitions for TPTA, TPTC, and TPTH were 383.01 → 350.9, 383.01 → 350.9, and 383.01 → 350.9, respectively; note, the ion transitions for TPTA, TPTC, and TPTH are identical because TPTA and TPTC underwent rapid hydrolysis to form TPTH in solution [117].

Furfuryl alcohol was analyzed by HPLC with UV absorbance detection (HPLC-UV; Thermo UltiMate 3000) at 220 nm. The sample injection volume was 50 μL, and the mobile phase flow rate was maintained at 600 μL min^{-1}. The method employed an isocratic mobile phase consisting of a 25:75 (v/v) mixture of (A) HPLC-grade methanol with 0.1% formic acid and (B) HPLC-grade water with 0.1% formic acid. Chromatographic separation was carried out on an Accucore C18 column (4.6×150 mm, 2.6 μm) maintained at 40 °C. The retention time of furfuryl alcohol was 6.6 min.

3.2.3 Photochemical experiments

Given the fate of other organometallic contaminants in surface water systems [8,53], the photodegradation mechanisms for TPTH were expected to involve direct photolysis and indirect photolysis by $^1O_2$, $^{\bullet}OH$, and $^3DOM^*$. A Rayonet reactor equipped with bulbs emitting light in the 310-410 nm range (and centered at 365 nm) was used to evaluate the direct photolysis, $^1O_2$, and $^3DOM^*$ kinetics; note, the reaction kinetics of TPTH with $^{\bullet}OH$ were determined as described in Chapter 4 and, therefore, not included here. The 310-410 nm range represents the energetic domain of sunlight responsible for degradation of organic contaminants in surface water. The average incident photon flux was calculated to be 1.9 (± 0.2) × 10^{-5} Ein L^{-1} s^{-1} with the ferrioxalate actinometer [75]. Direct photolysis solutions (10 mL) contained 2.7 μM TPTH and 5 mM phosphate buffer (pH 7.0 ± 0.2) in deionized (DI) water. Dark controls were included to correct for potential hydrolysis reactions. All experiments were carried out at room temperature (22 ± 1 °C). Experimental samples were collected at predetermined times, added to amber LC vials, and stored at -20 °C before analysis.

The photochemical reactivity of TPTH with $^1O_2$ was determined by competition kinetics in solutions containing the Rose Bengal photosensitizer and the furfuryl alcohol probe molecule. The experimental solutions initially contained 2.7 μM TPTH, 30 μM Rose Bengal, 200 μM furfuryl alcohol, and 5 mM phosphate buffer (pH 7.0 ± 0.2) in DI water. The steady-state $^1O_2$ concentration (*i.e.*, $[^1O_2]_{ss}$) and second-order rate constant for TPTH reaction with $^1O_2$ ($k''_{^1O_2,TPTH}$) were determined according to Eq. 3.1 and Eq. 3.2, respectively.

$$\left[{}^1O_2\right]_{ss} = \frac{k'_{obs,FFA}}{k''_{^1O_2,FFA}} \quad \text{(Eq. 3.1)}$$

$$k''_{^1O_2,TPTH} = \frac{k'_{obs,TPTH}}{\left[{}^1O_2\right]_{ss}} \quad \text{(Eq. 3.2)}$$

In Eq. 3.1-3.2, $k'_{obs,FFA}$ (s^{-1}) and $k'_{obs,TPTH}$ (s^{-1}) are the observed pseudo-first-order rate constants for furfuryl alcohol and TPTH degradation, respectively, and $k''_{^1O_2,FFA}$ is the second-order rate constant for furfuryl alcohol reaction with $^1O_2$ (1.0×10^8 M^{-1} s^{-1} [76]).

CBBP and AQ2S were used as surrogates to determine the second-order rate constant for TPTH reaction with $^3DOM^*$. CBBP has a reduction potential of 1.8 V_{SHE}, which is representative of typical DOM sources (1.4-1.9 V_{SHE}) [140]; however, CBBP produces

potentially interfering transients upon irradiation. To confirm the role of ^{3}DOM*, laser flash photolysis [53,87] was used to measure ^{3}CBBP* quenching by TPTH. Prior to laser flash photolysis, 2 mL of 100 μM CBBP in 5 mM phosphate-buffered DI water at pH 7.0 ± 0.1 was sparged with argon for 15 min to remove dissolved oxygen. Selective excitation of CBBP was carried out at 355 nm, where TPTH does not absorb, and the time-dependent change in absorbance of ^{3}CBBP* was monitored at 550 nm. Aliquots (10 μL) of TPTH in 50% acetonitrile were added to the CBBP solution to achieve a total concentration of 90 μM. To avoid photobleaching, the CBBP solution was replaced for every sequential increase in TPTH concentration. The 550-nm decay traces of ^{3}CBBP* were fit to an exponential model to determine the pseudo-first-order decay constant ($k'_{^3\mathrm{CBBP}^*}$) for each TPTH concentration [87,142]. The second-order rate constant for ^{3}CBBP* quenching by TPTH was calculated using a Stern-Volmer plot.

The reactivity of TPTH with ^{3}AQ2S* was evaluated by irradiating 3-24 μM TPTH and 100 μM AQ2S in phosphate-buffered DI water at pH (7.0 ± 0.2). In this solution, AQ2S was the primary light-absorbing molecule, because TPTH exhibited minimal absorbance above 270 nm. Therefore, the photon flux according to AQ2S (I_{AQ2S}, Ein L^{-1} s^{-1}) can be calculated using Eq. 3.3 [143].

$$I_{AQ2S} = \int_{\lambda=310\ \mathrm{nm}}^{\lambda=410\ \mathrm{nm}} I_0(\lambda)[1 - 10^{-\varepsilon_{AQ2S}(\lambda)\,\ell\,[AQ2S]}]d\lambda \qquad \text{(Eq. 3.3)}$$

In Eq. 3.3, $I_0(\lambda)$ is the net photon flux (Ein L^1 s^{-1}) determined by ferrioxalate actinometry, ε_{AQ2S} (λ) is the apparent molar absorption coefficient of AQ2S (M^{-1} cm^{-1}), and ℓ is the optical pathlength (cm).

Under steady-state conditions, the rate of formation of ^{3}AQ2S* ($R_{^3AQ2S^*}$, M s^{-1}) is equal to the product of I_{AQ2S} and the quantum yield of triplet formation ($\phi_{^3AQ2S^*}$ = 0.18 mol Ein^{-1} [143]), as shown in Eq. 3.4.

$$R_{^3AQ2S^*} = \phi_{^3AQ2S^*} I_{AQ2S} \quad \text{(Eq. 3.4)}$$

The ^{3}AQ2S* species quickly reacts with water, and the deactivation rate constant ($k'_{^3AQ2S^*,H_2O}$) is 1.1×10^7 s^{-1} [143]. As a result, TPTH must compete with H_2O for reaction with ^{3}AQ2S*. The rate of TPTH transformation by ^{3}AQ2S* ($R_{^3AQ2S^*,TPTH}$) can, therefore, be expressed by Eq. 3.5.

$$R_{^3AQ2S^*,TPTH} = \phi_{^3AQ2S^*} I_{AQ2S} \left(\frac{k''_{^3AQ2S^*,TPTH}\,[TPTH]}{k'_{^3AQ2S^*,H_2O} + k''_{^3AQ2S^*,TPTH}\,[TPTH]} \right) \quad \text{(Eq. 3.5)}$$

In Eq. 3.5, $k''_{^3AQ2S^*,TPTH}$ is the second-order rate constant for TPTH reaction with ^{3}AQ2S*.

Due to the much higher concentration of H_2O in the experimental solutions, $k'_{^3AQ2S^*,H_2O}$ was assumed to be much greater than $\left(k''_{^3AQ2S^*,TPTH}\,[TPTH]\right)$, allowing simplification of Eq. 3.5 to Eq. 3.6. Then, the second-order rate constant for TPTH reaction with $^3AQ2S^*$ was calculated as the slope of $R_{^3AQ2S^*,TPTH}$ vs. $\left(\frac{\Phi_{^3AQ2S^*}\, I_{AQ2S}}{k'_{^3AQ2S^*,H_2O}}\,[TPTH]\right)$ [143].

$$R_{^3AQ2S^*,TPTH} = k''_{^3AQ2S^*,TPTH}\left(\frac{\Phi_{^3AQ2S^*}\, I_{AQ2S}}{k'_{^3AQ2S^*,H_2O}}\,[TPTH]\right) \quad \text{(Eq. 3.6)}$$

3.2.4 Photochemical modeling

TPTH phototransformation was estimated for different source waters using the freely available APEX model [144], which has been validated for a number of organic contaminants [145-148]. The APEX model predicts the photochemical half-life, pseudo-first-order degradation rate constant, and contribution of each reaction pathway (*e.g.*, direct photolysis, $^1O_2$, $^\bullet OH$, $^3DOM^*$) for an organic contaminant as a function of water chemistry (*e.g.*, DOM, NO_2^-, NO_3^-, HCO_3^-, and CO_3^{2-} concentrations) and depth. APEX uses the spectral photon flux density for a fair-weather July 15 day at 45° N latitude (defined as a sunny summer day, SSD) and a UV irradiance of 22 W m^{-2}. The outputs are averaged over the water column depth entered by the user.

The TPTH-specific input parameters included the molar absorption spectrum (WS1 in the SI), direct photolysis quantum yield (negligible for TPTH due to minimal absorbance above 270 nm), and the second-order rate constants with reactive species (measured according to protocols in Section 3.2.3). The main system input parameters, namely the quantum yields of $^1O_2$ ($\phi_{^1O_2}$), $^\bullet$OH ($\phi_{^\bullet OH}$), and $^3DOM^*$ ($\phi_{^3DOM^*}$), were obtained for whole waters and NOM extracts from the database published by Wasswa *et al.* [139]. The other water quality parameters were selected based on typical concentrations available from literature: 10^{-6} M NO_2^-; 10^{-4} M NO_3^-; 10^{-3} M HCO_3^-; and, 10^{-5} M CO_3^{2-} [140,143,146]. Note, the bicarbonate/carbonate ratio was approximated by considering an air-equilibrated water system at pH 7.5. To facilitate comparison of TPTH phototransformation kinetics in water sources with different DOM, the water quality parameters were maintained at the aforementioned concentrations for all model runs. For each DOM source, the photochemical degradation kinetics of TPTH were assessed as a function of two independent variables, namely DOM concentration (1-20 mg_C L^{-1}) and water column depth (1-5 m).

3.3 Results and Discussion

3.3.1 Direct and indirect photolysis of TPTH

For direct photolysis to occur, the absorption of TPTH must overlap with the lamp's emission spectrum (*i.e.*, 310-410 nm). Figure B16 in Appendix B shows that TPTH exhibited low molar absorption coefficients (< 10 M^{-1} cm^{-1}) above 270 nm. In addition, a 24-h irradiation experiment in DI water revealed negligible TPTH degradation (Figure

B17 in Appendix B). Based on these results, direct photolysis of TPTH was not considered to be a kinetically relevant degradation mechanism.

Indirect photolysis by photogenerated reactive species, such as $^1O_2$, •OH, and $^3DOM^*$, often controls the fate of organic contaminants in surface water [91,149]. To measure the second-order rate constant for TPTH reaction with $^1O_2$, the Rose Bengal sensitizer and furfuryl alcohol probe molecule were added to experimental solutions. Using the data in Figure 3.1 with Eq. 3.1-3.2, $k''_{^1O_2,TPTH}$ was calculated to be $(3.9 \pm 0.5) \times 10^6$ M^{-1} s^{-1} at pH 7.0 ± 0.2. Similar second-order rate constants have been reported for degradation of other pesticides with $^1O_2$: 5×10^6 M^{-1} s^{-1} for amicarbazone (triazole herbicide) [148]; $(5.5 \pm 0.5) \times 10^6$ M^{-1} s^{-1} for imidacloprid (neonicotinoid pesticide); and, $(1.3 \pm 1.0) \times 10^6$ M^{-1} s^{-1} for acetamiprid (neonicotinoid pesticide) [93]. These rate constants are considered to be slow for typical environmental conditions [148,150]. As environmental concentrations of $^1O_2$ typically range from 10^{-14} to 10^{-12} M [139,151], the contribution of $^1O_2$ to TPTH degradation was $(3.9–390) \times 10^{-8}$ s^{-1}. Therefore, the half-life of TPTH is 2-205 d due to reaction with photochemically generated singlet oxygen.

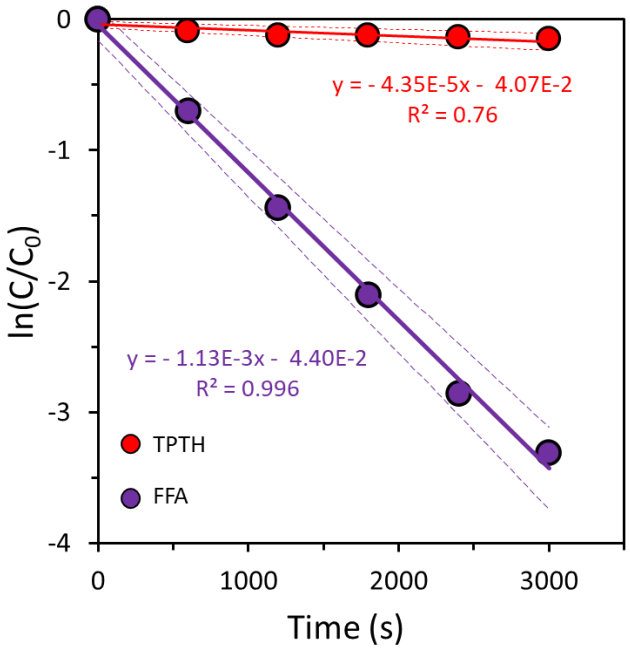

Figure 3.1. Observed degradation of TPTH and furfuryl alcohol (FFA) for irradiation at 365 nm. The experimental solutions initially contained 2.7 µM TPTH, 30 µM Rose Bengal, 200 µM FFA, and 5 mM phosphate buffer (pH 7.0 ± 0.2). The slopes (observed rate constants, solid lines) obtained from this plot were used to calculate the second-order rate constant for TPTH with $^1O_2$ (see Eq. 3.1-3.2). The dashed lines represent the upper and lower 95% confidence limits.

As reported in Chapter 4, the second-order rate constant for TPTH reaction with •OH was (7.81 ± 0.37) × 10^8 M^{-1} s^{-1}. A wide range of second-order rate constants for degradation of other pesticides with •OH has been reported in the literature: carbamates and thiocarbamates, 8.5 × 10^8–1.3 × 10^{10} M^{-1} s^{-1}; chlorophenoxy pesticides, 1.6 × 10^9 – 3.8 × 10^{10} M^{-1} s^{-1}; organochlorines, 3.6-8.6 ×10^9 M^{-1} s^{-1}; and, triazines, 3.0 × 10^7–1.0 × 10^{10} M^{-1} s^{-1} [152]. The rate constant for TPTH overlaps with other pesticides, indicating similar reactivity. While the rate constant reported for TPTH suggests the rapid degradation of TPTH by •OH, the steady-state concentrations of •OH in surface water are relatively low (*e.g.*, 10^{-17} to 10^{-15} M [139,153]), resulting in pseudo-first-order rate constants of (7.81–781) × 10^{-9} s^{-1}. Therefore, TPTH degradation by •OH is an order of magnitude slower than by

$^1O_2$, which is reinforced by the 10-1027 d half-life of TPTH for reaction with photochemically generated •OH.

The reactivity of TPTH with $^3DOM^*$ was assessed using CBBP and AQ2S as DOM surrogates. CBBP, which is an aromatic ketone with a triplet reduction potential of 1.8 V_{SHE}, has been demonstrated to be a representative proxy for $^3DOM^*$ [91,154]. Using laser flash photolysis, the decay of $^3CBBP^*$ was monitored in the presence of variable TPTH concentrations; however, the measured first-order decay rate constant ($k'_{^3CBBP^*}$) exhibited no dependence on TPTH concentration (Figure 3.2a and Figure B18 of Appendix B). This result suggests that TPTH did not react with $^3CBBP^*$, because the increasing TPTH concentration would have otherwise resulted in quicker quenching of $^3CBBP^*$. Wenk *et al.* [155] reported a similar phenomenon for DOM reaction with $^3CBBP^*$; however, their explanation involved electrostatic repulsion of DOM and $^3CBBP^*$, which was not expected in this case since TPTH is neutral at pH 7. Given these results, AQ2S was used to further assess and confirm the reactivity of TPTH with $^3DOM^*$.

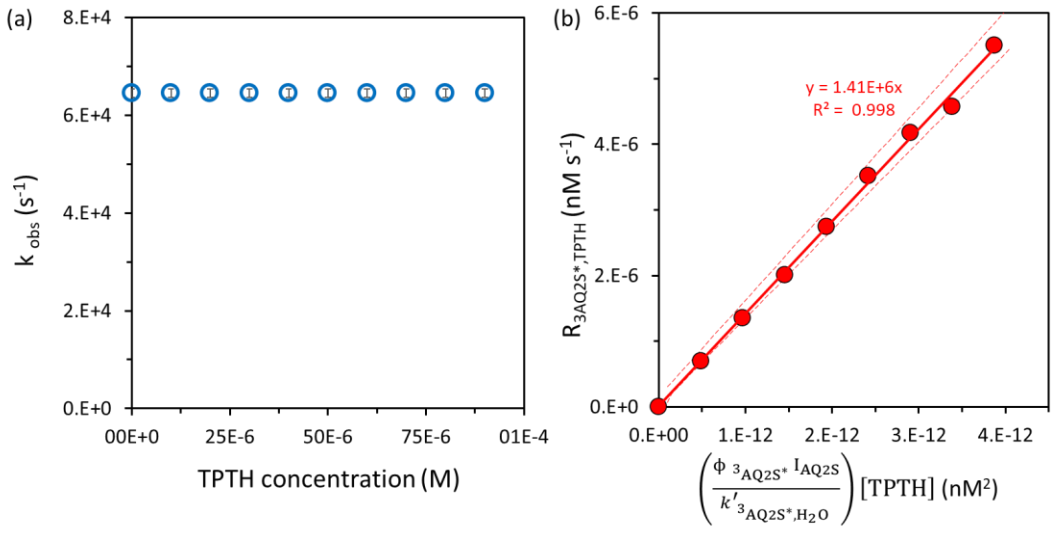

Figure 3.2. TPTH reaction with (a) ^{3}CBBP* and (b) ^{3}AQ2S*. The Stern-Volmer plot in (a) shows the decay rate constant of ^{3}CBBP* as a function of TPTH concentration. Solutions containing 100 µM CBBP in 5 mM phosphate buffer (pH 7.0) were irradiated with light at 355 nm. Prior to irradiation, the solutions were bubbled with argon gas for 15 min to eliminate dissolved oxygen and prevent formation of other transient species. The second-order rate constant for TPTH reaction with ^{3}CBBP* was not calculated due to the absence of a linear relationship between the observed rate constant for ^{3}CBBP* decay and TPTH concentration. Error bars represent the 95% confidence for the exponential decay fit to the transient absorbace data shown in Figure B3. In (b), the initial degradation rates of TPTH ($\mathbf{R}_{^3\mathbf{AQ2S}^*,\mathbf{TPTH}}$) were used to solve for the second-order rate constant of TPTH with ^{3}AQ2S*. The initial TPTH concentrations ranged from 3 to 24 µM, and the solution pH was adjusted to 7.0 ± 0.1 with 5 mM phosphate buffer. The experimental solutions contained 100 µM AQ2S and were irradiated with light at 365 nm. The solid line is the mean slope of the aggregate data, and the dashed lines represent the upper and lower 95% confidence limits.

AQ2S contains a quinone moiety, which is abundant in natural DOM matrices and plays a critical role in the photochemistry of ^{3}DOM* [156,157]. Unlike other triplet sensitizers (*e.g.*, CBBP, perinaphthenone, riboflavin), AQ2S does not generate reactive oxygen species during irradiation [158]. Instead, ^{3}AQ2S* reacts with water to form adducts that decompose into hydroxyderivatives without producing •OH. The ^{3}AQ2S* reaction with water outcompetes oxygen quenching, thereby preventing $^1O_2$ formation [143,157]. Given this chemistry, the reaction kinetics of TPTH degradation by ^{3}AQ2S* were assessed in bulk solution. Figure 3.2b shows the initial rate of TPTH (3-27 µM) degradation in solutions

containing 100 μM AQ2S at pH (7.0 ± 0.1) for irradiation at 365 nm. The slope of the plot corresponds to the second-order rate constant for TPTH reaction with ^{3}AQ2S*, namely (1.41 ± 0.06) × 10^6 M^{-1} s^{-1}. Note, this rate constant satisfied the assumption, $\left(k''_{^3\text{AQ2S}^*,\text{TPTH}}\,[\text{TPTH}]\right) \ll k'_{^3\text{AQ2S}^*,\text{H}_2\text{O}}$, that was applied to simplify Eq. 3.5 to Eq. 3.6. Carena *et al.* [140] determined the second-order rate constant of atrazine (herbicide) with ^{3}AQ2S* to be (1.43 ± 0.07) × 10^9 M^{-1} s^{-1}, which is three orders of magnitude higher than the rate constant determined for TPTH, indicating slow reactivity of TPTH with ^{3}DOM*. Given typical steady-state ^{3}DOM* concentrations (10^{-14} to 10^{-12} M [91]) in surface water, the pseudo-first-order rate constant for TPTH with ^{3}DOM* was (1.41–141) × 10^{-8} s^{-1}, similar to the $^1O_2$ contribution. Therefore, the half-life of TPTH is 6-568 d due to reaction with photochemically generated triplet excited ^{3}DOM*.

The apparent photodegradation rate constant for TPTH can be written according to Eq. 3.7 [138]. By substituting the calculated second-order rate constants and the typical steady-state concentrations of $^1O_2$ (10^{-13} M), •OH (10^{-16} M), and ^{3}DOM* (10^{-13} M) in surface water, the apparent first-order rate constant for TPTH degradation was estimated for a typical water in Eq. 3.8.

$$k'_{\text{app,TPTH}} = k''_{^1\text{O}_2,\text{TPTH}}\left[\,^1\text{O}_2\right]_{\text{ss}} + k''_{\cdot\text{OH,TPTH}}\left[\cdot\text{OH}\right]_{\text{ss}} + k''_{^3\text{DOM}^*,\text{TPTH}}\left[\,^3\text{DOM}^*\right]_{\text{ss}} \quad \text{(Eq. 3.7)}$$

$$k'_{\text{app,TPTH}} = 3.90 \times 10^{-7}\ s^{-1} + 7.81 \times 10^{-8}\ s^{-1} + 1.41 \times 10^{-7}\ s^{-1} = 6.09 \times 10^{-7}\ s^{-1} \quad \text{(Eq. 3.8)}$$

According to previous studies for other organic contaminants [150,159], the pseudo-first-order rate constant (*i.e.*, 6.09×10^{-7} s^{-1}) indicates that TPTH photodegradation is relatively slow in the environment. Based on the similar magnitude of the three terms in Eq. 3.8, all three reactive species are expected to be involved with TPTH degradation in surface water. However, the steady-state concentrations of $^1O_2$, $^{\bullet}OH$, and $^3DOM^*$ are highly dependent on the source water quality and the corresponding DOM concentration and composition. The aforementioned rate constants were, therefore, employed in the APEX model to evaluate the impacts of DOM source and content on the overall photodegradation kinetics of TPTH in real waters.

3.3.2 Photochemical modeling of TPTH degradation in different source waters

The negligible direct photolysis and relatively slow indirect photolysis of TPTH pose logistical challenges to comprehensive laboratory studies on the photochemical half-life of TPTH in different source waters. For this reason, APEX model simulations were run to inform TPTH photodegradation kinetics at different water quality conditions. This approach was supported by previous efforts, which highlighted the ability of APEX to accurately estimate the photodegradation kinetics of slow-reacting organic contaminants with acceptable uncertainty [148,158,160]. The APEX model requires the user to input the quantum yields of formation for $^1O_2$, $^{\bullet}OH$, and $^3DOM^*$. These parameters are a function of the DOM matrix, which is a complex mixture of chromophores that differs according to source, season, and water chemistry [161]. The photochemical reactivity of $^3DOM^*$ is also highly variable between sources, mainly due to differences in excited state energies,

redox potentials, and surface charge conditions [149]. These properties also affect the production and steady-state concentrations of $^1O_2$ and •OH [162]. Fortunately, Wasswa *et al.* [139] compiled an extensive body of literature on the quantum yields of $^1O_2$, •OH, and $^3DOM^*$ for over 1308 whole waters and NOM extracts. These parameters were used to run model simulations for TPTH photodegradation in real source waters.

Using the data from Wasswa *et al.* [139], the quantum yields for the three reactive species were plotted as box-and-whisker diagrams in Figure B19 of Appendix B for surface water, wastewater effluent, stormwater, wetlands, and NOM extracts. Several individual sources contained quantum yields for all three reactive species; however, the values of $\phi_{^1O_2}$ (535/1308), $\phi_{\bullet OH}$ (928/1308), or $\phi_{^3DOM^*}$ (412/1308) were missing for many source waters. Because $^3DOM^*$ transfers energy to molecular oxygen to produce $^1O_2$ [139,155,163], the $\phi_{^1O_2}$ and $\phi_{^3DOM^*}$ parameters demonstrated a strong correlation (Figure B20 in Appendix B). For this reason, any missing $\phi_{^1O_2}$ or $\phi_{^3DOM^*}$ values from the Wasswa *et al.* [139] dataset were estimated by linear correlation. No convincing correlations were observed for $\phi_{\bullet OH}$ with $\phi_{^1O_2}$ or $\phi_{^3DOM^*}$ (Figure B21 in Appendix B), presumably due to the presence of other •OH precursors and variable scavenger concentrations between the source waters [155]. Given the relatively narrow range of $\phi_{\bullet OH}$, missing values from the Wasswa *et al.* [139] dataset were estimated using the median $\phi_{\bullet OH}$ for each source water type. The resultant distribution of the quantum yields of $^1O_2$, •OH, and $^3DOM^*$ are given as 10th, 50th, and 90th percentiles in Table 3-1. Wetlands demonstrated the highest median $\phi_{^1O_2}$ (6.39×10^{-2} mol Ein^{-1}), stormwater had the highest median $\phi_{^3DOM^*}$ (4.83×10^{-2} mol Ein^{-1}), and wastewater effluent exhibited the highest median $\phi_{\bullet OH}$ (80.6×10^{-6}

mol Ein^{-1}). NOM extracts had the lowest median $\phi_{^3DOM^*}$ (1.92×10^{-2} mol Ein^{-1}) and $\phi_{^1O_2}$ (2.00×10^{-2} mol Ein^{-1}), whereas the lowest median $\phi_{\bullet OH}$ was reported for surface water (11.90×10^{-6} mol Ein^{-1}). These values suggest that indirect photolysis of TPTH will be fastest in wetlands, stormwater, and wastewater effluent.

Table 3-1. The distribution of reactive species quantum yields, pseudo-first-order rate constants, and half-lives of TPTH in different water sources. The quantum yields were determined from the dataset reported by Wasswa *et al.* [139]. The pseudo-first-order rate constants ($k'_{app,TPTH}$) and half-lives ($t_{1/2}$) for TPTH were estimated by APEX for 1 m water depth and 5 mg_C L^{-1} DOM.

Water source	Percentile	$\phi_{^1O_2}$ ($\times 10^{-2}$ mol Ein^{-1})	$\phi_{^3DOM^*}$ ($\times 10^{-2}$ mol Ein^{-1})	$\phi_{\bullet OH}$ ($\times 10^{-6}$ mol Ein^{-1})	$k'_{app,TPTH}$ ($\times 10^{-3}$ SSD^{-1})	$t_{1/2}$ (SSD)
Surface water	10	0.98	0.76	4.32	2.20	315
	50	2.26	2.37	11.9	4.41	157
	90	4.48	5.57	139	11.1	62.5
Wastewater effluent	10	0.55	0.93	20.1	2.07	335
	50	3.24	2.18	80.6	7.29	95.1
	90	7.38	7.07	468	23.1	30.0
Wetlands	10	1.92	1.86	46.6	4.69	148
	50	6.39	4.43	63.8	11.5	60.4
	90	9.45	8.00	92.0	16.9	40.9
Stormwater	10	3.81	2.58	28.8	6.87	101
	50	5.07	4.83	41.0	9.31	74.4
	90	6.61	7.42	64.9	12.5	55.5
NOM extract	10	0.46	0.74	14.6	1.78	391
	50	2.00	1.92	37.2	4.58	151
	90	6.87	4.10	74.5	12.3	56.5

3.3.2.1 *Modeled half-lives and rate constants of TPTH*

The photochemical reaction kinetics of TPTH were modeled as a function of water depth and DOM concentration for fixed water chemistry conditions (*i.e.*, 10^{-6} M NO_2^-, 10^{-4} M NO_3^-, 10^{-3} M HCO_3^-, and 10^{-5} M CO_3^{2-}). Predicted half-lives of TPTH using individual quantum yields are reported in Figure B22. And the calculated half-lives and pseudo-first-order rate constants of TPTH are reported in Figure 3.3 for each source. Using the median quantum yields for $^1O_2$, $^\bullet OH$, and $^3DOM^*$ in Table 3-1 with a 1 m water depth and 5 mg_C L^{-1} DOM, the TPTH half-lives followed the order: wetlands (60 SSD) < stormwater (74 SSD) < wastewater effluent (95 SSD) < NOM extracts (151 SSD) < surface water (157 SSD). These findings suggest that TPTH will degrade faster in wetlands, as well as stormwater- and wastewater effluent-impacted systems, than in surface water. The modeled half-lives of TPTH in surface water sources closely matched those of NOM extracts, suggesting that laboratory studies with NOM extracts may underestimate TPTH degradation in areas affected by stormwater runoff or wastewater effluent. To simulate shallow rivers and the epilimnion of lakes, TPTH photodegradation kinetics were modeled at 1- and 5-m depths, respectively [160]. The half-life of TPTH increased with water column depth for all cases due to decreased light penetration (Figure 3.3).

The half-lives and pseudo-first-order rate constants of TPTH exhibited a strong dependence on DOM concentration, which directly influenced the steady-state concentrations of reactive species. In general, the pseudo-first-order rate constant of TPTH (i) decreased as the DOM concentration changed from 1 mg_C L^{-1} to 3 mg_C L^{-1} and

(ii) increased as the DOM concentration changed from 3 mg_C L^{-1} to 15 mg_C L^{-1} (Figure 3.3). Two primary factors contributed to these observed trends. First, DOM serves as both precursor and scavenger of •OH [164]; therefore, as the DOM concentration increases, the •OH scavenging rate will begin to outcompete the •OH formation rate [146]. Second, the steady-state concentrations of $^1O_2$ and $^3DOM^*$ increase with DOM concentration [146], enhancing the overall TPTH photodegradation kinetics at higher DOM concentrations. Due to these phenomena, the apparent pseudo-first-order rate constants of TPTH varied with DOM content for the five water sources. For example, in water with 15 mg_C L^{-1} DOM, the pseudo-first-order rate constants of TPTH in stormwater (1.5×10^{-2} SSD^{-1}) and wetlands (1.8×10^{-2} SSD^{-1}) were 1.3-1.7× higher than in surface water (6.6×10^{-3} SSD^{-1}), see Figure 3.3. This result mostly stems from the $\phi_{^1O_2}$ parameter. As indicated in Table 3-1, the $\phi_{^1O_2}$ values for stormwater and wetlands were 1.2-1.8× higher than of surface water, respectively. Similar effects were documented for $^3DOM^*$ (Figure 3.3). For stormwater and wetlands, the enhanced photodegradation of TPTH by $^1O_2$ and $^3DOM^*$ overcame the decreased contribution from •OH. However, similar compensating phenomena were not observed for surface water and NOM extracts due to the lower $\phi_{^1O_2}$ and $\phi_{^3DOM^*}$ values. These findings highlight the importance of $^1O_2$ reactions to photodegradation of TPTH in (agricultural) wetlands, wastewater effluent, and stormwater-influenced harbors.

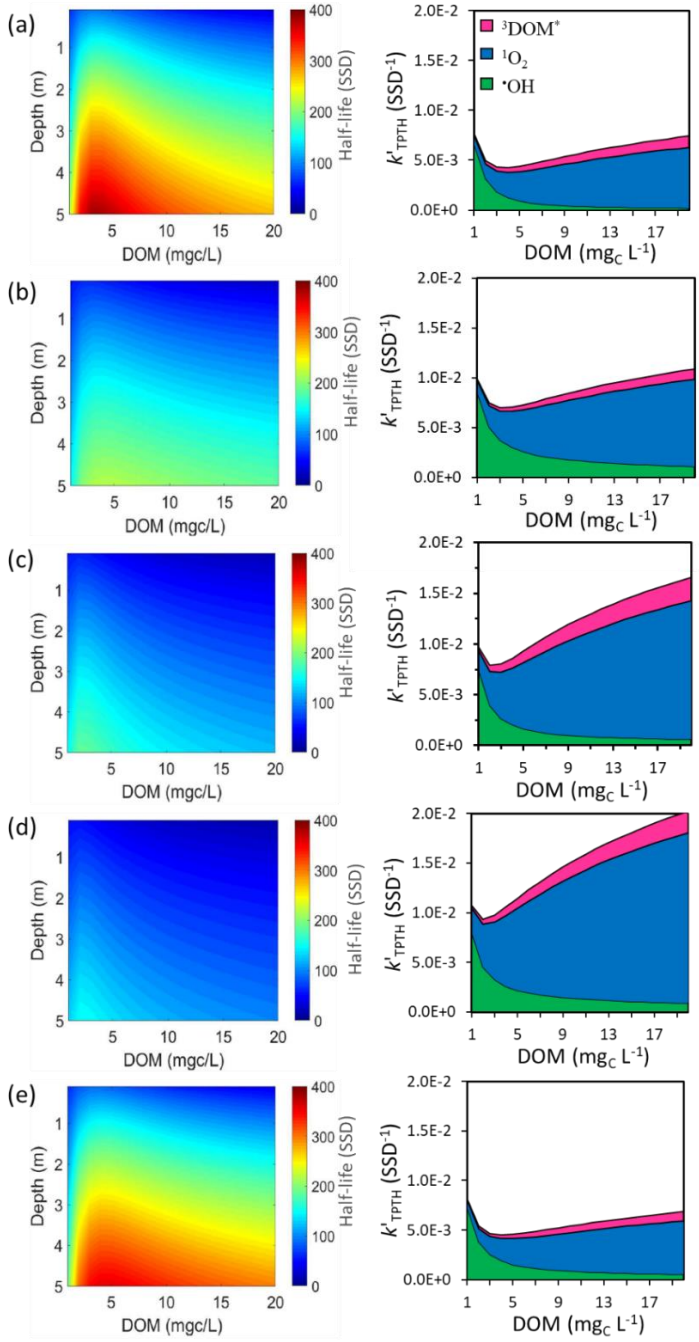

Figure 3.3. The modeled half-lives (left column) and pseudo-first-order rate constants (right column) for TPTH photodegradation in (a) surface water, (b) wastewater effluent, (c) stormwater, (d) wetlands, and (e) NOM extracts as a function of DOM concentration. The half-lives were evaluated for water depths of 1-5 m. The TPTH rate constants were modeled using the median quantum yields of $^1O_2$, •OH, and $^3DOM^*$ reported in Table 3-1 and a water depth of 1 m. Other water chemistry parameters were as follows: 10^{-6} M NO_2^-; 10^{-4} M NO_3^-; 10^{-3} M HCO_3^-; and, 10^{-5} M CO_3^{2-}. The rate constants correspond to a UV irradiance of 22 W m^{-2} at 45 °N latitude in mid-July.

3.3.2.2 *Contribution of each indirect photolysis mechanism to TPTH transformation*

Figure 3.4 reports the percent of TPTH degradation attributed to $^1O_2$, $^{\bullet}OH$, and $^3DOM^*$ for the five different water sources with 1, 5, and 10 $mg_C\ L^{-1}$ and a 1 m water depth. The $^{\bullet}OH$ contributions were high for all water sources at 1 $mg_C\ L^{-1}$ and followed the order: wetlands (65%) < stormwater (67%) < surface water (78%) < wastewater effluent (80%) < NOM extracts (83%). Interestingly, these values did not follow the order of median $\phi_{^{\bullet}OH}$ values reported in Table 3-1, but rather followed $\phi_{^1O_2}$ values. This observation could be explained by the highlights made in Section 3.3.2.1, *i.e.,* with increasing DOM concentration, hydroxyl radical contribution decreased compensated by increased contributions from $^1O_2$ and $^3DOM^*$. At 5 $mg_C\ L^{-1}$ and 10 $mg_C\ L^{-1}$, the $^1O_2$ reaction was the most important pathway, accounting for 60-81% of TPTH degradation in all water sources. The corresponding contributions of the $^{\bullet}OH$ and $^3DOM^*$ mechanisms were 7-32% and 7-13%, respectively. These findings reinforced the importance of $^1O_2$ for indirect photolysis of TPTH in environmental waters. Contrary to predicted half-lives of TPTH, water depth did not greatly influence the percent contribution of each reaction mechanism (Figure B22 in Appendix B).

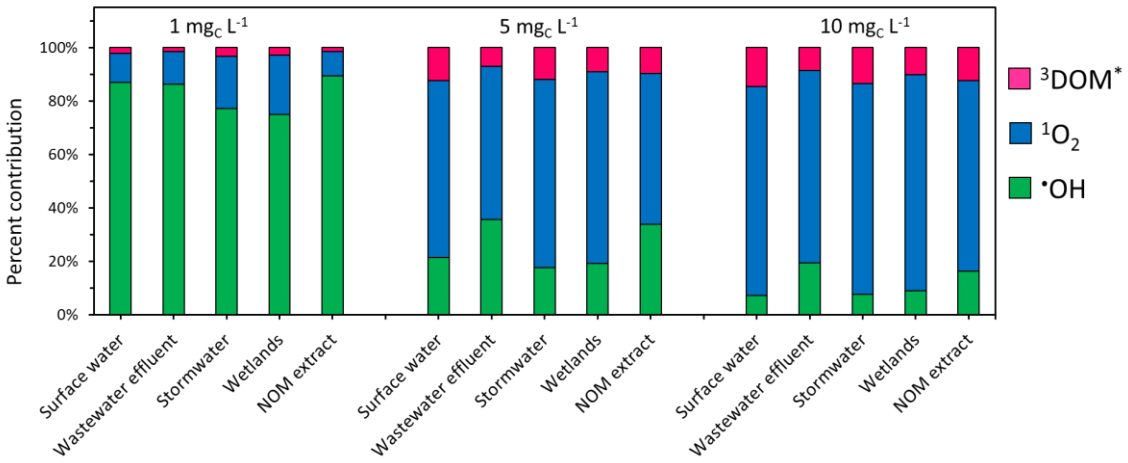

Figure 3.4. The percent contributions of $^1O_2$, $^\bullet OH$ and $^3DOM^*$ to TPTH photodegradation in different water sources with 1, 5, and 10 mg_C L^{-1} at 1 m water depth. These results were computed for solutions containing 10^{-6} M NO_2^-, 10^{-4} M NO_3^-, 10^{-3} M HCO_3^-, and 10^{-5} M CO_3^{2-}.

3.4 Conclusion

This study confirmed that (i) direct photolysis of triphenyltin chemicals is negligible and (ii) $^1O_2$, $^\bullet OH$, and $^3DOM^*$ all contribute to indirect photolysis of TPTH. The second-order rate constants for TPTH reaction with $^1O_2$ ($k''_{^1O_2,TPTH} = (3.9 \pm 0.5) \times 10^6$ M^{-1} s^{-1}) and $^3DOM^*$ ($k''_{^3AQ2S^*,TPTH} = (1.41 \pm 0.06) \times 10^6$ M^{-1} s^{-1}) were experimentally determined and reported for the first time. The calculated second-order rate constants suggested that all three reactive species were important to TPTH degradation in surface water. These rate constants, along with published quantum yields for $^1O_2$, $^\bullet OH$, and $^3DOM^*$ in 1308 different source waters, enabled APEX simulations to predict TPTH photodegradation kinetics. The model predictions highlighted the importance of $^\bullet OH$ in waters with 1-3 mg_C L^{-1} DOM and $^1O_2$ in waters with 3-15 mg_C L^{-1} DOM. The results of extensive APEX model simulations indicated that the 25-75th percentile range of TPTH half-lives was as follows: 126-262 SSD in surface water; 77-178 SSD in wastewater effluent; 55-126 SSD in stormwater; 51-78 SSD in wetlands; and, 106-202 SSD in NOM extracts. Based on the

median quantum yields for $^1O_2$, •OH, and $^3DOM^*$, the predicted median half-lives of TPTH at a 1 m water depth and 5 mg_C L^{-1} DOM followed the order: wetlands (60 SSD) < stormwater (74 SSD) < wastewater effluent (95 SSD) < NOM extracts (151 SSD) < surface water (157 SSD). The TPTH photodegradation kinetics in NOM extracts closely matched those in surface waters; however, faster TPTH degradation was observed for wetlands, wastewater effluent, and stormwater. Because, agricultural runoff, wastewater effluent, and antifouling paints from marine vessels are the main sources of triphenyltin contamination, the faster photodegradation kinetics in wetlands, wastewater effluent, and stormwater should facilitate TPTH attenuation and may inform opportunities to improve TPTH treatment in point sources.

3.5 Acknowledgments

We acknowledge funding from the National Science Foundation (CHE 1508090).

Chapter 4 Photochemical fate of triphenyltin pesticides in engineered treatment systems: Reaction kinetics, transformation products, and residual toxicity

Abstract

Triphenyltin hydroxide (TPTH) is an organotin fungicide on the Environmental Protection Agency contaminant candidate list that causes endocrine disruption and reproductive malformation in aquatic organisms. The objective of this study was to determine the photodegradation kinetics, identify the transformation products, and measure the residual toxicity of TPTH during treatment by the UV-254 and UV-H_2O_2 systems. The effective quantum yield of TPTH was 0.18 ± 0.02 mol Ein^{-1} for direct photolysis at 254 nm. The effects of solution pH (*e.g.*, 4-10), ionic strength (*e.g.*, 0.001-0.1 M), and photosensitizers (*e.g.*, hydrogen peroxide, dissolved organic matter) on TPTH photodegradation were explored to simulate various environmental conditions. Solution pH and ionic strength had a negligible influence on the measured rate constants. However, enhanced TPTH degradation was observed in the UV-H_2O_2 process due to reaction with hydroxyl radicals. The apparent second-order rate constant for TPTH reaction with hydroxyl radicals was $(7.81 \pm 0.37) \times 10^8$ M^{-1} s^{-1}. The primary phototransformation products were identified by liquid chromatography with tandem mass spectrometry and used to elucidate the reaction pathways of TPTH during direct photolysis and advanced oxidation. Hydroxylation of phenyl groups was identified as the main reaction pathway for advanced oxidation. The toxicological activity of TPTH and its phototransformation products was measured using bacterial growth inhibition assays

with *Staphylococcus* spp. (ATCC 14389). TPTH inhibited the growth of *Staphylococcus* spp. with an observed IC_{50} of approximately 400 µg L^{-1}. The antibacterial activity of the phototransformation products was assessed using the potency equivalents approach, and the results indicated that both direct photolysis and advanced oxidation generated antimicrobially-active products. Overall, the experimental results highlighted the need for advanced treatment of TPTH and careful consideration of the corresponding photoproducts to ensure removal of organotin toxicity in water and wastewater.

4.1 Introduction

Organotin chemicals, particularly tributyltin and triphenyltin, have been widely employed as heat stabilizers (polymer industry), fungicides and miticides (agriculture), and non-target biocides (marine paint) [118,119]. Triphenyltin compounds are broadly classified by the general formula, $(C_6H_5)_3Sn$-R, where 'R' represents an anion, such as acetate, chloride, or hydroxide [117]. However, triphenyltin acetate and triphenyltin chloride undergo rapid hydrolysis reactions in water to form triphenyltin hydroxide (TPTH), which accounts for more than 93% of triphenyltin species in seawater [165]. TPTH is a registered fungicide with the Environmental Protection Agency (EPA) for application on plants, such as rice, potatoes, and beets [43]. Until a recent ban [43], TPTH was also used as a biocide in antifouling paints for marine vessels and infrastructure to prevent the attachment and growth of algae and barnacles. Although inorganic tin is considered safe [166], organotin chemicals are toxic to humans and aquatic organisms [167]. Chronic toxicity can occur at ng L^{-1} concentrations in oysters (shell deformation) and marine gastropods (imposex) [40]. Due to its lethal, mutagenic, and carcinogenic effects, TPTH has been added to the US EPA

Contaminant Candidate List 4 [47,120]; however, the removal of triphenyltin chemicals in water and wastewater treatment processes is unknown and requires investigation to inform future treatment and remediation strategies.

Triphenyltin chemicals are considered to be among the most serious pollutants in worldwide water bodies [168]. The adverse effects of these compounds, along with their ubiquitous presence in surface water and sediment, have raised concerns about human exposure through (i) seafood products affected by bioaccumulation and biomagnification and (ii) contaminated drinking water sources. Hu *et al.* [122] reported average triphenyltin content in primary producers (*e.g.*, phytoplankton, zooplankton), invertebrates (*e.g.*, crab, shrimp, clam, whelk), and fish from Bohai Bay (China) to be 1.0, 3.7, and 6.5 ng Sn g^{-1} wet weight, respectively. In raw wastewater and reclaimed water from Mexico City (Mexico), the triphenyltin concentrations ranged from 3.7 to 9.3 ng Sn L^{-1}. Triphenyltin levels as high as 11.3 ng Sn L^{-1} were reported by Gao *et al.* [123] in the Three Gorges Reservoir (China), an important source of drinking and irrigation water for millions of people. These previous findings emphasize the need for advanced treatment processes for TPTH in both water and wastewater.

Compared to other mechanisms, such as hydrolysis and biodegradation, phototransformation was identified as the primary degradation pathway for TPTH in aquatic systems [117]. These findings suggest the effectiveness of photochemical processes for TPTH treatment in water and wastewater. However, previous studies only reported the apparent rate of triphenlytin degradation for specific water quality and operational

conditions [135,136,169], which prevents extrapolation of those findings to the design of photochemical water and wastewater treatment systems. Furthermore, drastic differences have been reported for the quantum yield of TPTH in deionized (DI) water, with values ranging from 1.1×10^{-6} mol Ein^{-1} for medium-pressure lamps with emission peaks at 185, 238, 248, 254, 265, 280, 297, 300, 313, and 366 nm [170] to 1.25 (± 0.26) mol Ein^{-1} for low-pressure lamps that emit at 254 nm [171]. The six order-of-magnitude difference in the quantum yield for direct photolysis has important implications for selection of photolytic (*e.g.*, UV-254) or photochemical (*e.g.*, UV-H_2O_2) treatment. In addition, the impacts of water quality parameters, namely solution pH, ionic strength, and dissolved organic matter (DOM) content, on TPTH phototransformation have not been evaluated. For these reasons, a detailed investigation of the photochemical reaction mechanisms and kinetics of TPTH is warranted to improve treatment process selection, design, and efficacy.

Based on data for other contaminants [63,172,173], the typical operating conditions for the UV-254 and UV-H_2O_2 processes are not expected to completely mineralize organotin chemicals. Due to the persistence and toxicity of organotin chemicals, the primary transformation products of TPTH and their corresponding toxicity need to be identified. Previous efforts suggested the sequential loss of phenyl groups from TPTH during photolysis to ultimately yield inorganic tin [135,136,170]. The formation of phenyltin dimers has also been postulated due to the poor recovery and lack of identifiable products during extended irradiation periods [135,170]; however, these products have not been analytically confirmed. UV-H_2O_2 advanced oxidation, which generates hydroxyl radicals ($^{\bullet}OH$), is expected to produce photoproducts that have not been previously reported for TPTH. For

this reason, the primary photoproducts and residual toxicity of TPTH require investigation to identify appropriate treatment goals that involve both TPTH concentration and toxicity.

This study aims to fill the aforementioned knowledge gaps on TPTH phototransformation in advanced water and wastewater treatment processes. In particular, the objectives were as follows: (1) calculate the fluence-based rate constant and quantum yield for direct photolysis of TPTH at 254 nm; (2) identify the influence of solution pH, ionic strength, and DOM content on the apparent rate of TPTH photodegradation; (3) measure the second-order rate constant for TPTH reaction with $^{\bullet}OH$; (4) determine the removal efficiency of TPTH by the UV-H_2O_2 advanced oxidation process; (5) characterize the primary photoproducts and reaction mechanisms for direct photolysis and advanced oxidation of TPTH; and, (6) establish the residual toxicity of TPTH photoproducts. This study reports critical kinetic parameters for treatment of triphenyltin compounds in UV-based treatment processes and informs the residual toxicity of TPTH photoproducts under typical operating settings for existing water and wastewater treatment processes.

4.2 Material and methods

4.2.1 Materials

TPTH (>98%) was purchased from Sigma-Aldrich (St. Louis, MO, USA), and high-performance liquid chromatography (HPLC) grade methanol was used to prepare a 1 g L^{-1} stock solution. Sodium phosphate monobasic monohydrate (>98%), sodium phosphate dibasic heptahydrate (>98%), sodium phosphate tribasic dodecahydrate (>98%), sodium

hydroxide (NaOH; 97%), hydrochloric acid (HCl; >98%), hydrogen peroxide (H_2O_2; 30%, v/v), *para*-chlorobenzoic acid (*p*CBA; 97%), glycerol (reagent grade), and tryptic soy broth were obtained from Fisher Scientific (Hampton, NH, USA). *Staphylococcus* spp. (#14389) was purchased from the American Type Culture Collection (ATCC; Manassas, VA, USA).

Suwannee River Natural Organic Matter (SRNOM) was secured from the International Humic Substances Society (Denver, CO, USA). A 400 mg L^{-1} stock solution was created by adding SRNOM to DI water, adjusting the pH to 10.0 with 0.1 M NaOH, and sonicating until the SRNOM was completely dissolved. Then, the pH of the SRNOM solution was adjusted to 7.0 with 1 M HCl, and the solution was passed through a 0.2-µm filter and stored at -20 °C [151]. A total organic carbon analyzer (Shimadzu TOC-L; Columbia, MD, USA) was employed to confirm the dissolved organic carbon concentration (87 mg_C L^{-1}) of the SRNOM working solution.

4.2.2 Analytical methods

The concentrations of TPTH and *p*CBA in experimental samples were determined by liquid chromatography with triple quadrupole tandem mass spectrometry (LC-MS/MS; Thermo UltiMate 3000 with Quantum Access Max; Waltham, MA, USA). Analytes were separated on a Waters Symmetry C18 column (2.1×150 mm, 3.5 µm) maintained at 40 °C. An isocratic mobile phase consisting of (i) 0.1% formic acid in LC-MS-grade water and (ii) LC-MS-grade methanol (40:60, v/v) was used for analysis; the flow rate was 200 µL min^{-1}. The electrospray ionization device was operated in positive mode for

TPTH and negative mode for *p*CBA. The following MS/MS settings were used for TPTH analysis: capillary temperature, 270 °C; spray voltage, 3000 V; sheath gas pressure, 40 (arbitrary units); auxiliary gas pressure, 15 (arbitrary units); and, collision gas (argon) pressure, 1.5 Torr. Except for the capillary temperature (250 °C) and spray voltage (2500 V), all MS/MS settings were identical for *p*CBA analysis. The measured ion transitions for TPTH and *p*CBA were 383.0 → 350.9 and 155.1 → 111.9, respectively.

4.2.3 Direct photolysis experiments

The direct photolysis kinetics of TPTH were measured in a Rayonet reactor equipped with eight bulbs emitting light at 254 nm. Using the ferrioxalate actinometer, the average incident photon flux was calculated to be 9.7 (± 0.4) × 10^{-9} Ein cm^{-2} s^{-1} [75]. The irradiated solutions (10 mL) initially contained 2.7 µM TPTH and 5 mM phosphate buffer in DI water. The 18-min irradiation time was selected to achieve a suitable extent of TPTH transformation for accurate calculation of rate constants. Dark controls were included to correct for other reactions, including hydrolysis. All experiments were carried out at room temperature (22 ± 1 °C). For each experiment, samples were collected at predetermined times, added to amber LC vials, and stored at -20 °C before analysis.

The apparent time ($k'_{\mathrm{d,254,app}}$, s^{-1}) and fluence ($k'_{\mathrm{p,254,app}}$, cm^2 mJ^{-1}) based, pseudo-first-order rate constants for direct photolysis of TPTH at 254 nm were calculated using Eq. 4.1 and Eq. 4.2, respectively.

$$k'_{\mathrm{d,254,app}} = -\left(\frac{1}{\mathrm{t}}\right)\ln\left(\frac{\mathrm{C_t}}{\mathrm{C_0}}\right)$$

(Eq. 4.1)

$$k'_{\mathrm{p,254,app}} = \frac{k'_{\mathrm{d,254,app}}}{\mathrm{I_0\ U_{254}}}$$

(Eq. 4.2)

The variables in Eq. 4.1-4.2 are defined as follows: t is the irradiation time (s); C_0 and C_t are the TPTH concentrations (µM) at time 0 and t, respectively; I_0 is the net photon flux (Ein cm^{-2} s^{-1}); and, U_{254} is the molar photon energy of 254-nm light (4.72×10^8 mJ Ein^{-1}).

The absorbance spectra of solutions containing 27 µM TPTH and 5 mM phosphate buffer were determined at pH 4.0 ± 0.1, 7.0 ± 0.1, and 10.0 ± 0.1 for wavelengths (λ) of 200-300 nm. These measurements were recorded by UV-visible absorbance spectrophotometry (Thermo Evolution 600; Waltham, MA, USA) in a quartz cuvette with 10-cm pathlength (ℓ, cm). The absorbance data were divided by the TPTH concentration and pathlength to calculate apparent molar absorption coefficients ($\varepsilon_{\lambda,\mathrm{app}}$, M^{-1} cm^{-1}). With Eq. 4.3, the time-based, pseudo-first-order rate constants and molar absorption coefficients were used to evaluate the apparent quantum yield ($\phi_{254,\mathrm{app}}$, mol Ein^{-1}) for TPTH at 254 nm [53]. Note, the I'_0 parameter in Eq. 4.3 is the average photon intensity per volume (Ein L^{-1} s^{-1}).

$$\phi_{254,\mathrm{app}} = \frac{k'_{\mathrm{d,254,app}}}{2.303\ \ell\ \varepsilon_{254,\mathrm{app}}\ \mathrm{I'_0}}$$

(Eq. 4.3)

The impacts of water quality parameters, including solution pH, ionic strength, and DOM content, on the direct photolysis kinetics of TPTH were also investigated in the Rayonet reactor. The initial TPTH concentration was 2.7 µM for all experiments, and the other conditions were varied as indicated below. Solution pH was adjusted to environmentally relevant values (*i.e.*, pH 4, 7, 10) using 5 mM phosphate buffer. Photolysis experiments were conducted at pH 7 with 1, 10, and 100 mM NaCl to assess ionic strength effects. To evaluate the impact of DOM on TPTH degradation, 10 $mg_C\ L^{-1}$ of SRNOM was added to the experimental solutions, and the solution pH was adjusted to 7.0 ± 0.2 with 5 mM phosphate buffer.

4.2.4 UV-H_2O_2 experiments

TPTH degradation in the UV-H_2O_2 process was investigated using solutions that initially contained 2.7 µM TPTH, 0.27 µM – 16.2 mM H_2O_2, 75 µM *p*CBA, and 5 mM phosphate buffer (pH 7.0 ± 0.2). Competition kinetics were employed to determine the second-order rate constant for TPTH reaction with •OH ($k''_{\bullet OH,TPTH}$) in accordance with previous protocols [53]. The fractional contributions of direct photolysis (f_d) and •OH ($f_{\bullet OH}$) to the overall TPTH degradation were calculated by Eq. 4.4a and 4.4b, respectively.

$$f_d = \frac{S\, k'_{p,254,app}}{S\, k'_{p,254,app} + k''_{\bullet OH,TPTH} \int_0^t [\bullet OH]\, dt} \qquad \text{(Eq. 4.4a)}$$

$$f_{\cdot OH} = 1 - f_d = \frac{k''_{\cdot OH,TPTH} \int_0^t [\cdot OH]\, dt}{S\, k'_{p,254,app} + k''_{\cdot OH,TPTH} \int_0^t [\cdot OH]\, dt}$$

(Eq. 4.4b)

In Eq. 4.4, S is the screening factor, which accounts for inner-filter effects, and $\int_0^t [\cdot OH]\, dt$ is the hydroxyl radical exposure (M s). To balance TPTH degradation by direct photolysis and ·OH, 0.1, 1, 10, 100, 1000, 3000, and 6000 mol H_2O_2/mol TPTH were initially examined to achieve at least 50% TPTH degradation by ·OH and at least 80% overall TPTH degradation within 12 min. The optimal condition for calculation of $k''_{\cdot OH,TPTH}$ was determined to be 6000 mol H_2O_2/mol TPTH.

4.2.5 Analysis of phototransformation products

A relatively high initial TPTH concentration (54 µM) was used to ensure the detection of transformation products formed during UV-254 and UV-H_2O_2 treatment. Characterization of photodegradation products was carried out using LC-MS and LC-MS/MS in positive electrospray ionization mode. TPTH and its photoproducts were separated on a Waters Symmetry C18 column (2.1×150 mm, 3.5 µm) at a flow rate of 200 µL min^{-1}. The mobile phase included 0.1% formic acid in (A) LC-MS grade water and (B) LC-MS grade methanol with the following gradient program: 0-4 min, 10% B; 4-10 min, ramp to 60% B; 10-30 min, 60% B; 30-36 min, ramp to 10% B; and, 36-40 min, 10% B. The column temperature was 40 °C, and the sample injection volume was 50 µL. The mass spectra acquisition included (1) full scan MS measurements of *m/z* 100-500 to identify peaks corresponding to TPTH phototransformation products and (2) data-

dependent MS/MS analysis in collision-induced dissociation mode to fragment the most abundant ion in each full scan event. To ensure comprehensive evaluation, fragmentation was conducted with collision energies of 10, 20, and 30 V. The exact mass and fragmentation patterns were recorded and used to propose the chemical formulae and structures of transformation products. Due to the lack of chemical standards for the proposed products, MS/MS peak areas were used to monitor formation and degradation trends during UV-254 and UV-H_2O_2 treatment.

4.2.6 Residual toxicity analysis

The residual toxicity of TPTH and its transformation products was analyzed in samples that had undergone treatment by the UV-254 and UV-H_2O_2 systems. In particular, 90-mL solutions were prepared with 27 µM TPTH, 0 mM H_2O_2 (for direct photolysis at 254 nm) or 10 mM H_2O_2 (for advanced oxidation with UV-H_2O_2), and 5 mM phosphate buffer (pH 7.0 ± 0.2). Then, 10-mL aliquots were added to eight quartz tubes (for each experiment) before irradiation at 254 nm in the Rayonet reactor. Each tube was removed from the reactor at a predetermined time. A small volume (100 µL) of each sample was used to measure the TPTH concentration, and the rest was employed for analysis of residual toxicity via a growth inhibition assay with *Staphylococcus* spp. (ATCC 14389). The remaining 10 mL of the original solution was used to establish the half-maximal inhibitory concentration (IC_{50}) of TPTH against *Staphylococcus* spp.

The freeze-dried *Staphylococcus* spp. from ATCC was transferred into 100 mL of tryptic soy broth and cultured at 37 °C and 160 rpm. Once the optical density at 600 nm (OD_{600},

measured per cm) reached 2.0, the culture was mixed with autoclaved glycerol (1:1, v/v), and 1-mL aliquots were transferred into 2-mL cryovials for storage at -80 °C. One cryovial was used to generate the inoculum for each assay. After thawing at room temperature, 0.5 mL from the cryovial was added to 25 mL of tryptic soy broth. The mixture was cultured at 37 °C and 160 rpm until OD_{600} reached 3.0, which typically occurred after 16-24 h. The specific OD_{600} was recorded, and an inoculum was generated with an OD_{600} of 0.1 (equivalent to ~10^6 CFU mL^{-1}) though dilution with tryptic soy broth.

The residual toxicity of untreated and irradiated TPTH solutions was measured as growth inhibition of *Staphylococcus* spp. in 96-well microplates. Two samples from the untreated or treated solutions were analyzed in triplicate per microplate, with each sample undergoing 11 serial dilutions (*i.e.*, 12 total subsamples). The subsamples were placed in wells A1-C12 (first sample) and F1-H12 (second sample). First, 250 μL of the experimental samples were deposited into wells A1-C1 and F1-H1, and 100 μL of tryptic soy broth was added to wells A2-C12, D1-E12, and F2-H12. Then, 150 μL of the experimental samples were transferred from wells A1-C1 to A2-C2 to achieve a dilution factor of 1.67. The mixtures were aspirated at least three times, and then 150 μL from wells A2-C2 was transferred into A3-C3. The dilution scheme continued through to wells A12-C12, which were aspirated and then 150 μL was wasted. Wells A1-C12 and F1-H12, which contained 100 μL of serially diluted experimental samples, were then supplemented with 100 μL of the *Staphylococcus* spp. inoculum. Positive controls were generated in wells D1-E6 by adding 100 μL of tryptic soy broth and 100 μL of inoculum.

Negative controls, consisting of 200 μL of tryptic soy broth, were placed in wells D7-E12.

During incubation at 37 °C and 160 rpm, the microplates were covered with lids to minimize evaporation. After 16-20 h, microplates were withdrawn from the incubator and the lids were removed. The microplates were placed in a microplate reader (BioTek Eon; Winooski, Vermont, USA) and underwent orbital shaking at 425 rpm for 30 s before measurement of OD_{600}. The shaking and analysis procedures were repeated three times to ensure precision. The mean of the three OD_{600} measurements was used to calculate the growth inhibition for each subsample (Eq. 4.5).

$$\mathrm{I}\ (\%) = \left(\frac{\mathrm{OD}_{600,\mathrm{pos}} - \mathrm{OD}_{600,ss}}{\mathrm{OD}_{600,\mathrm{pos}} - \mathrm{OD}_{600,\mathrm{neg}}}\right) 100\% \qquad \text{(Eq. 4.5)}$$

In Eq. 4.5, I is growth inhibition of *Staphylococcus* spp., and $\mathrm{OD}_{600,\mathrm{pos}}$, $\mathrm{OD}_{600,\mathrm{neg}}$, and $\mathrm{OD}_{600,ss}$ are the OD_{600} of the positive control, negative control, and subsample, respectively.

Using OriginPro 9.3 (Northampton, MA, USA), the growth inhibition data were fit to the Hill equation (Eq. 4.6). Separate Hill models were fit to the growth inhibition data from (i) untreated TPTH solutions and (ii) each serially diluted sample from the UV-254 and UV-H_2O_2 experiments. The IC_{50} values and corresponding 95% confidence intervals were recorded for each model.

$$I\ (\%) = I_{min} + \frac{I_{max} - I_{min}}{1 + \left(\frac{IC_{50}}{C}\right)^{H}}$$

(Eq. 4.6)

In Eq. 4.6, I_{min} is the minimum growth inhibition, I_{max} is the maximum growth inhibition, C is the molar concentration of TPTH, and H is the Hill slope.

The residual toxicity of samples that underwent UV-254 or UV-H_2O_2 treatment was converted into potency equivalents (PEQ) using Eq. 4.7.

$$PEQ = \frac{IC_{50}^{untreated}}{IC_{50}^{treated}}$$

(Eq. 4.7)

In Eq. 4.7, $IC_{50}^{untreated}$ is the IC_{50} value for TPTH standards, and $IC_{50}^{treated}$ is the IC_{50} value for experimental samples that contained TPTH and transformation products.

4.2.7 Statistical Analysis

Linear regressions and statistical analysis of experimental data were performed using Microsoft Excel 365 and Origin Pro 9.3. Analysis of Covariance (ANCOVA) tests were conducted to determine the significance of differences in the calculated rate constants for the investigated solution conditions. If the *p*-value was less than 0.05, then the difference was considered significant.

4.3 Results and Discussion

4.3.1 Direct photolysis of TPTH at 254 nm

The apparent molar absorption coefficients of TPTH at pH 4, 7, and 10 are reported for 200-300 nm in Figure B16 of Appendix C. The results indicated that solution pH did not affect the apparent molar absorbance of TPTH, which has a pK_a value of 8.49; therefore, the neutral and anionic TPTH species exhibited similar absorbance profiles. At 254 nm, the measured molar absorption coefficient of TPTH was $(8.14 \pm 0.08) \times 10^2$ M^{-1} cm^{-1}, highlighting the potential for TPTH transformation by the UV-254 process.

The pseudo-first-order rate constants and quantum yield for direct photolysis of TPTH at 254 nm were calculated according to Eq. 4.1-4.3 using the data shown in Figure C1 of Appendix C; the measured values are reported in Table 4-1. The quantum yield determined in this study, namely 0.18 ± 0.02 mol Ein^{-1}, was five orders of magnitude higher than that reported by Navio *et al.* (1.1×10^{-6} mol Ein^{-1}) for medium-pressure lamps with emission peaks at 185-366 nm [170] and one order of magnitude lower than the quantum yield published by Palm *et al.* (1.25 ± 0.26 mol Ein^{-1}) for a 254-nm light source [171]. In a separate validation experiment using polychromatic light, Palm *et al.* measured a quantum yield of 0.3 mol Ein^{-1}, which is similar to the value reported in Table 4-1. The two previous studies [170,171] calculated time-based rate constants for TPTH photodegradation, but the corresponding fluence-based rate constants were not determined and cannot be estimated, because the photon flux in their photoreactors was not provided. The large discrepancy in the literature-reported quantum yields of TPTH

cannot be explained; however, the direct photolysis parameters reported in Table 4-1 are preferred due to (i) the lower uncertainty on the quantum yield (*i.e.*, 8.9% in this study, 20.8% in Palm *et al.* [171], not reported in Navio *et al.* [170]) and (ii) the high reproducibility observed during investigation of water quality impacts on direct photolysis of TPTH.

Table 4-1. Photochemical properties for direct photolysis of TPTH at 254 nm and pH 7.

Property	Parameter	Value
Molar absorption coefficient	$\varepsilon_{254,app}$	$(8.14 \pm 0.08) \times 10^{2}$ M^{-1} cm^{-1}
Time-based, pseudo-first-order rate constant	$k'_{d,254,app}$	$(2.34 \pm 0.16) \times 10^{-3}$ s^{-1}
Fluence-based, pseudo-first-order rate constant	$k'_{p,254,app}$	$(5.18 \pm 0.25) \times 10^{-4}$ cm^{2} mJ^{-1}
Quantum yield	$\Phi_{254,app}$	0.18 ± 0.02 mol Ein^{-1}

The effects of water quality parameters were explored to advance understanding of TPTH photodegradation kinetics in real water and wastewater systems. Figure 4.1 shows the observed fluence-based, pseudo-first-order rate constants for TPTH photodegradation at 254 nm as a function of solution pH, ionic strength, and DOM content. As with the molar absorption coefficients, the observed rate constants for TPTH photodegradation at pH 4, 7, and 10 were similar (p = 0.12, ANCOVA). These results indicate that the neutral and anionic TPTH species exhibit similar photochemical reactivity at 254 nm. The average fluence-based rate constant from the variable pH experiments was $(5.18 \pm 0.17) \times 10^{-4}$ cm^{2} mJ^{-1}. Similar to TPTH, the fluazaindolizine pesticide exists as both neutral and anionic species in water (pK_a = 5.6), but the speciation profile did not affect photodegradation kinetics [174]. This result supports the lack of influence from solution pH on the photochemical reactivity of TPTH.

Previous literature indicated that ionic strength can enhance the photodegradation of organic contaminants by increasing the steady-state concentrations of their excited triplet states, either by reducing the triplet quenching reaction rates or by enhancing the intersystem crossing of singlet excited species to the triplet excited states [175,176]. As shown in Figure 4.1, the observed rate constants for TPTH photodegradation at 254 nm did not significantly change for the 1-, 10-, and 100-mM ionic strength conditions (p = 0.07, ANCOVA), suggesting a negligible influence of ionic strength on the production or scavenging of excited triplet TPTH species. The average fluence-based rate constant for TPTH calculated for the variable ionic strength experiments was $(5.04 \pm 0.23) \times 10^{-4}$ cm^2 mJ^{-1}, which overlaps with the rate constants recorded for the variable pH conditions.

Unlike solution pH and ionic strength, the addition of 10 mg_C L^{-1} DOM did inhibit TPTH degradation. However, after applying screening corrections to account for inner-filter effects caused by the DOM content, no significant differences (p = 0.06, ANCOVA) were observed between the apparent rate constants for TPTH photodegradation in solutions with variable pH, ionic strength, and DOM. The average screening-corrected fluence-based rate constant for solutions containing DOM was $(4.98 \pm 0.30) \times 10^{-4}$ cm^2 mJ^{-1}, similar to those recorded for the variable pH and ionic strength experiments as highlighted in Figure 4.1. These findings were reinforced by separate equilibrium experiments (not shown) that confirmed the negligible interaction of TPTH and DOM in solutions containing 10 mg_C L^{-1} DOM, 5 mM phosphate buffer (to maintain pH at 4-10),

and 0.027-54 µM TPTH. Overall, the results confirmed that the DOM influence on TPTH removal efficiency at 254 nm is limited to light screening.

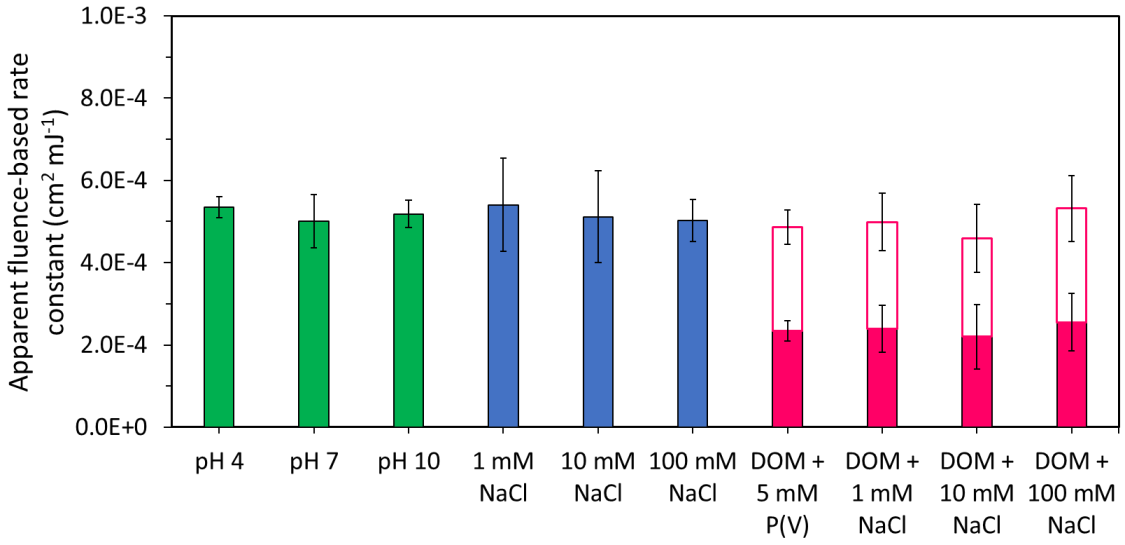

Figure 4.1. Observed rate constants for TPTH degradation by direct photolysis at 254 nm. The green columns indicate the influence of solution pH, which was adjusted with 5 mM phosphate buffer, on TPTH degradation. The blue columns represent TPTH degradation kinetics with 1, 10, and 100 mM ionic strength (as NaCl). The red columns show the combined effects of DOM (10 mg_C L^{-1}) and ionic strength (as 5 mM phosphate buffer or 1, 10, and 100 mM NaCl) on TPTH degradation. The hollow red columns are the screening-corrected rate constants for TPTH in the presence of DOM. The initial TPTH concentration was 2.7 µM, and the solution pH was adjusted to 7.0 ± 0.2 for all conditions, except those in which pH was varied. Error bars correspond to 95% confidence intervals on the mean rate constants from duplicate time-series experiments (n = 7 × 2 = 14).

Based on the photochemical properties reported in Table 4-1, 2-10% TPTH degradation is expected for a typical UV-254 process operating with a fluence of 40-200 mJ cm^{-2} [9]. To achieve greater than 90% TPTH transformation, the fluence would have to exceed 4500 mJ cm^{-2}, which is not economical. These results demonstrate the need for advanced processes to effectively treat TPTH in water and wastewater.

4.3.2 TPTH transformation in the UV-H_2O_2 advanced oxidation process

In the UV-H_2O_2 system, TPTH degradation involves direct photolysis at 254 nm and reaction with hydroxyl radicals [172]. The hydroxyl radical contribution to the degradation of 2.7 µM TPTH was minimal at H_2O_2 concentrations of 0.27-270 µM (Figure C1 in Appendix C). The time-based, pseudo-first-order rate constants for these conditions were 2.0-2.6 × 10^{-3} s^{-1}, comparable to the direct photolysis rate constant reported in Table 4-1, (2.34 ± 0.16) × 10^{-3} s^{-1}. Therefore, higher H_2O_2 doses were needed to evaluate the second-order rate constant for TPTH reaction with hydroxyl radicals. With 16 mM H_2O_2 (*i.e.*, ~6000 mol H_2O_2/mol TPTH), 99.5% of the incident photon flux was absorbed by H_2O_2, reducing the rate of direct photolysis and enabling greater production of hydroxyl radicals. For this condition, TPTH degradation was enhanced by 38% at pH 7, because the observed pseudo-first-order rate constant increased from (2.34 ± 0.16) × 10^{-3} s^{-1} for direct photolysis at 254 nm to (3.22 ± 0.20) × 10^{-3} s^{-1} for UV-H_2O_2 treatment (Figure 4.2a).

As shown in Figure 4.2b, competition kinetics with *p*CBA enabled the determination of the second-order rate constant for TPTH reaction with hydroxyl radicals [53]. At pH 7 and an initial H_2O_2 concentration of 16 mM, the second-order rate constant was calculated to be (7.81 ± 0.37) × 10^{8} M^{-1} s^{-1}. For the conditions reported in Figure 4.2b, the contributions of direct photolysis (f_d) and hydroxyl radicals ($f_{\cdot OH}$) to the overall TPTH degradation kinetics were 43% and 57%, respectively. The reported fractional contributions met the requirements outlined in Section 2.4. The second-order rate constant obtained in this study was approximately an order of magnitude lower than the

value, (9.4 ± 3) × 10^9 M^{-1} s^{-1}, reported by Palm *et al.* [171]. To measure TPTH concentrations, Palm *et al.* [171] employed HPLC with UV absorbance at 220 nm. At low wavelengths (< 230 nm), solvent interferences can affect analytical accuracy by HPLC-UV [177,178]; furthermore, UV absorbance is a non-selective detection method that is subject to interferences from transformation products. These phenomena may explain the high error on the Palm *et al.* rate constant (32%) and possibly account for the difference in magnitude. For typical fluence conditions employed during advanced oxidation (*i.e.*, 540-2000 mJ cm^{-2} [9]) and 6000 mol H_2O_2/mol TPTH, the TPTH degradation efficiency ranged from 50 to 92%.

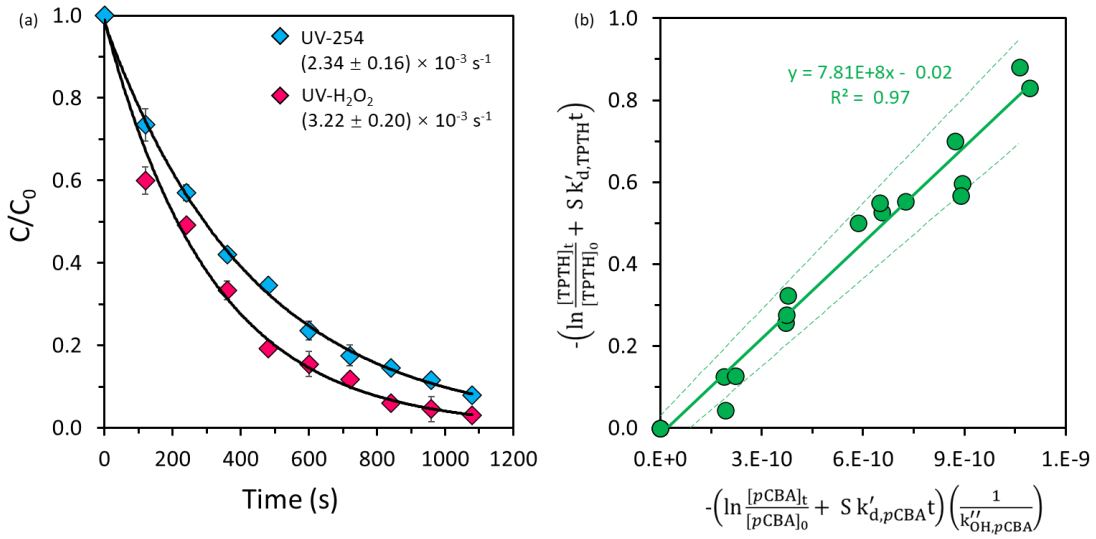

Figure 4.2. (a) TPTH degradation profiles for the UV-254 and UV-H_2O_2 treatment processes and (b) determination of the second-order rate constant for TPTH reaction with hydroxyl radicals. In (a), the initial TPTH and H_2O_2 concentrations were 2.7 µM and 16 mM, respectively, and the solution pH was 7.0 ± 0.1. The plotted symbols represent the mean of triplicate experiments, and the error bars are standard deviation. The solid lines represent are the exponential fit to the presented data sets. The observed rate constants for TPTH at UV-254 and UV-H_2O_2 were (2.34 ± 0.16) × 10^{-3} s^{-1} and (3.22 ± 0.20) × 10^{-3} s^{-1}, respectively. Competition kinetics presented in (b) were conducted with solutions containing of 2.7 µM TPTH, 5 mM phosphate buffer (to maintain pH at 7.0), 16 mM H_2O_2, and 75 µM *p*CBA. The solid line is the mean slope of the aggregate data set (from triplicate experiments, n = 18), and the dashed lines represent the lower and upper 95% confidence bands.

4.3.3 Identification of primary TPTH photoproducts

The *m/z* values of TPTH and its phototransformation products were initially identified by LC-MS. The fragmentation patterns of TPTH and transformation products were then assessed by MS/MS to provide additional information and confirm chemical structures. The MS spectrum and MS/MS fragmentation pattern of TPTH are provided in Figure C2 of Appendix C. From Figure C3a in Appendix C, electrospray ionization of TPTH generated two main *m/z* peaks at 350.39 and 382.93. The *m/z* of 350.39 corresponded to the loss of the hydroxide group during ionization ($[C_{18}H_{15}Sn\text{-}OH]^+$) [179], as confirmed by the MS/MS fragments at *m/z* 196.74, and 119.88. The *m/z* of 382.93 was a TPTH-methanol adduct, namely $[C_{18}H_{15}Sn+MeOH]^+$, with MS/MS fragments at *m/z* 350.39, 272.06, 196.74, and 119.88 (Figure C2b in Appendix C). The formation of methanol adducts during electrospray ionization has been previously attributed to the polar bond between the tin atom and hydroxide group [3]. Recall, the stock solution of TPTH was prepared in methanol, and the LC mobile phase contained methanol and water. For this reason, most of the product identification involved analysis of methanol adducts. Organotins also exhibit distinct *m/z* clusters due to the presence of tin isotopes [4], which were used to confirm phototransformation products that retained the tin atom.

Preliminary photoproduct identification was conducted by comparing the LC-MS chromatograms of UV-254 or UV-H_2O_2 treated samples to the initial solution. The presence of unique LC-MS peaks in the treated samples indicated transformation products. Using this strategy, no TPTH transformation products were identified for UV-

254 treatment. The absence of identifiable products for direct photolysis of TPTH was attributed to low yields that resulted in concentrations below the instrumental detection limit. Figure C3 in Appendix C shows LC-MS chromatograms for a solution that initially contained 54 μM TPTH before and after 12 min of treatment by the UV-H_2O_2 system. The LC-MS chromatogram for the treated sample exhibited three peaks that were not present in the initial solution. All three new peaks exhibited MS/MS fragments consisting of tin isomer clusters and *m/z* 120.02 (*i.e.*, tin cation). The retention times, *m/z* of parent ions, and fragmentation patterns for TPTH and the identified phototransformation products are summarized in Table 4-2.

Table 4-2. MS and MS/MS information used to identify TPTH phototransformation products formed during the UV-H_2O_2 process. Measured fragment ion of *m/z* 120.02 corresponds to tin cation.

Compound	Retention time (min)	Measured parent ion (m/z)	Ion designation	Measured fragment ion (m/z)	Proposed structure
TPTH	16.00	382.66	$[C_{18}H_{15}Sn+MeOH]^+$	350.39 196.95 120.02	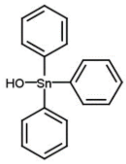
P1	15.04	398.69	$[C_{18}H_{14}Sn+MeOH+OH]^+$	366.70 196.74 120.02	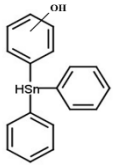
P2	15.04	412.92	$[C_{18}H_{13}Sn+MeOH+(OH)_2]^+$	366.70 196.74 120.02	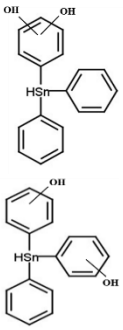
P3	15.52	398.69	$[C_{18}H_{14}Sn+MeOH+OH]^+$	288.79 212.84 153.20 120.02	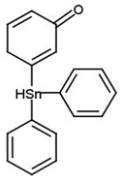
P4	17.34	380.63	$[C_{18}H_{14}Sn+MeOH+OH-H_2O]^+$	350.39 196.74 165.10 120.02	none proposed

Overall, four main photoproducts were confirmed as organotins using the *m/z* 120.02 fragment ion, which corresponds to $[Sn]^+$. The phototransformation products P1 (*m/z* 398.64) and P2 (*m/z* 412.98) were identified as $[C_{18}H_{14}Sn+MeOH+OH]^+$ and $[C_{18}H_{13}Sn+MeOH+(OH)_2]^+$, respectively. Note, the mass difference (2 Da) for

assignment of P2 stems from tin isotope distribution during electrospray ionization [3,179]. P1 and P2 formed through hydroxyl radical attack at the phenyl groups (Table 4-2) to form mono- and di-hydroxylated products, respectively. Previous research has shown that dihydroxylation can occur at the same aromatic ring or different rings during UV-H_2O_2 treatment [180], hence two structures were proposed for P2. The retention times of P1 and P2 (15.04 min) were earlier than TPTH (16.00 min), as expected for more polar compounds. The MS/MS fragmentation spectra of both photoproducts included isotope clusters at *m/z* 366.70, 196.7, and 120.0 (Figure C4 in Appendix C), reinforcing the retention of organotin moieties. These fragments stem from loss of the methanol adduct to form $[C_{18}H_{15}Sn+OH]^+$, cleavage of two Sn-C bonds to form $[C_6H_6Sn+H]^+$, and loss of all phenyl groups to form $[Sn]^+$, respectively. Photoproduct P3 (*m/z* 398.69) had the same mass as P1, suggesting that the observed ion was $[C_{18}H_{14}Sn+MeOH+OH]^+$. However, the retention time (15.52 min) and fragmentation pattern (*m/z* 288.79, 153.20) of P3 were different than those of P1, confirming that P3 was a unique photoproduct with a different chemical structure than P1. In this case, P1 was expected to undergo keto-enol tautomerization to form P3, with the formula and proposed structure shown in Table 4-2. Based on the observed *m/z* values, P4 is likely a dehydration product of P1 (*i.e.*, $[C_{18}H_{14}Sn+MeOH+OH-H_2O]^+$), but no chemical structure was proposed due to the high degree of overlap in MS/MS fragments (Figure C6 in Appendix C).

This information was used to reanalyze the experimental samples by LC-MS/MS in selective reaction monitoring mode to obtain chromatograms with better sensitivity (Figure C6 in Appendix C) and evaluate photoproduct trends with treatment (Figure 4.3).

The photoproducts exhibited similar formation and degradation patterns, with apparent generation for the first 12 min (fluence, 3300 mJ cm^{-2}) of UV-H_2O_2 treatment, followed by consistent degradation over the next 30 min (fluence, 8242 mJ cm^{-2}). The highest photoproduct peak areas coincided with 44% transformation of TPTH. Unfortunately, photoproduct concentrations could not be determined due to the absence of commercially available standards, but these results did confirm production of tin-containing transformation products during UV-H_2O_2 treatment. The contribution of these organotin transformation products to the residual toxicity of treated TPTH solutions was further investigated for the UV-254 and UV-H_2O_2 treatment processes.

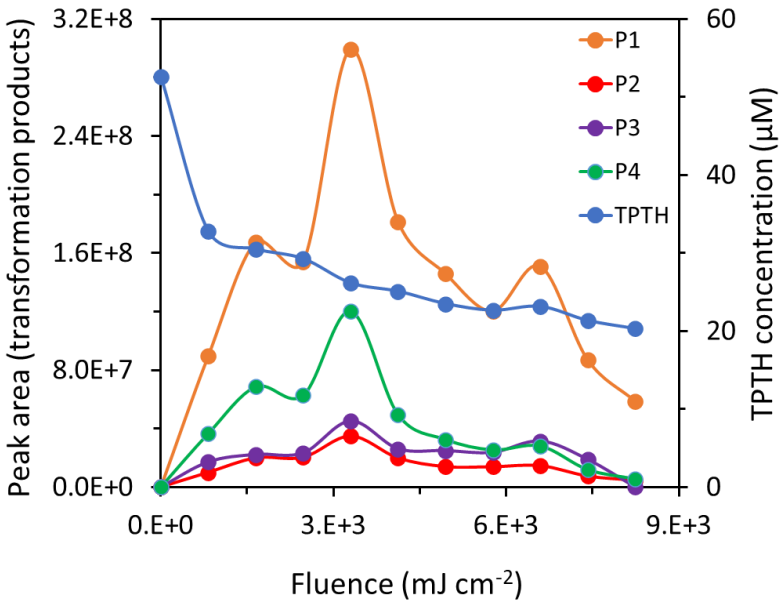

Figure 4.3. Concentration profiles of TPTH and the primary phototransformation products (as peak areas) during UV-H_2O_2 treatment. The initial solution contained 54 µM TPTH and 16 mM H_2O_2.

4.3.4 Residual toxicity of TPTH and photoproducts

Transformation product investigation revealed that (i) mineralization of TPTH cannot be expected during UV-based treatment and (ii) the primary photoproducts retained the C-Sn bond. These products may also retain the toxicity of TPTH and, therefore, raise environmental concerns. To evaluate the residual toxicity, growth inhibition assays with *Staphylococcus* spp. were performed on treated TPTH samples and compared to the untreated solutions. The inhibition profiles of the untreated TPTH solutions with and without H_2O_2 are presented in Figure 4.4, and the corresponding IC_{50} values were 0.45 ± 0.03 mg L^{-1} and 0.25 ± 0.02 mg L^{-1}, respectively. The lower IC_{50} obtained for the TPTH + H_2O_2 solution was likely due to inhibitory effects from H_2O_2. The concentration of H_2O_2 was assumed to be relatively constant in irradiated solutions and PEQ was calculated based on the initial concentration.

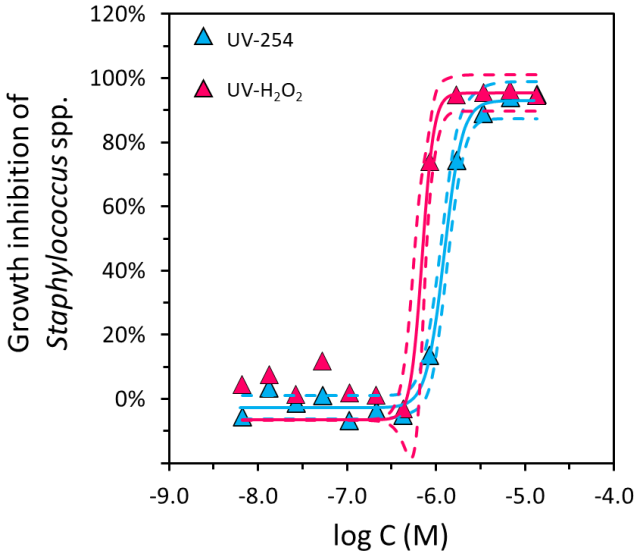

Figure 4.4. *Staphylococcus* spp. growth inhibition profiles for solutions containing TPTH (only) and TPTH with 10 mM H_2O_2 as representative samples of the untreated UV-254 and UV-H_2O_2 solutions. The solid curves are the best-fit Hill models, and the dashed curves are the 95% confidence bands. The symbols are the mean growth inhibition from triplicate measurements.

Growth inhibition profiles were also generated for each sample collected from the TPTH solutions treated by the UV-254 and UV-H_2O_2 systems. The IC_{50} value for each individual sample was used, along with the corresponding parameters for the untreated solutions, to calculate PEQs with Eq. 4.7. The PEQ data were plotted against the normalized TPTH concentration in each sample to evaluate the residual toxicity of the photoproducts. If TPTH was the only toxic compound in the sample, the PEQ data would decrease along the 1:1 line in Figure 4.5. Importantly, all of the measured PEQ values were above the 1:1 line, suggesting that the photoproducts from the UV-254 and UV-H_2O_2 processes retained antimicrobial activity. For UV-254 treatment, the maximum PEQ (3.3) was recorded at a fluence of 275 mJ cm^{-2}, which coincided with 35% TPTH degradation. Because the PEQ data exceeded 1.0, the phototransformation products were more potent than TPTH. Furthermore, the PEQ values remained above 1.0 for fluence up to approximately 1370 mJ cm^{-2}, indicating that typical UV treatment processes actually increase the toxicity associated with TPTH. Similar results were obtained for the UV-H_2O_2 process, but the maximum PEQ value (2.4) was lower and occurred at a lower fluence (140 mJ cm^{-2}) and extent of TPTH degradation (15%). Nevertheless, the PEQ values exceeded 1.0 until a fluence of approximately 825 mJ cm^{-2}. Given the noted differences in TPTH photoproducts for the UV-254 and UV-H_2O_2 systems, along with the competitive reaction kinetics of direct photolysis and $^{\bullet}OH$, the direct photolysis photoproducts are expected to be more toxic than the hydroxylation and dehydration products identified in Table 4-2.

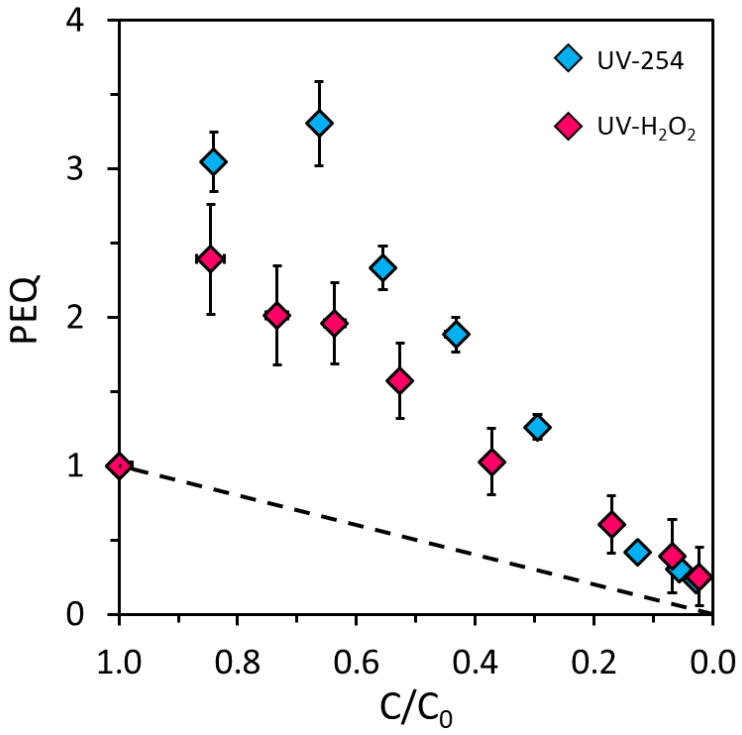

Figure 4.5. Antimicrobial activity (as PEQs) of UV-254 and UV-H_2O_2 treated solutions as a function of the residual TPTH concentration (C/C_0). The symbols are the mean PEQs from triplicate measurements, and the error bars in both directions represent 95% confidence intervals. The dashed 1:1 line indicates the scenario wherein TPTH is the only source of toxicity. Data points above the 1:1 line revealed that phototransformation products exert antimicrobial activity.

4.4. Conclusion

This study evaluated the photodegradation kinetics and removal efficiencies of TPTH in the UV-254 and UV-H_2O_2 systems. For the calculated fluence-based, pseudo-first-order rate constant, $(5.18 \pm 0.25) \times 10^{-4}$ cm^2 mJ^{-1}, only 2-10% TPTH degradation is expected in the typical UV processes currently used for drinking water and wastewater treatment. The removal efficiency of TPTH increased to 50-92% with the addition of 16 mM H_2O_2 due to generation of $^{\bullet}OH$ by the UV-H_2O_2 system. Due to the relatively slow phototransformation kinetics, complete mineralization of TPTH is not expected for the typical operating conditions employed with the UV-254 and UV-H_2O_2 processes. The

isomer clusters and unique fragmentation patterns of organotins were used to identify TPTH phototransformation products. Interestingly, no photoproducts were recorded for UV-254 treatment, but four hydroxylation and dehydration products of TPTH were identified in the UV-H_2O_2 system. Growth inhibition assays with *Staphylococcus* spp. demonstrated that photoproducts were more potent than TPTH and indicated that overall toxicity will increase for typical fluence conditions. The photoproducts formed by direct photolysis were apparently more toxic than those produced during UV-H_2O_2 treatment. Overall, these results indicate (i) the change in TPTH concentration is not a sufficient metric for describing the treatment efficacy of the UV-254 and UV-H_2O_2 processes and (ii) phase-change processes (*e.g.*, adsorption) may be more appropriate for TPTH to prevent generation of toxic photoproducts.

4.5 Acknowledgements

We acknowledge funding from the National Science Foundation (CHE 1508090).

Chapter 5 Conclusions

5.1 Overview

The objective of this dissertation was to advance understanding of the photochemical fate of organometallics in the aquatic environment. This goal was accomplished by examining the applicability of proven experimental approaches, measuring key photochemical reaction kinetics parameters, modeling photodegradation half-lives, identifying primary transformation products, and determining residual toxicity for organoselenium and organotin chemicals in natural and engineered systems. In addition, the dissertation involved innovative comparison studies of organometallics with their carbon analogs, and the results emphasized the importance of the selenium and tin atoms on the photoreactivity of organometallics. Although this dissertation focused on select chemicals, the findings are expected to apply to a broader set of organoselenium and organotin compounds. The main conclusions and significance of each chapter are highlighted in the following paragraphs.

Chapter 2 examined the photochemical reactivity of ebselen in the presence of reactive species sensitizers and scavenging/quenching agents that are frequently used to investigate the photodegradation mechanisms and kinetics of organic contaminants. The key findings are as follows:

- Ebselen exhibited pH-dependent photodegradation at 254 nm with the observed rate constant increasing from 1.73 (± 0.27) × 10^{-3} s^{-1} at pH 4.4 to 13.50 (± 0.43) × 10^{-3} s^{-1} at pH 10.5. This result was unexpected since ebselen does not dissociate,

as evidenced by the consistent molar absorption coefficients at 254 nm for pH 4.5-10.5.

- The observed rate constant for ebselen in solution containing Rose Bengal, a singlet oxygen ($^1O_2$) sensitizer, increased from 7.03 (± 1.20) × 10^{-4} s^{-1} at pH 4.4 to 6.74 (± 1.80) × 10^{-3} s^{-1} at pH 10.2; however, the steady-state $^1O_2$ concentrations were comparable, 3.1 (± 0.5) × 10^{-12} M, for all pH conditions. This result, in combination with the previous finding, suggests that ebselen undergoes base-catalyzed reactions that affect direct and indirect photolysis.
- Enhanced ebselen degradation kinetics were observed during UV-H_2O_2 reactions with t-butanol (a common hydroxyl radical (•OH) scavenger) due to the involvement of secondary radicals. To preclude these issues, sodium pyruvate was employed as a non-radical generating quencher of H_2O_2 to effectively stop the reaction between ebselen and H_2O_2 in •OH sensitized experiments.
- Ebselen reactivity increased in the presence of sodium azide, sorbic acid, and isopropanol (commonly employed reactive species scavenging/quenching agents), highlighting the need for careful consideration of traditional protocols when studying highly reactive organoselenium compounds.

Significance: This chapter represents the first report of the photochemistry of ebselen and provides crucial insight to the larger class of organoselenium molecules. The findings demonstrated the atypical and convoluted photochemistry of ebselen, including for direct photolysis and reaction with singlet oxygen. For instance, photodegradation kinetics of ebselen showed high dependence on the solution pH during direct photolysis at 254 nm and in Rose Bengal-sensitized experiments even though ebselen does not undergo

acid/based dissociation. Further evaluation indicated ebselen reaction with active intermediates ($^3RB^{2-*}$, $O_2^{\bullet-}$, H_2O_2) that are not kinetically-relevant for other organic compounds. Overall, this chapter suggested that conventional reactive species sensitizers (*e.g.,* Rose Bengal, perinaphthenone, H_2O_2, nitrate/nitrite) and quenchers (*e.g.*, sodium azide, sorbic acid, isopropanol) need to be carefully applied in photochemical studies of highly reactive organoselenium compounds. These results will assist future research efforts to accurately evaluate the mechanisms, kinetics, and effects of water quality parameters for photodegradation of other organoselenium molecules.

Chapter 3 described the photochemical fate of triphenyltin chemicals in different water sources by cohesively employing laboratory experiments to calculate second-order rate constants with reactive species and literature-reported photoreactivity of real waters. The significant findings include the following:

- The second-order rate constants for transformation of triphenyltin hydroxide by $^1O_2$, $^{\bullet}OH$, and $^3DOM^*$ were calculated to be $(3.9 \pm 0.52) \times 10^6$ M^{-1} s^{-1}, $(7.81 \pm 0.37) \times 10^8$ M^{-1} s^{-1}, and $(1.41 \pm 0.06) \times 10^6$ M^{-1} s^{-1}, respectively.
- The Aqueous Photochemistry of Environmentally occurring Xenobiotics model was used to evaluate triphenyltin hydroxide half-lives and apparent first-order rate constants in different whole waters using approximately 1308 published reports of reactive species quantum yields.
- For a 1 m water depth and 5 mg_C L^{-1} DOM, the median half-lives of triphenyltin hydroxide followed the order: surface water (157 Sunny Summer Days (SSD)) >

NOM extracts (151 SSD) > wastewater effluent (95 SSD) > stormwater (74 SSD) > wetlands (60 SSD).

- Triphenyltin hydroxide photoreactivity in surface waters matched that in NOM isolates; however, triphenyltin hydroxide degradation was faster in wetlands and waters impacted by wastewater effluent and stormwater.
- Even though the kinetics were apparently slow in the environment (*i.e.*, the half-lives ranged from several weeks to a year, depending on the water quality), photodegradation of triphenyltin hydroxide was still a kinetically-important process compared to other biotic degradation mechanisms.

Significance: This chapter systematically assessed the abiotic transformation mechanisms and kinetics of triphenyltin chemicals in different water sources. The rate of triphenyltin hydroxide degradation was affected by the DOM source, content, and composition of real waters. Overall, the half-lives of triphenyltin hydroxide ranged from several weeks to a year, suggesting the persistence of triphenyltin hydroxide in the aquatic environment. However, based on the model predictions from this chapter, the DOM in water bodies contaminated with triphenyltin hydroxide, namely agricultural wetlands, wastewater effluent, and harbors affected by stormwater runoff, facilitates the $^{1}O_2$ and ^{3}DOM* photodegradation mechanisms. In addition to the direct conclusions about triphenyltin hydroxide fate in different water sources, this chapter also highlights the need for improved water/wastewater treatment of triphenyltin hydroxide to prevent contamination of drinking water supplies and the natural environment.

Chapter 4 investigated the fate of triphenyltin chemicals in engineered systems equipped with UV-based treatment processes (*i.e.,* UV-254, UV-H_2O_2) by determining reaction kinetics, identifying transformation products, and evaluating residual toxicity. The significant findings of this chapter include:

- At 254 nm, similar absorbance profiles were obtained for the neutral and anionic triphenyltin hydroxide species, and the measured molar absorption coefficient was $(8.14 \pm 0.08) \times 10^2$ M^{-1} cm^{-1}.
- The observed time- and fluence-based, pseudo-first-order rate constants for triphenyltin hydroxide photodegradation at 254 nm were $(2.34 \pm 0.16) \times 10^{-3}$ s^{-1} and $(5.18 \pm 0.25) \times 10^{-4}$ cm^2 mJ^{-1}, respectively, at pH 7. The corresponding quantum yield was 0.18 ± 0.02 mol Ein^{-1}.
- Primary water quality parameters, such as solution pH and ionic strength, did not affect the transformation kinetics of triphenyltin hydroxide during UV-254 treatment; however, DOM inhibited triphenyltin hydroxide transformation due to inner filter effects.
- The addition of 16 mM H_2O_2 (~6000 mol H_2O_2/mol triphenyltin hydroxide) enhanced triphenyltin hydroxide degradation by 38% at pH 7, with the observed pseudo-first-order rate constant increasing from $(2.34 \pm 0.16) \times 10^{-3}$ s^{-1} for direct photolysis at 254 nm to $(3.22 \pm 0.20) \times 10^{-3}$ s^{-1} for UV-H_2O_2 treatment.
- The second-order rate constant for transformation of triphenyltin hydroxide by $^{\bullet}OH$ was calculated to be $(7.81 \pm 0.37) \times 10^8$ M^{-1} s^{-1}.
- Using a growth inhibition assay with *Staphylococcus* spp., the transformation products of triphenyltin hydroxide generated during UV-254 and UV-H_2O_2

treatment were determined to be toxicologically active and more potent than triphenyltin hydroxide.

Significance: This chapter examined the effectiveness of the UV-254 and UV-H_2O_2 advanced oxidation processes to transform triphenyltin chemicals into benign products. The calculated fluence-based, pseudo-first-order rate constant indicated only 2-10% triphenyltin hydroxide degradation in typical UV processes employed for drinking water and wastewater treatment. Advanced oxidation increased the removal efficiency of triphenyltin hydroxide to 50-92% with the addition of 16 mM H_2O_2. Although triphenyltin hydroxide degraded, no photoproducts were identified for UV-254 treatment. Four transformation products were identified for advanced oxidation of triphenyltin hydroxide, and hydroxylation of the aromatic rings was the primary reaction mechanism. Based on residual toxicity measurements, the direct photolysis photoproducts were more toxic than the hydroxylation and dehydration products identified for advanced oxidation. This finding confirmed that advanced oxidation not only facilitated faster degradation of organotin chemicals, but also resulted in less toxic phototransformation products compared to UV-254.

5.2 Future Studies

1. Additional research on the occurrence of ebselen in various water systems and its fate in biological and photochemical processes is essential to assess the persistence of ebselen in the ecosystem and its potential toxicity. According to the phototransformation kinetics presented in Chapter 2, ebselen exhibited high photoreactivity in typical irradiation condition of engineered and natural systems.

However, conventional protocols may have overestimated ebselen degradation due to the convoluted effects of reactive species sensitizing and quenching agents due to the generation of kinetically significant active intermediates.

2. Several unanswered questions about the reaction mechanisms of ebselen underlined in Chapter 2 were outside of the scope of this dissertation research and should be addressed in a future study. Some examples include:
    - The pH-dependent photodegradation kinetics of ebselen during direct photolysis and Rose Bengal-sensitized experiments were hypothesized to involve reaction with $O_2^{\bullet-}$. This hypothesis can be investigated by determining the photochemical formation and decay rates of $O_2^{\bullet-}$ in irradiated solutions by the chemiluminescent method with probes (*e.g.,* luminol and methoxy cypiridina luciferin analog).
    - Further deconvolute the observed reaction kinetics of ebselen with NaN_3, sorbic acid, and tert-butanol. Then, develop a protocol to identify the reactive intermediates, such as triplets and/or secondary radicals of sensitizers that are kinetically relevant to ebselen.
3. Appropriate protocols for investigating the aquatic photochemistry of highly reactive organoselenium chemicals must be established. A first step in this direction may be to investigate other triplet photosensitizers with a low quantum yield of $^1O_2$, such as 2-acetonaphthone or 3-methoxy-acetophenone.
4. Elucidate the details of reaction pathways by identifying transformation products of triphenyltin chemicals in natural water systems. As indicated in Chapter 3, the chemical transformation of triphenyltins in natural systems happens through the involvement of $^1O_2$, $^\bullet OH$, and $^3DOM^*$. A systematic investigation on the degradation

products of triphenyltins in natural waters in the presence of DOM will give a more comprehensive picture on the reaction mechanisms involved in natural waters.

Appendix

A. Supplemental Information for Chapter 1

Text A1. Chemical reagents.

Ebselen (EBS; ≥ 98%) and its carbon analog (C-EBS; 95%) were purchased from Sigma-Aldrich (St. Louis, MO) and AstaTech (Bristol, PA), respectively. Unless indicated, other chemicals were obtained from Fisher Scientific (Hampton, NH). Sodium phosphate monobasic monohydrate (> 98%), sodium phosphate dibasic heptahydrate (>98%), and sodium phosphate tribasic dodecahydrate (> 98%) were used to prepare pH buffers. The Rose Bengal (RB; 88%) and perinaphthanone (PN; 97%) $^1O_2$ sensitizers were purchased from Sigma-Aldrich. H_2O_2 (30%, v/v) was used as a $^{\bullet}OH$ sensitizer. Furfuryl alcohol (FFA) and *para*-chlorobenzoic acid (*p*CBA) were employed as probe compounds for $^1O_2$ and $^{\bullet}OH$, respectively. Several scavenging and quenching agents were included in this study: isopropanol (99.9%; Sigma-Aldrich) was used to quench $^{\bullet}OH$; NaN_3 (>99%; Acros Organics) was used to scavenge $^1O_2$ and $^{\bullet}OH$; sorbic acid (MP Biomedicals) was used to quench triplets (also prevents $^1O_2$ production); and, *tert*-butanol (99.5%; Acros Organics) was used to quench $^{\bullet}OH$.

Text A2. Analytical methods.

EBS, C-EBS, and *p*CBA concentrations were measured by liquid chromatography with triple quadrupole tandem mass spectrometry (LC-MS/MS; Thermo UltiMate 3000 with Quantum Access Max mass spectrometer). The LC method employed a 200 µL min^{-1} isocratic mobile phase consisting of a 40:60 (v/v) mixture of (A) 0.1% formic acid in LC-MS-grade water and (B) LC-MS-grade methanol with 0.1% formic acid. Chromatographic separation was carried out on a Waters Symmetry C18 column (2.1×150 mm, 3.5 µm) at 40 °C. The retention times of EBS, C-EBS, and *p*CBA were 5.57, 6.63, and 6.67 min, respectively. The electrospray ionization unit was operated in positive mode for EBS and C-EBS and negative mode for *p*CBA. The other MS/MS operating parameters were as follows: capillary temperature, 270 °C; spray voltage, 3000 V; sheath gas pressure, 40 (arbitrary units); auxiliary gas pressure, 15 (arbitrary units); and, collision gas (argon) pressure, 1.5 Torr. The monitored ion transitions for EBS, C-EBS, and *p*CBA were 276.0 → 183.9, 210.1 → 132.1, and 155.1 → 111.9, respectively.

FFA was analyzed using high-performance liquid chromatography with UV absorbance detection (HPLC-UV; Thermo UltiMate 3000). The sample injection volume was 50 µL, the flow rate was 600 µL min^{-1}, and the column temperature was 40 °C. The isocratic mobile phase was composed of a 25:75 (v/v) mixture of (A) HPLC-grade methanol with 0.1% formic acid and (B) HPLC-grade water with 0.1% formic acid. FFA was separated on an Accucore C18 (4.6×150 mm, 2.6 µm) analytical column, and the retention time was 4.6 min. The UV absorbance of FFA was measured at 220 nm.

Text A3. Quantum yield calculation.

The apparent quantum yield ($\phi_{\lambda,app}$) of EBS and C-EBS were calculated according to Eq. A1 [181].

$$\phi_{\lambda,app} = \frac{k'_{d,\lambda,app}}{2.303\ \ell\ \varepsilon_{\lambda,app}\ I_0} \quad \text{(Eq. A1)}$$

In Eq. A1, $k'_{d,\lambda,app}$ is the apparent, time-based pseudo-first-order rate constant (s^{-1}) for direct photolysis at wavelength λ, $\varepsilon_{\lambda,app}$ is the apparent molar absorption coefficient (M^{-1} cm^{-1}) for the considered wavelength, ℓ is the optical pathlength (cm), and I_0 is the net photon flux (Ein L^{-1} s^{-1}). The net photon flux of the 254 nm and 365 nm systems was reported in section 2.3 of the manuscript.

Text A4. Transient absorption spectroscopy.

Nanosecond laser flash photolysis experiments were conducted to (i) evaluate the formation of transient EBS species (*e.g.*, triplet EBS ($^3EBS^*$) or the EBS radical cation ($EBS^{\bullet+}$)) by direct photoexcitation and (ii) determine the second-order reaction rate constant of EBS with triplet sensitizers. Transient absorption spectroscopy was carried out using the second- or third- harmonic frequency from a Q-switched Nd:YAG laser (Continuum Surelight II; pulse width, 8 ns) for excitation. The energy of the 355 nm and 532 nm excitation was 25 mJ cm^{-2} $pulse^{-1}$ or less. Transient absorption spectra were recorded using a 75-W Xenon arc lamp as the probe light source, an Action SP-150 monochromator, and a R-928 Hamamatsu photomultiplier tube. A complete description of the laser flash photolysis instrument has been provided elsewhere [142]. To evaluate the formation of transient EBS species, a solution containing 150 µM EBS and 5 mM phosphate buffer was prepared in 50% acetonitrile. The investigated pH values included 4.4, 5.2, 7.3, 9.6, and 11.2. A laser pulse at 355 nm was used for excitation, and kinetic traces were recorded for every 25 nm across the 400-700 nm range. The transient absorption measurements were taken for EBS samples exposed to air and samples sparged with argon gas for 15 min to inhibit potential quenching of reactive species by oxygen.

To determine the second-order rate constants for EBS with triplet sensitizers, 2 mL of 5 µM RB in 5 mM phosphate-buffered DI water at pH 4.4-11.2 (same pH values as above) was sparged with argon for 10 min. Selective excitation of RB was carried out at 532 nm, and the time-dependent change in absorbance (ΔA) for $^3RB^{2-*}$ was monitored at 600 nm.

Aliquots of 10 µL containing EBS in 50% acetonitrile were sequentially added, up to a total concentration of 70 µM, to quench $^{3}RB^{2-}$*. The 600-nm decay traces were fit to a single-exponential decay model to obtain the pseudo-first-order decay constant [87,142]. The absorption spectra of the experimental solutions were recorded with a JASCO V-570 double-beam spectrophotometer between laser flashes to confirm no photodegradation of EBS and RB.

Table A3. List of triplet species and/or active intermediates formed by sensitizing, scavenging, and quenching agents in irradiated aqueous solutions.

Sensitizer, scavenger, or quencher	Active intermediates formed upon irradiation
Rose Bengal	$^3RB^{2-*}$, $RB^{\bullet 3-}$, $RB^{\bullet -}$, $^1O_2$, $O_2^{\bullet -}$, and H_2O_2 [67,68]
Nitrate/nitrite	$^\bullet NO_2$, $^\bullet NO$, $O_2^{\bullet -}$, and $^\bullet OH$ [182]
Hydrogen peroxide	$^\bullet OH$, $HO_2^\bullet$, and H_2O_2 [182]
Sorbic acid	Triplet sorbic acid [183]
Isopropanol	Hydrogen transfer leading to hydroxy isopropyl radical [109]
tert-butanol	$R^\bullet$ and $ROO^\bullet$ (formed by reaction with $^\bullet OH$) [54]

Table A4. Second-order rate constants for EBS reaction with $^3RB^{2-*}$ were calculated at various conditions to confirm a lack of dependence on solution pH. Furthermore, the measured rate constants confirmed the high reactivity of EBS with $^3RB^{2-*}$.

pH	$k''_{^3RB^{2-*},\,EBS}$ ($M^{-1}\,s^{-1}$)
4.4	3.95×10^8
5.2	4.50×10^8
7.3	4.45×10^8
9.6	4.26×10^8
11.2	4.33×10^8

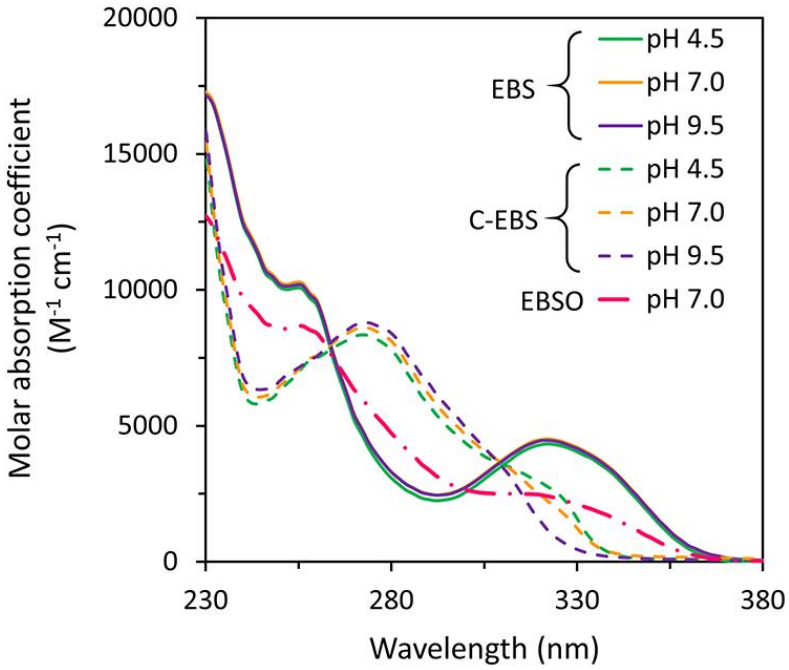

Figure A6. The molar absorption coefficients of EBS (20 mg L^{-1}), C-EBS (20 mg L^{-1}), and ebselen selenoxide (EBSO, 20 mg L^{-1}) for 230-380 nm and select pH values. Solution pH was adjusted with 10 mM phosphate buffer. EBS and C-EBS do not undergo acid dissociation reactions and are present in solution as neutral molecules; therefore, solution pH had a negligible influence on the measured absorbance spectra. Note, the concentrations of EBS and C-EBS were higher than the kinetics experiments to ensure the sensitivity of molar absorption coefficients measured in the 230-380 nm range.

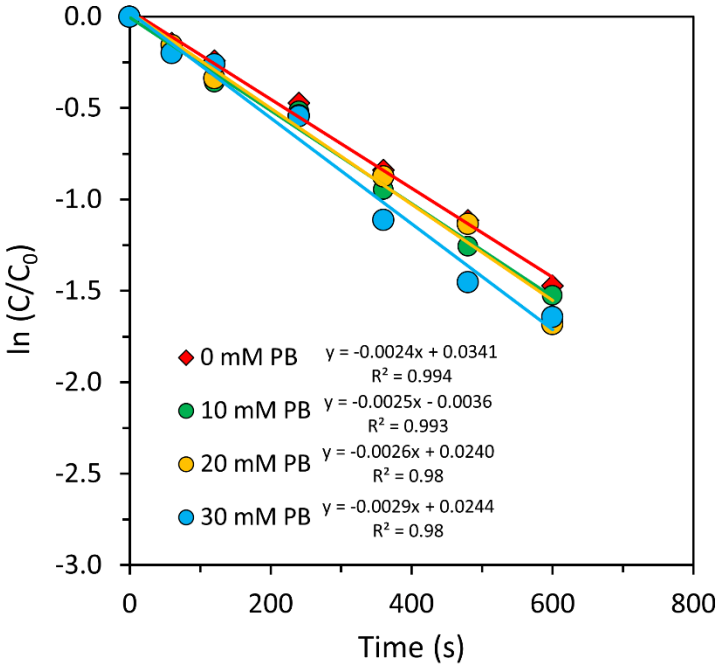

Figure A7. Observed degradation trends of EBS (initial concentration 3.6 µM) in DI water with 0, 10, 20, and 30 mM phosphate buffer for irradiation at 254 nm. The measured pH of all solutions was 7.2 ± 0.1; note, the pH of the 0 mM phosphate-buffered solution was adjusted with 1 mM NaOH. The observed rate constants for EBS with 0, 10, 20, and 30 mM phosphate buffer were 2.43 (± 0.47) × 10^{-3} s^{-1}, 2.55 (± 0.40) × 10^{-3} s^{-1}, 2.63 (± 0.55) × 10^{-3} s^{-1}, and 2.89 (± 0.61) × 10^{-3} s^{-1}, respectively.

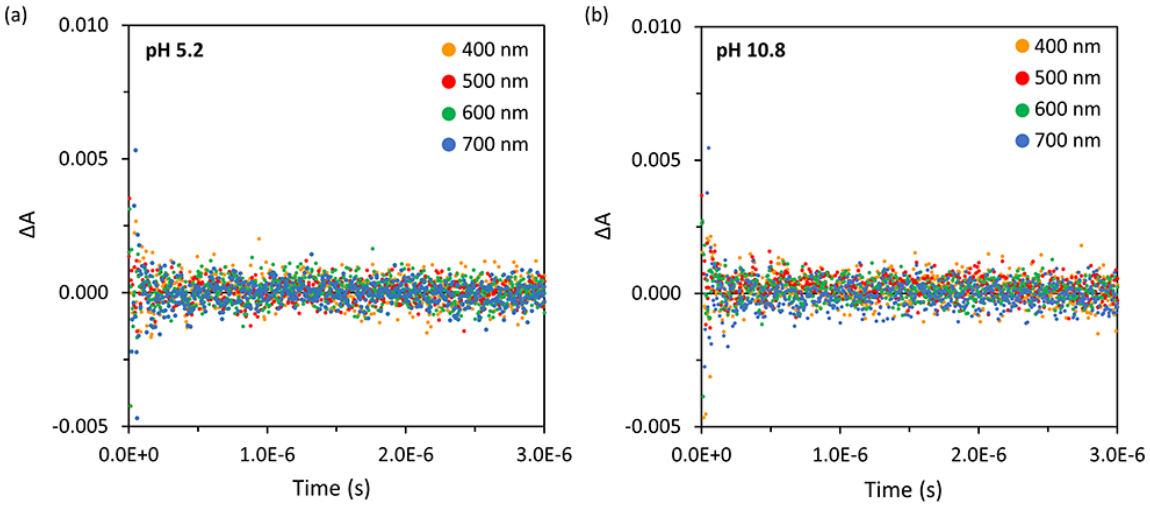

Figure A8. Transient absorption spectroscopy of EBS (150 µM) in 50% acetonitrile with 5 mM phosphate buffer at (a) pH 5.2 and (b) pH 10.8. Excitation was conducted at 355 nm, and absorbance measurements were recorded for every 25 nm in the 400-700 nm range (for clarity, data are only shown for 100 nm intervals). Transient signals corresponding to $^{3}EBS^{*}$ or $EBS^{\bullet+}$ were not observed, suggesting a low triplet yield for excitation at 355 nm.

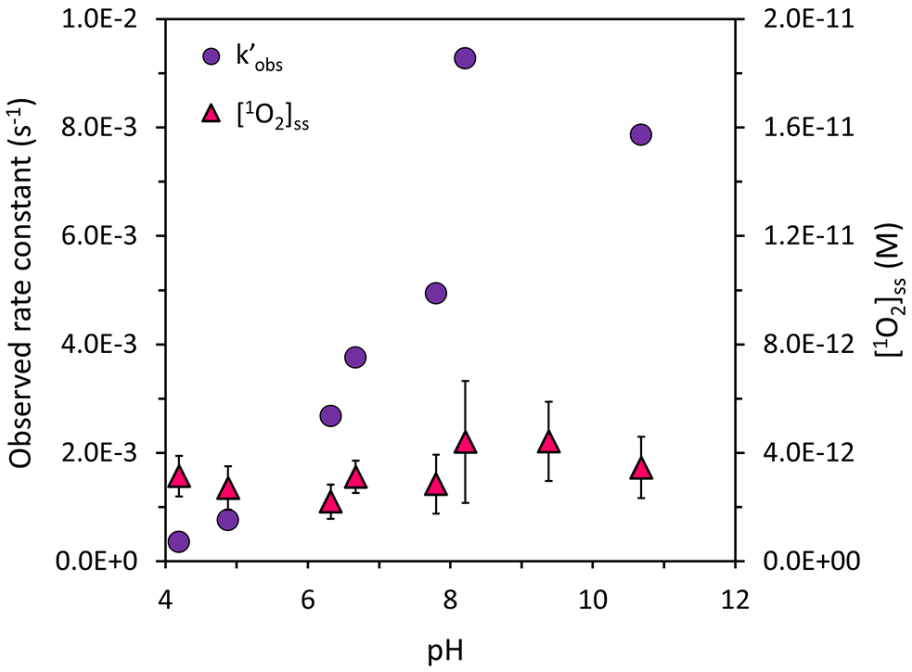

Figure A9. Observed pseudo-first-order rate constants for EBS (3.6 µM) photodegradation and steady-state $^1O_2$ concentrations in solutions containing 0.5 µM PN, 0.2 mM FFA, and 5 mM phosphate buffer. The rate constants and $^1O_2$ concentrations were calculated from time series experiments with seven data points. Error bars represent 95% confidence intervals on the mean rate constant from the time series experiments. Similar to the data obtained from RB-sensitized solutions, EBS exhibited pH-dependent reaction kinetics in PN-sensitized solutions even though steady-state concentrations of $^1O_2$ were consistent, namely 3.3 (± 0.8) × 10^{-12} M, for all pH conditions.

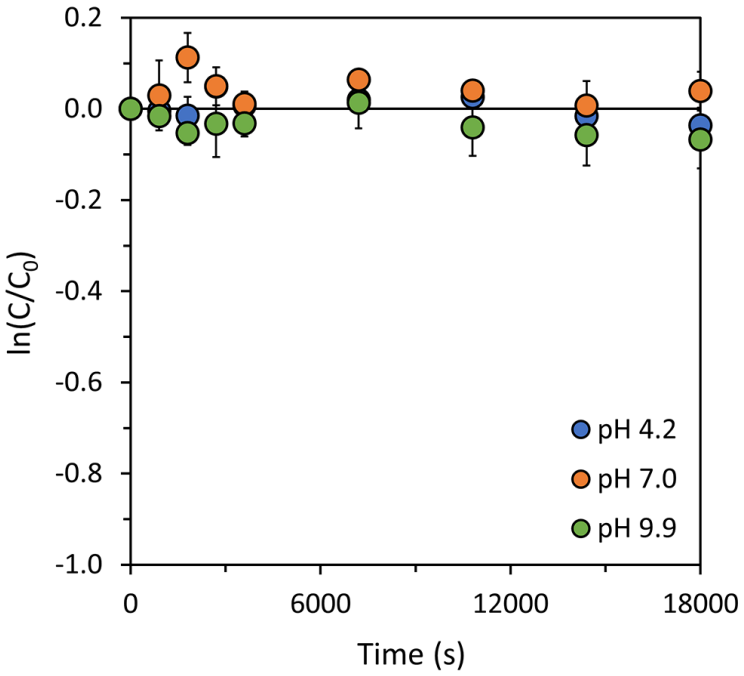

Figure A10. Observed change in C-EBS (3.6 µM) concentration during irradiation with light at 365 nm. The solutions also contained 40 µM RB, 0.2 mM FFA, and 5 mM phosphate buffer. The steady-state concentrations of $^1O_2$ measured in the pH 4.2, 7.0, and 9.9 solutions were 3.05×10^{-12} M, 3.11×10^{-12} M, and 3.36×10^{-12} M, respectively. Contrary to EBS, C-EBS exhibited negligible degradation in RB-sensitized solutions. The plotted symbols represent the mean of triplicate experiments, and the error bars are standard deviation.

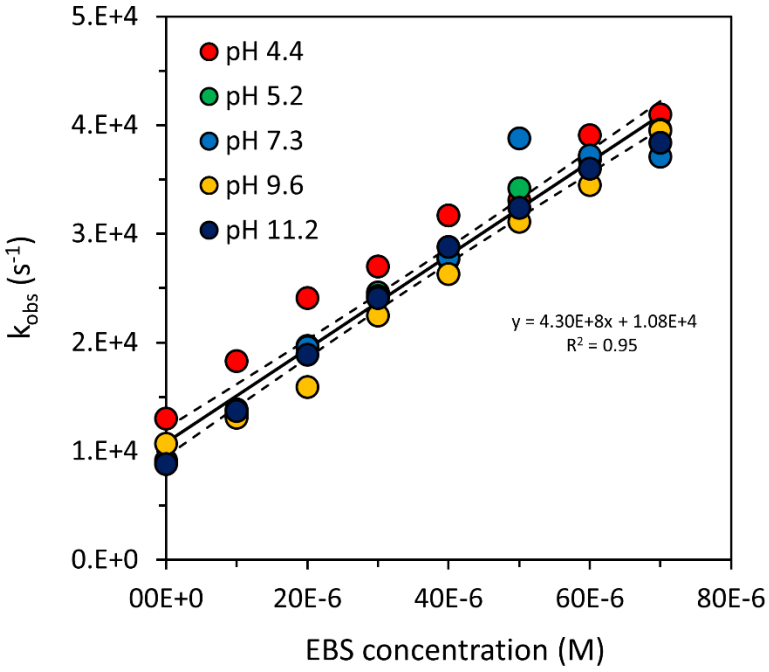

Figure A11. Stern-Volmer plot showing the decay rate constant of $^3RB^{2-}$* as a function of EBS concentration and pH. These data were used to calculate the second-order rate constant, $k''_{^3RB^{2-*},EBS}$. These transient absorption experiments were conducted with solutions consisting of 5 µM RB, 5 mM phosphate buffer (to maintain the pH values reported in the legend), and incremental addition of 10 µM EBS (up to 70 µM). The solid black line is the mean slope of the aggregate data set, and the dashed black lines represent the lower and upper 95% confidence bands. The calculated rate constants from individual pH values are reported in Table S2. These data confirm high reactivity of EBS with $^3RB^{2-}$*, and the average second-order rate constant of EBS with $^3RB^{2-}$* was 4.30 (± 0.15) × 10^8 $M^{-1}s^{-1}$.

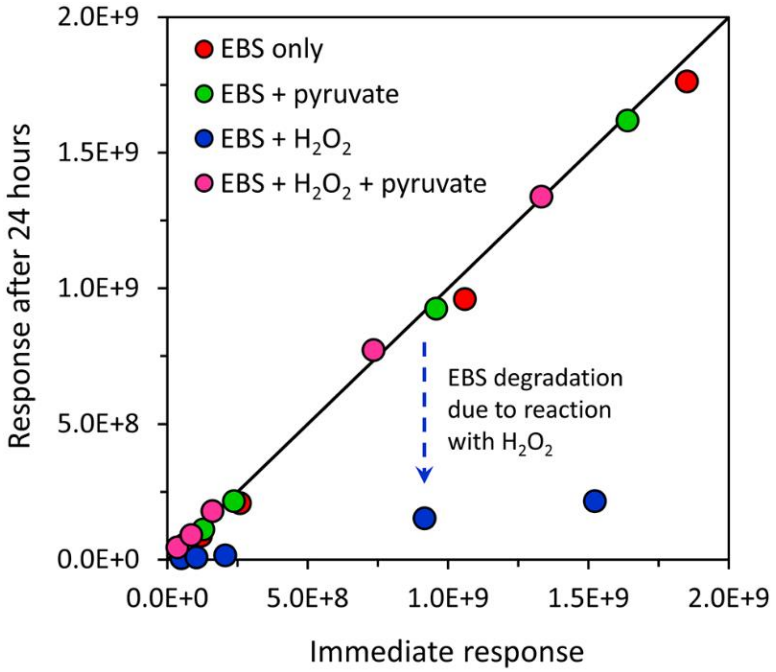

Figure A12. LC-MS/MS response of EBS measured immediately after preparation and after 24 h of storage in the following solutions: (i) 0.36-36 µM EBS; (ii) 0.36-36 µM EBS + 7.5 mM sodium pyruvate; (iii) 0.36-36 µM EBS + 0.5 mM H_2O_2; and, (iv) 0.36-36 µM EBS + 0.5 mM H_2O_2 + 7.5 mM sodium pyruvate. The response of EBS measured after 24 h was similar to the response measured immediately after sample preparation for the EBS only, EBS + pyruvate, and EBS + H_2O_2 + pyruvate scenarios. These results suggest that (i) hydrolysis reactions were negligible, (ii) sodium pyruvate did not react with EBS, and (iii) sodium pyruvate effectively quenched the residual H_2O_2. The addition of pyruvate influenced the ionization efficiency of EBS during LC-MS/MS analysis and resulted in a slightly lower response compared to solutions without pyruvate. For the EBS + H_2O_2 scenario, the response of EBS decreased during the 24 h storage time, indicating EBS reaction with H_2O_2.

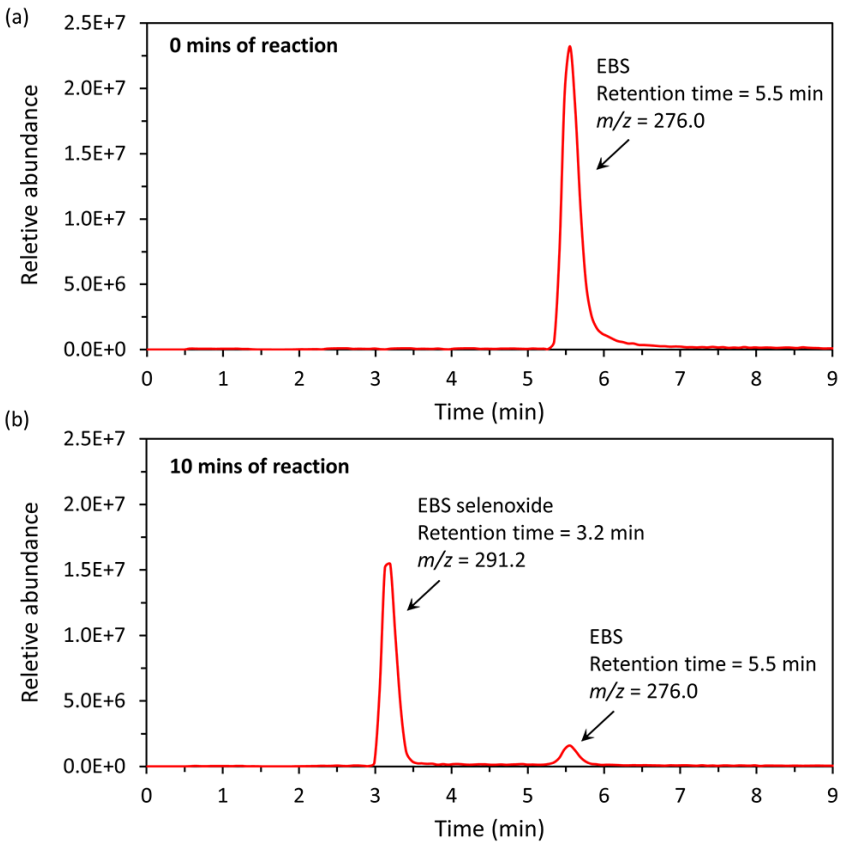

Figure A13. Chromatograms of a solution with 3.6 µM EBS, 50 µM H_2O_2, and 5 mM phosphate buffer after (a) 0 min and (b) 10 min of reaction. For (a), 50 µM H_2O_2 was added to a solution containing 3.6 µM EBS, 5 mM phosphate buffer, and 7.5 mM sodium pyruvate. The sodium pyruvate effectively quenched the added H_2O_2, preventing EBS interaction with H_2O_2. For (b), 50 µM H_2O_2 was added to a solution containing 3.6 µM EBS and 5 mM phosphate buffer. After 10 min, 7.5 mM sodium pyruvate was added to quench residual H_2O_2. EBS reaction with H_2O_2 generated EBS selenoxide (EBSO). The peaks at 5.5 min (m/z, 276.0 → 183.9) and 3.2 min (m/z, 291.2 → 195.4) represent EBS and EBSO (confirmed by standard), respectively.

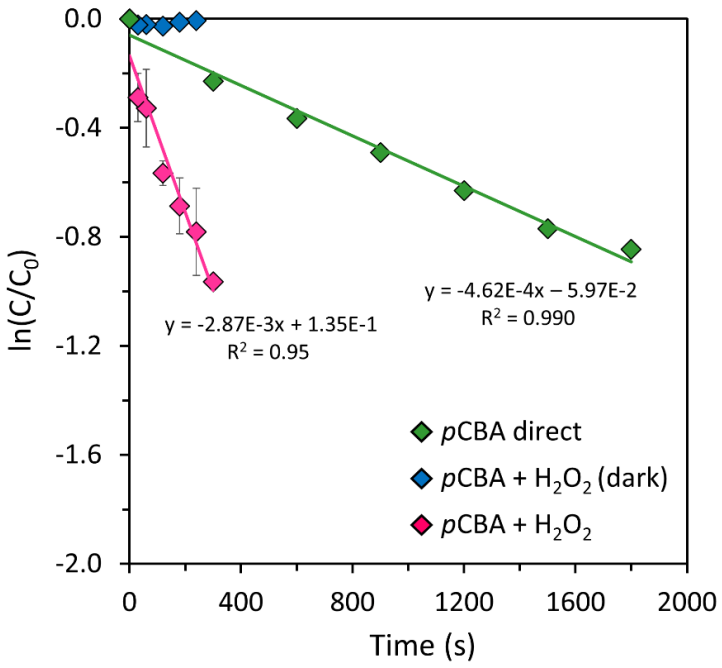

Figure A14. Degradation kinetics of 75 µM pCBA at pH 7.1 for direct photolysis at 254 nm, UV-H_2O_2 treatment (with 254 nm), and reaction with H_2O_2 in the dark. The initial H_2O_2 concentration was 5 µM, and solution pH was maintained with 5 mM phosphate buffer. The observed pseudo-first-order rate constant for pCBA degradation ($\boldsymbol{k'_{d,pCBA}}$) was 4.62 (± 0.65) × 10^{-4} s^{-1}. The error on the direct photolysis rate constant represents the 95% confidence interval on the mean rate constant from the time-series experiment (n = 7). The plotted symbols for the pCBA + H_2O_2 dataset represent the mean of triplicate experiments, and the error bars are standard deviation. Note, EBS and H_2O_2 were not added to the direct photolysis mixture for pCBA, but EBS was present in the pCBA + H_2O_2 solutions for analysis of competition kinetics.

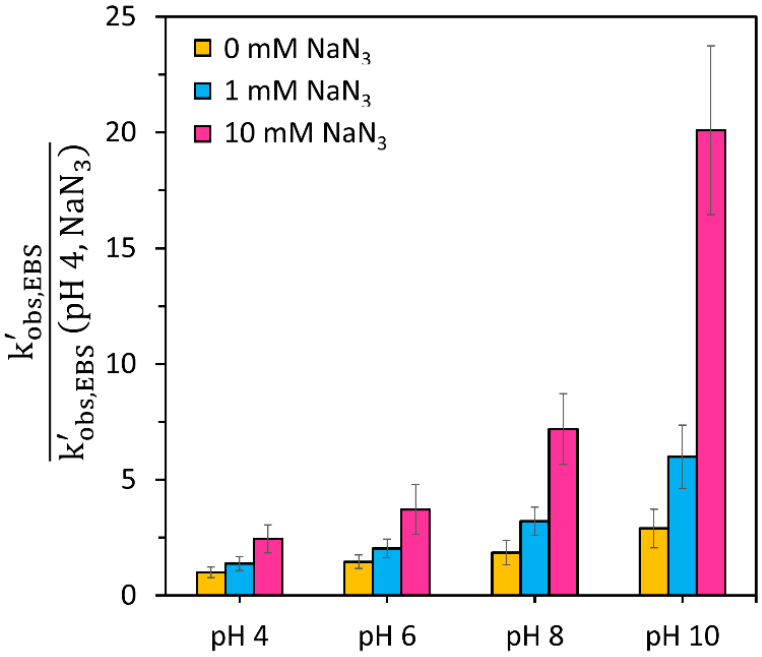

Figure A15. Observed pseudo-first-order rate constants for irradiation of EBS at 254 nm in the presence of 0, 1, and 10 mM NaN_3 at pH 4, 6, 8, and 10. Note that all results are normalized to the rate constant at pH 4 with 0 mM NaN_3 to emphasize the relative differences. The initial EBS concentration was 3.6 µM, and the pH was maintained with 5 mM phosphate buffer. Error bars correspond to propagated 95% confidence intervals on the mean rate constants from duplicate time series experiments (n = 7 × 2 = 14).

B. Supplemental Information for Chapter 3

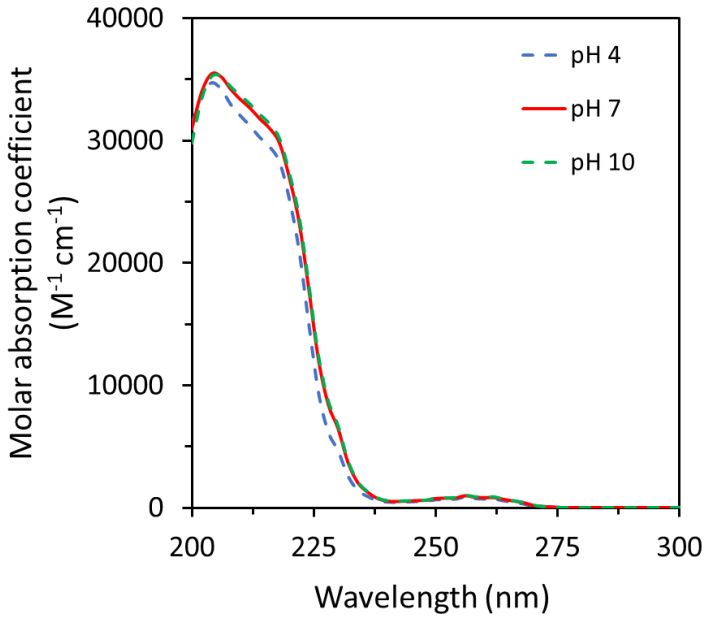

Figure B16. The molar absorption coefficients of TPTH at pH 4, 7, and 10. The solutions contained 27 µM TPTH, 5 mM phosphate buffer, and 50% methanol (for TPTH solubility) in deionized water. Data were measured for 200-500 nm but are only reported for the 200-300 nm range, because the absorbance above 300 nm was below the instrument detection limit (i.e., 10 M^{-1} cm^{-1}).

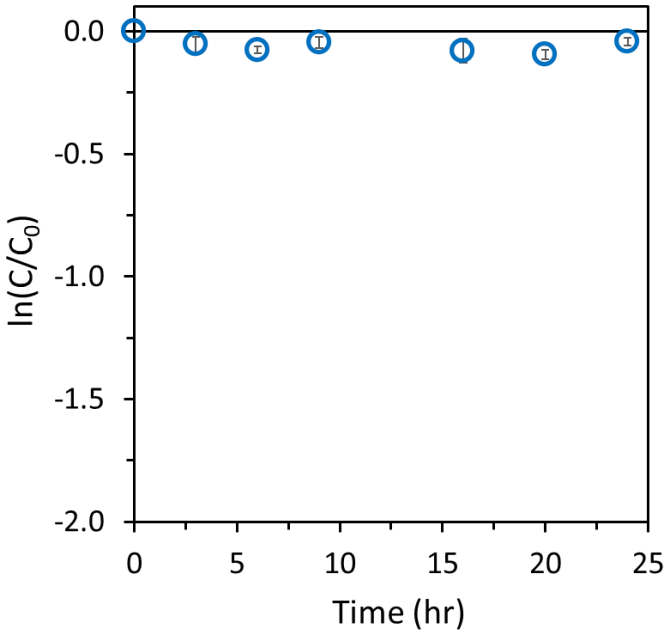

Figure B17. Direct photolysis of TPTH (initial concentration 2.7 µM) in deionized water at 365 nm. The solution pH was adjusted to 7.0 ± 0.1 with 5 mM phosphate buffer.

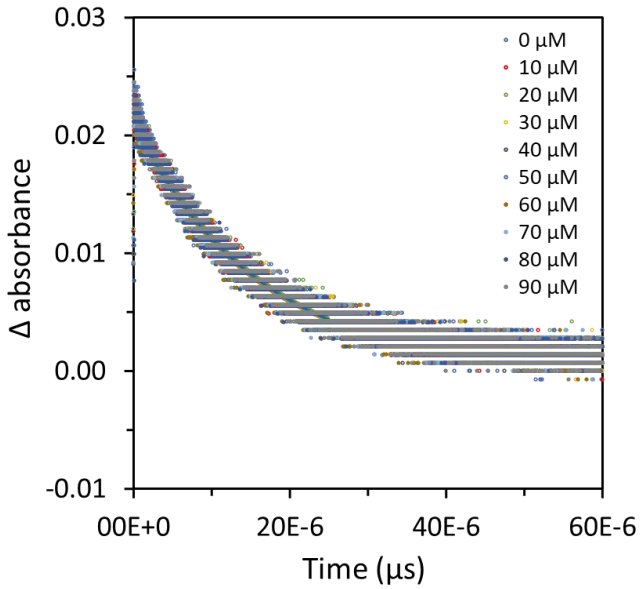

Figure B18. Transient absorption decay curves of ^{3}CBBP* at 550 nm for 0-90 µM TPTH. Additional details are available in Section 2.3 and Figure 2 of the main manuscript.

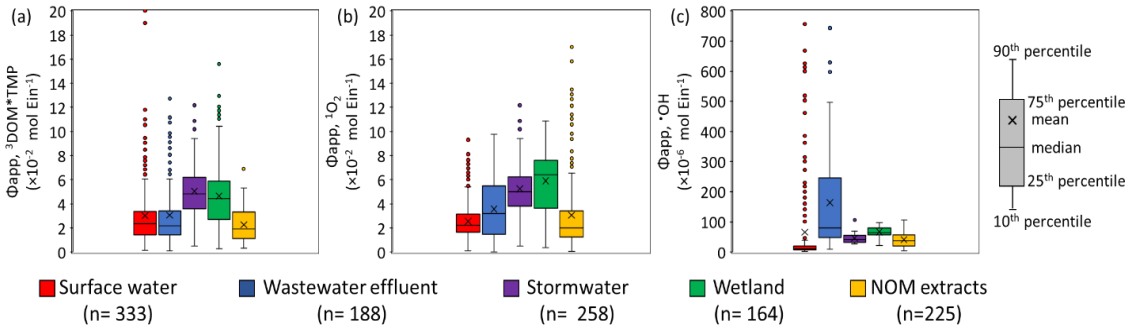

Figure B19. Box-and-whisker diagrams of the quantum yields of (a) $^1O_2$, (b) $^\bullet$OH, and (c) ^{3}DOM* for different water sources. The data were collected from Wasswa et al. [139].

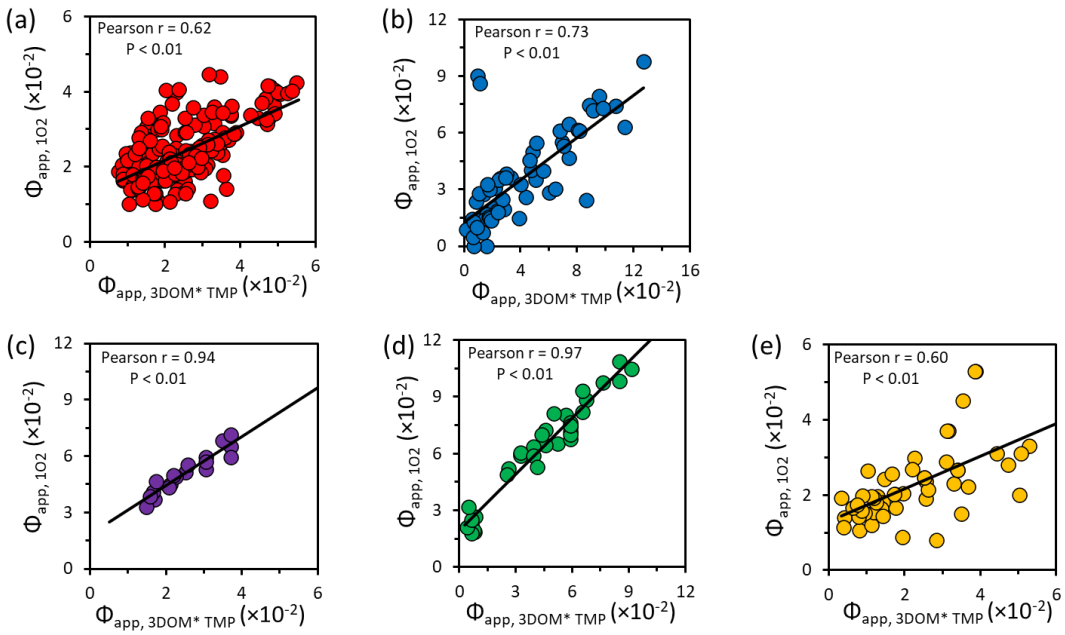

Figure B20. Linear correlations were observed for the quantum yields of $^1O_2$ and $^3DOM^*$ in (a) surface water, (b) wastewater effluent, (c) stormwater, (d) wetlands, and (e) NOM extracts. The data were obtained from Wasswa et al. [139]. The linear regressions were used to estimate missing $\boldsymbol{\phi}_{^1O_2}$ or $\boldsymbol{\phi}_{^3DOM^*}$ parameters for select water sources.

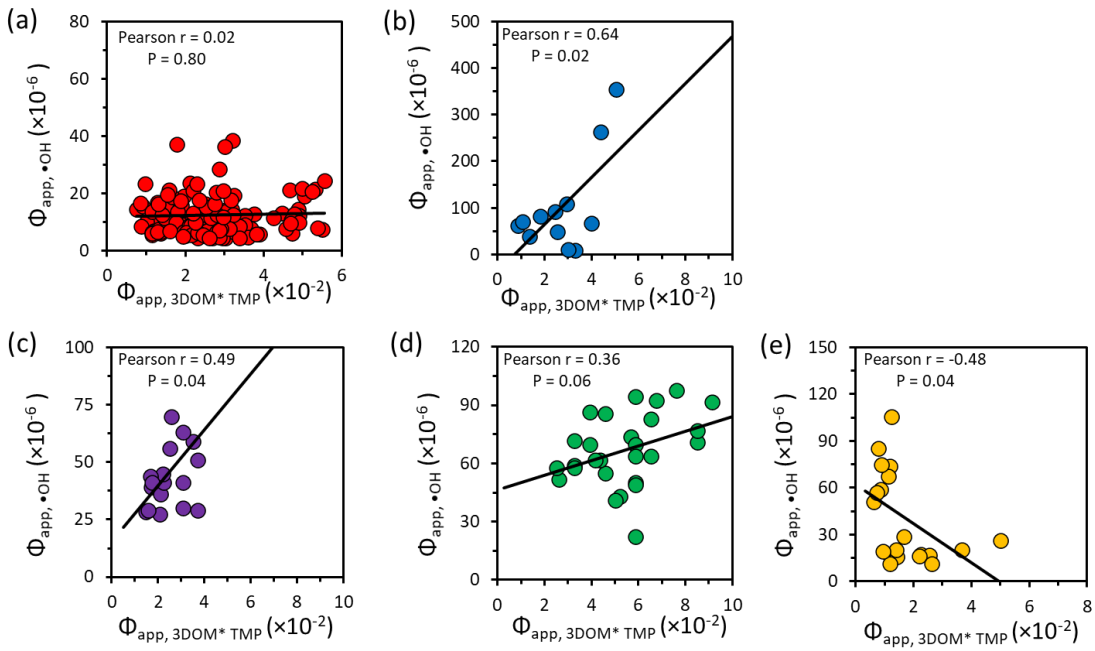

Figure B21. Linear correlations were not observed for the quantum yields of •OH and ^{3}DOM* in (a) surface water, (b) wastewater effluent, (c) stormwater, (d) wetlands, and (e) NOM extracts. The data were obtained from Wasswa et al. [139]. No convincing correlations were observed between the quantum yields; therefore, missing $\boldsymbol{\phi_{\bullet OH}}$ parameters were estimated using the median value for that water source.

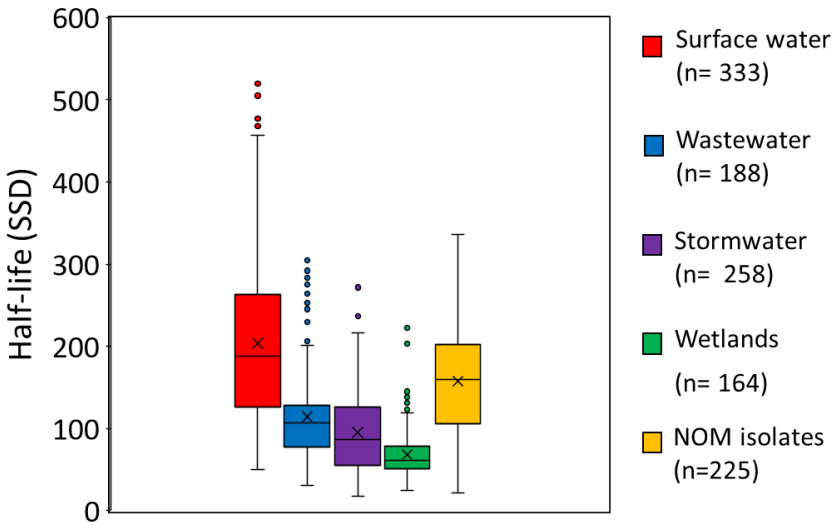

Figure B22. The distribution of TPTH half-lives in different water sources with 5 mg_C L^{-1} DOM. The individual half-lives were calculated for 1 m water depth in the APEX photochemical model using the quantum yields from Figure B4, the rate constants for TPTH reaction with reactive species (Section 3.1 of the main manuscript), and the following water chemistry parameters: 10^{-6} M NO_2^-; 10^{-4} M NO_3^-; 10^{-3} M HCO_3^-; and, 10^{-5} M CO_3^{2-}.

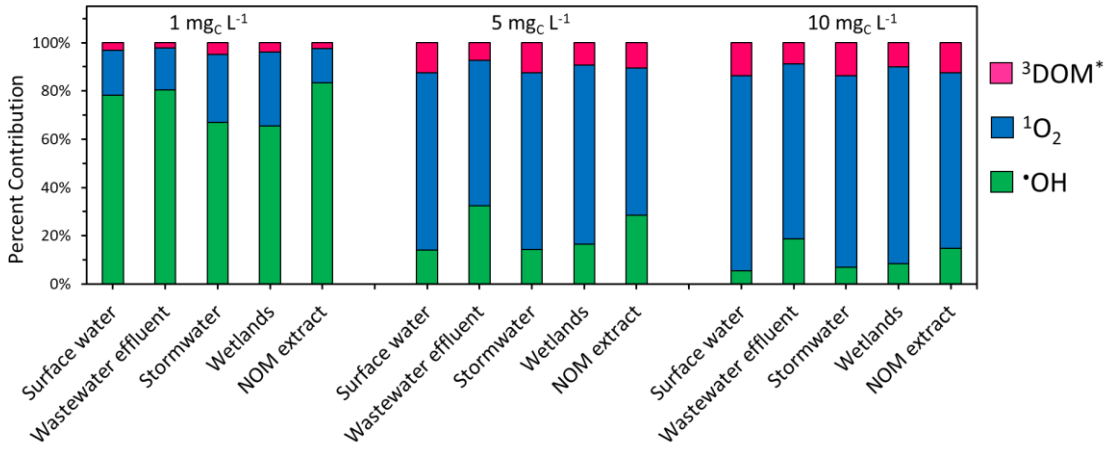

Figure B23. The percent contributions of $^1O_2$, $^\bullet OH$, and $^3DOM^*$ to TPTH photodegradation in different water sources with 1, 5, and 10 mg_C L^{-1} and a 5 m water depth. The results were obtained for solutions containing 10^{-6} M NO_2^-, 10^{-4} M NO_3^-, 10^{-3} M HCO_3^-, and 10^{-5} M CO_3^{2-}.

C. Supplemental Information for Chapter 4

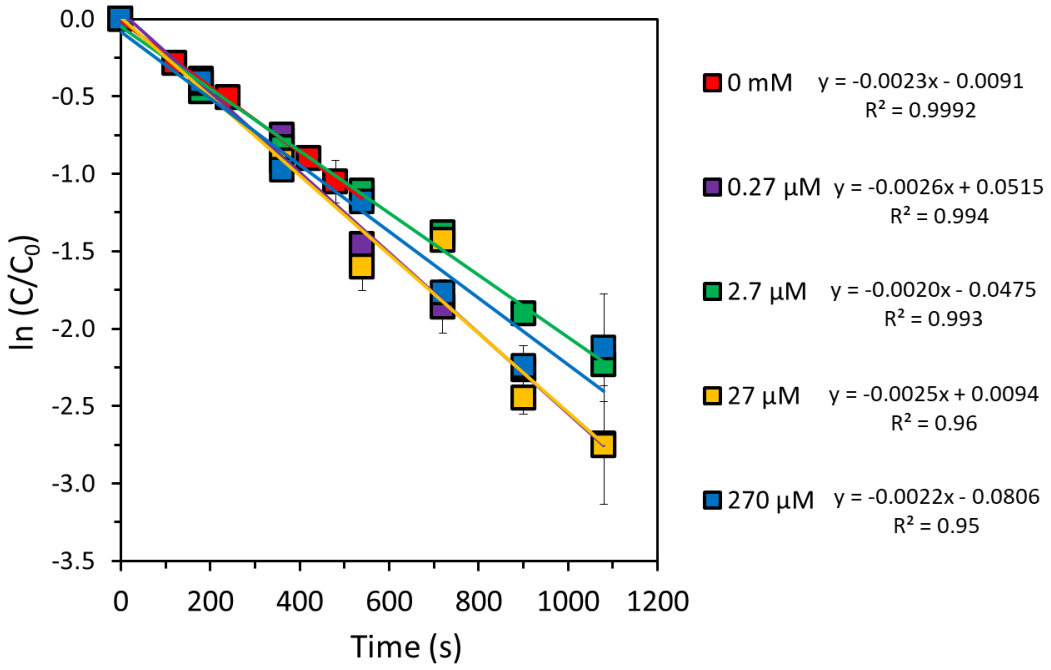

Figure C1. Observed degradation profiles of 2.7 µM TPTH for irradiation at 254 nm with 0, 0.27, 27, and 270 µM H_2O_2. The measured pH of all solutions was 7.0 ± 0.2. Except for the 0 mM H_2O_2 condition, all other solutions included 75 µM pCBA to enable competition kinetics. The plotted symbols represent the mean of triplicate experiments, and the error bars are standard deviation. The observed rate constants for TPTH with 0, 0.27, 27, and 270 µM H_2O_2 were (2.1 ± 0.2) × 10^{-3} s^{-1}, (2.6 ± 0.2) × 10^{-3} s^{-1}, (2.0 ± 0.2) × 10^{-3} s^{-1}, (2.5 ± 0.6) × 10^{-3} s^{-1}, and (2.2 ± 0.5) × 10^{-3} s^{-1}, respectively. The results indicate that the hydroxyl radical contribution to TPTH degradation was minimal for these H_2O_2 concentrations.

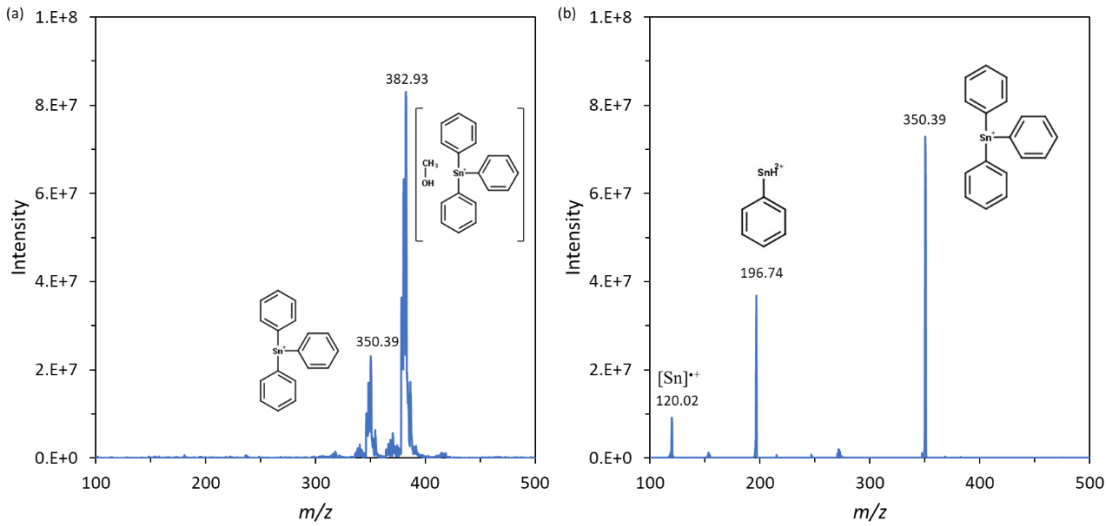

Figure C2. TPTH analysis by (a) MS and (b) MS/MS. The 54 µM TPTH solution was prepared in 100% methanol and directly injected into the mass spectrometer using positive electrospray ionization. The two peaks observed in (a) correspond to TPTH and a TPTH-methanol adduct. The fragmentation pattern in (b) was obtained for the TPTH-methanol adduct (m/z 382.52) with a collision energy of 35 V, but the fragmentation pattern was the same for m/z 350.39. Note, the "2+" on the fragment with m/z 196.74 corresponds to the tin oxidation state (Sn II).

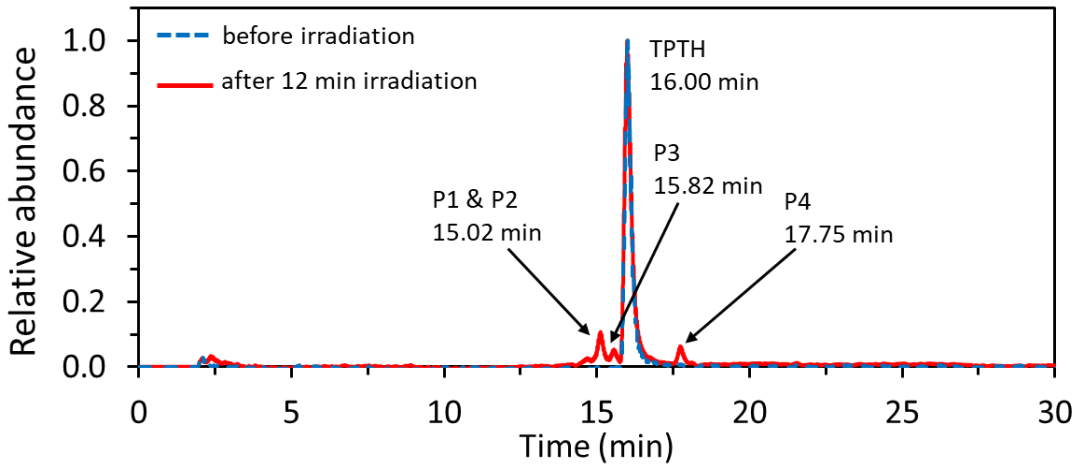

Figure C3. Representative chromatograms showing the total ion current for solutions with 54 µM TPTH and 16 mM H_2O_2 (to sensitize production of •OH) before and after 12 min of irradiation at 254 nm. The mass spectrum acquisition was set to collect data for m/z 100-500.

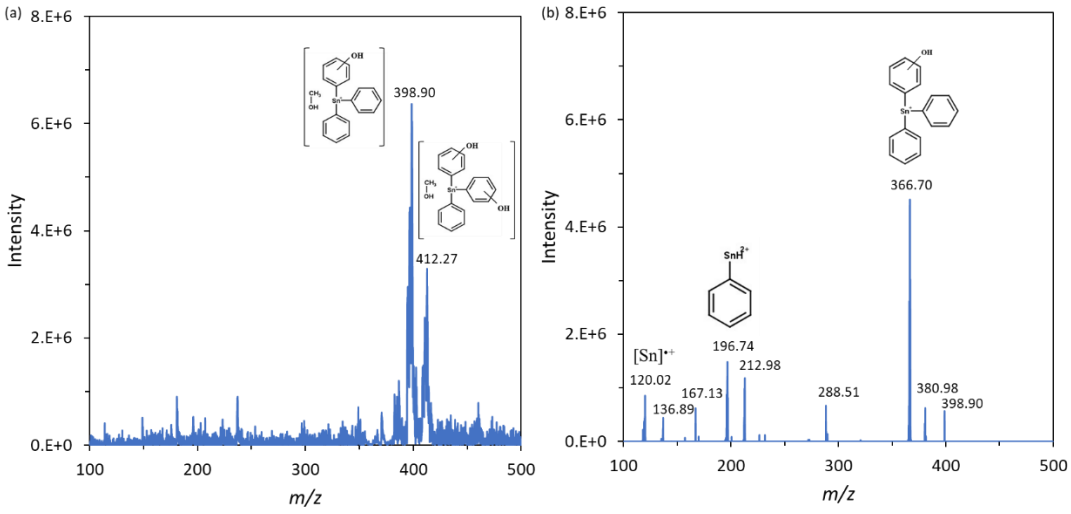

Figure C4. Analysis of a solution that initially contained 54 µM TPTH and 16 mM H_2O_2 after 12 min of irradiation using (a) MS and (b) MS/MS. Positive electrospray ionization was used for both analyses. The spectra in (a) were extracted at a retention time of 15.02 min and show the P1 and P2 photoproducts. The fragmentation pattern in (b) was obtained for m/z 398.9 (corresponding to P1) with a collision energy of 35 V, but a similar fragmentation pattern was obtained for P2. Note, the "2+" on the fragment with m/z 196.74 corresponds to the tin oxidation state (Sn II).

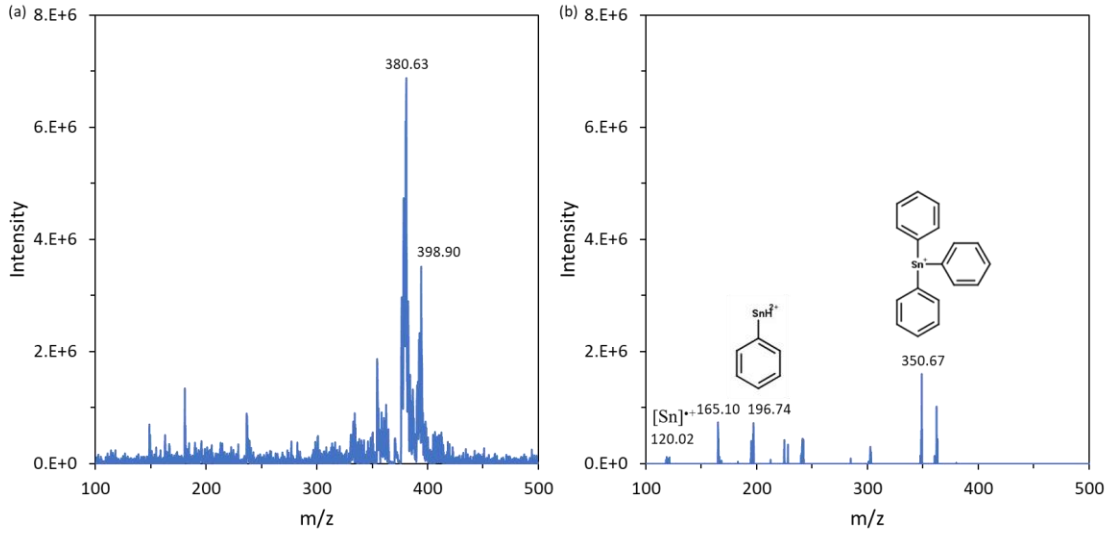

Figure C5. Mass spectrum and fragmentation pattern obtained from solution that initially contained 54 µM TPTH and 16 mM H_2O_2 after 12 min of irradiation using (a) MS and (b) MS/MS. The spectra in (a) were extracted at a retention time of 17.34 min and show the P4 photoproduct. The fragmentation pattern in (b) was obtained for m/z 380.63 with a collision energy of 35 V. Note, the "2+" on the fragment with m/z 196.74 corresponds to the tin oxidation state (Sn II).

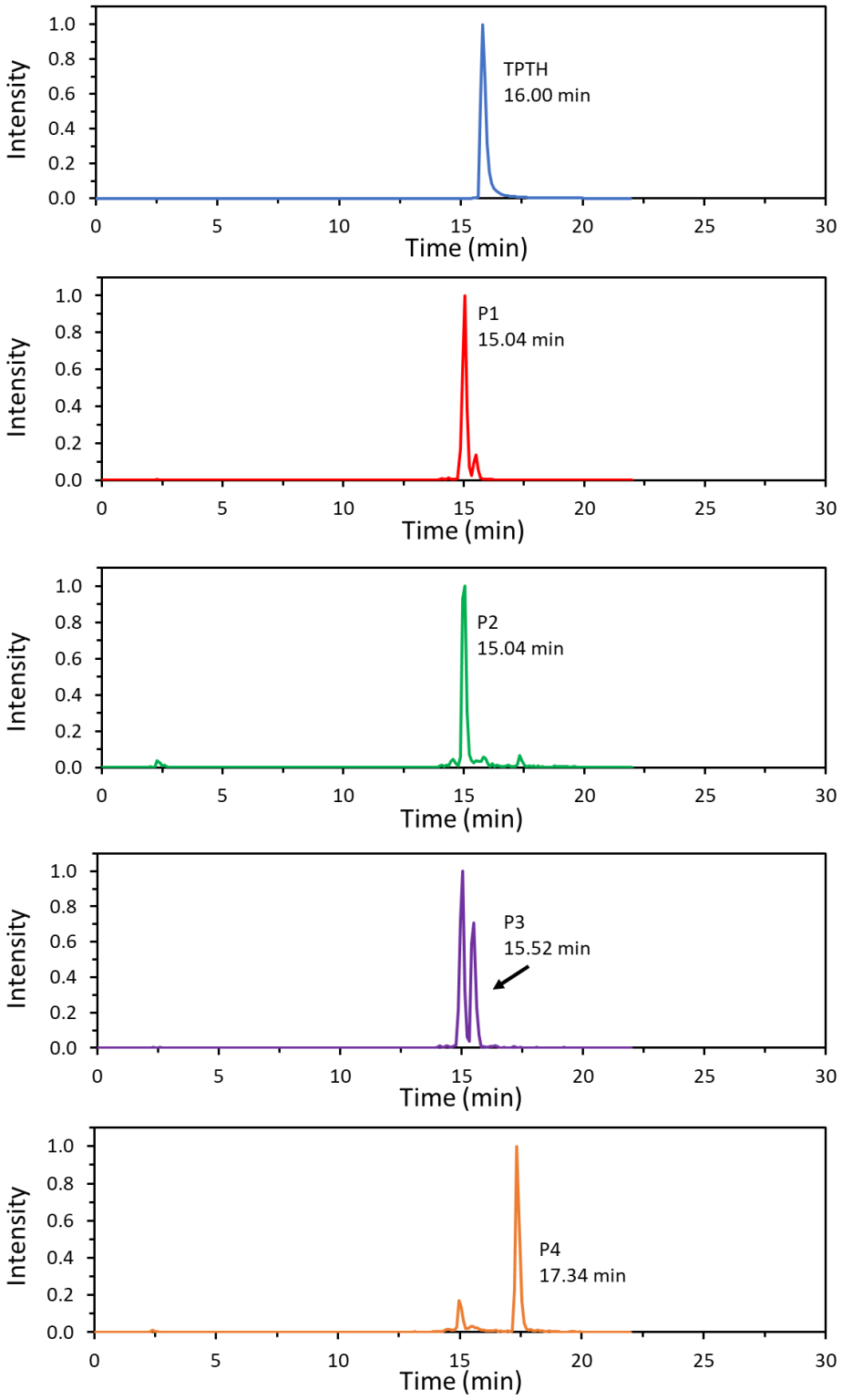

Figure C6. Characteristic chromatograms of TPTH and the primary photoproducts listed in Table 4.2 (main manuscript). The analyzed sample stemmed from 6 min of UV-H_2O_2 treatment of a solution with 54 µM TPTH and 16 mM H_2O_2.

Reference

1. Rai, V.; Vajpayee, P.; Singh, S. N.; Mehrotra, S., Effect of chromium accumulation on photosynthetic pigments, oxidative stress defense system, nitrate reduction, proline level and eugenol content of Ocimum tenuiflorum L. *Plant science* **2004,** *167*, (5), 1159-1169.
2. Halpern, J., Organometallic chemistry at the threshold of a new millennium. Retrospect and prospect. *Pure and Applied Chemistry* **2001,** *73*, (2), 209-220.
3. Jirásko, R.; Holčapek, M., Structural analysis of organometallic compounds with soft ionization mass spectrometry. *Mass spectrometry reviews* **2011,** *30*, (6), 1013-36.
4. Jones-Lepp, T. L.; Momplaisir, G.-M., New applications of LC–MS and LC–MS2 toward understanding the environmental fate of organometallics. *TrAC Trends in Analytical Chemistry* **2005,** *24*, (7), 590-595.
5. Pruchnik, F. P., *Organometallic Chemistry of the Transition Elements*. Plenum Press: New York, 1990.
6. Koubkova, L.; Vyzula, R.; Vojtesek, B.; Hrstka, R., a Mini Review of Organometallic Compounds and Their Anticancer Properties. *Supplementum ad Acta Musei Moraviae* **2013,** *1984*.
7. P. Mangalgiri, K.; Adak, A.; Blaney, L., Organoarsenicals in poultry litter: Detection, fate, and toxicity. *Environment International* **2015,** *75*, 68-80.
8. Mangalgiri, K. P.; Blaney, L., Elucidating the Stimulatory and Inhibitory Effects of Dissolved Organic Matter from Poultry Litter on Photodegradation of Antibiotics. *Environmental Science & Technology* **2017,** *51*, (21), 12310-12320.

9. Adak, A.; Mangalgiri, K. P.; Lee, J.; Blaney, L., UV irradiation and UV-H2O2 advanced oxidation of the roxarsone and nitarsone organoarsenicals. *Water Research* **2015,** *70*, 74-85.

10. Alexander, C.; Nithyakumar, A.; Paul, M. W. B.; Arockia Samy, N., Platinum(II) complexes of imidazophenanthroline-based polypyridine ligands as potential anticancer agents: synthesis, characterization, in vitro cytotoxicity studies and a comparative ab initio, and DFT studies with cisplatin, carboplatin, and oxaliplatin. *JBIC Journal of Biological Inorganic Chemistry* **2018,** *23*, (5), 833-848.

11. Moraleja, I.; Esteban-Fernández, D.; Lázaro, A.; Humanes, B.; Neumann, B.; Tejedor, A.; Mena, M. L.; Jakubowski, N.; Gómez-Gómez, M. M., Printing metal-spiked inks for LA-ICP-MS bioimaging internal standardization: comparison of the different nephrotoxic behavior of cisplatin, carboplatin, and oxaliplatin. *Analytical and Bioanalytical Chemistry* **2016,** *408*, (9), 2309-2318.

12. Ma, D.-L.; Chan, D. S.-H.; Leung, C.-H., Group 9 Organometallic Compounds for Therapeutic and Bioanalytical Applications. *Accounts of Chemical Research* **2014,** *47*, (12), 3614-3631.

13. Sarma, B. K.; Mugesh, G., Antioxidant activity of the anti-inflammatory compound ebselen: a reversible cyclization pathway via selenenic and seleninic acid intermediates. *Chemistry (Weinheim an der Bergstrasse, Germany)* **2008,** *14*, (34), 10603-14.

14. Azad, G. K.; Tomar, R. S., Ebselen, a promising antioxidant drug: mechanisms of action and targets of biological pathways. *Molecular biology reports* **2014,** *41*, (8), 4865-4879.

15. Sands, K. N.; Back, T. G., Key steps and intermediates in the catalytic mechanism for the reduction of peroxides by the antioxidant ebselen. *Tetrahedron* **2018**.

16. Fliedner, A.; Remde, A.; Niemann, R.; Schäfers, C.; Stein, B., Effects of the organotin pesticide azocyclotin in aquatic microcosms. *Chemosphere* **1997,** *35*, (1–2), 209-222.

17. de Carvalho Oliveira, R.; Santelli, R. E., Occurrence and chemical speciation analysis of organotin compounds in the environment: A review. *Talanta* **2010,** *82*, (1), 9-24.

18. Hoch, M., Organotin compounds in the environment — an overview. *Applied Geochemistry* **2001,** *16*, (7–8), 719-743.

19. Finnegan, C.; Ryan, D.; Enright, A.-M.; Garcia-Cabellos, G., A review of strategies for the detection and remediation of organotin pollution. *Critical Reviews in Environmental Science and Technology* **2018,** *48*, (1), 77-118.

20. Clasen, B.; Becker, A. G.; Lópes, T.; Murussi, C. R.; Antes, F. G.; Horn, R. C.; Flores, É. M. M.; Baldisserotto, B.; Dressler, V. L.; Loro, V. L., Triphenyltin hydroxide induces changes in the oxidative stress parameters of fish. *Ecotoxicology* **2017,** *26*, (4), 565-569.

21. Kumawat, N. K.; Dey, A.; Narasimhan, K. L.; Kabra, D., Near Infrared to Visible Electroluminescent Diodes Based on Organometallic Halide Perovskites: Structural and Optical Investigation. *ACS Photonics* **2015,** *2*, (3), 349-354.

22. Zhang, M.; Nomura, A.; Uchida, Y.; Iijima, H.; Sakamoto, T.; Iishii, Y.; Morishima, Y.; Mochizuki, M.; Masuyama, K.; Hirano, K.; Sekizawa, K., Ebselen

suppresses late airway responses and airway inflammation in guinea pigs. *Free Radical Biology and Medicine* **2002,** *32*, (5), 454-64.

23. Müller, A.; Cadenas, E.; Graf, P.; Sies, H., A novel biologically active seleno-organic compound--I. Glutathione peroxidase-like activity in vitro and antioxidant capacity of PZ 51 (Ebselen). *Biochemical pharmacology* **1984,** *33*, (20), 3235-9.
24. Prasad, N.; Ramteke, P.; Dholia, N.; Yadav, U. C. S., Chapter 27 - Therapeutic interventions to block oxidative stress-associated pathologies. In *Immunity and Inflammation in Health and Disease*, Chatterjee, S.; Jungraithmayr, W.; Bagchi, D., Eds. Academic Press: 2018; pp 341-362.
25. Bartolini, D.; Sancineto, L.; Fabro de Bem, A.; Tew, K. D.; Santi, C.; Radi, R.; Toquato, P.; Galli, F., Chapter Ten - Selenocompounds in cancer therapy: An overview. In *Advances in Cancer Research*, Tew, K. D.; Galli, F., Eds. Academic Press: 2017; Vol. 136, pp 259-302.
26. Thangamani, S.; Younis, W.; Seleem, M. N., Repurposing ebselen for treatment of multidrug-resistant staphylococcal infections. *Scientific Reports* **2015,** *5*, 11596.
27. Gustafsson, T. N.; Osman, H.; Werngren, J.; Hoffner, S.; Engman, L.; Holmgren, A., Ebselen and analogs as inhibitors of Bacillus anthracis thioredoxin reductase and bactericidal antibacterials targeting Bacillus species, Staphylococcus aureus and Mycobacterium tuberculosis. *Biochimica et Biophysica Acta (BBA)-General Subjects* **2016,** *1860*, (6), 1265-1271.
28. Sies, H.; Parnham, M. J., Potential therapeutic use of ebselen for COVID-19 and other respiratory viral infections. *Free Radical Biology and Medicine* **2020,** *156*, 107-112.

29. Menéndez, C. A.; Byléhn, F.; Perez-Lemus, G. R.; Alvarado, W.; de Pablo, J. J., Molecular characterization of ebselen binding activity to SARS-CoV-2 main protease. *Science advances* **2020,** *6*, (37), eabd0345.

30. Kumar, M.; Chhillar, B.; Yadav, M.; Sagar, P.; Singhal, N. K.; Gates, P. J.; Butcher, R. J.; Singh, V. P., Catalytic and highly regenerable aminic organoselenium antioxidants with cytoprotective effects. *Organic & Biomolecular Chemistry* **2021,** *19*, (9), 2015-2022.

31. Plateau, P.; Saveanu, C.; Lestini, R.; Dauplais, M.; Decourty, L.; Jacquier, A.; Blanquet, S.; Lazard, M., Exposure to selenomethionine causes selenocysteine misincorporation and protein aggregation in Saccharomyces cerevisiae. *Scientific Reports* **2017,** *7*, 44761.

32. Meotti, F. C.; Borges, V. C.; Zeni, G.; Rocha, J. B.; Nogueira, C. W., Potential renal and hepatic toxicity of diphenyl diselenide, diphenyl ditelluride and Ebselen for rats and mice. *Toxicol Lett* **2003,** *143*, (1), 9-16.

33. Mangiapane, E.; Pessione, A.; Pessione, E., Selenium and selenoproteins: an overview on different biological systems. *Curr Protein Pept Sci* **2014,** *15*, (6), 598-607.

34. Massé, A. J.; Muscatello, J. R.; Hogan, N. S.; Janz, D. M., Tissue-specific selenium accumulation and toxicity in adult female Xenopus laevis chronically exposed to elevated dietary selenomethionine. *Environmental Toxicology and Chemistry* **2017,** *36*, (4), 1047-1055.

35. Meotti, F. C.; Borges, V. C.; Zeni, G.; Rocha, J. B. T.; Nogueira, C. W., Potential renal and hepatic toxicity of diphenyl diselenide, diphenyl ditelluride and Ebselen for rats and mice. *Toxicology Letters* **2003,** *143*, (1), 9-16.

36. EPA Aquatic life ambient water quality criterion for selenium in freshwater. www.epa.gov/wqc/aquatic-life-criterion-selenium (August 8),

37. Simmons, D. B.; Wallschläger, D., A critical review of the biogeochemistry and ecotoxicology of selenium in lotic and lentic environments. *Environ Toxicol Chem* **2005,** *24*, (6), 1331-43.

38. Lemly, A. D., Aquatic selenium pollution is a global environmental safety issue. *Ecotoxicology and Environmental Safety* **2004,** *59*, (1), 44-56.

39. Brosillon, S.; Bancon-Montigny, C.; Mendret, J., Study of photocatalytic degradation of tributyltin, dibutylin and monobutyltin in water and marine sediments. *Chemosphere* **2014,** *109*, 173-179.

40. He, S.; Li, P.; Li, Z.-H., Review on endocrine disrupting toxicity of triphenyltin from the perspective of species evolution: Aquatic, amphibious and mammalian. *Chemosphere* **2021,** *269*, 128711.

41. Furdek, M.; Vahčič, M.; Ščančar, J.; Milačič, R.; Kniewald, G.; Mikac, N., Organotin compounds in seawater and Mytilus galloprovincialis mussels along the Croatian Adriatic Coast. *Marine pollution bulletin* **2012,** *64*, (2), 189-199.

42. Levine, K. E.; Young, D. J.; Afton, S. E.; Harrington, J. M.; Essader, A. S.; Weber, F. X.; Fernando, R. A.; Thayer, K.; Hatch, E. E.; Robinson, V. G., Development, validation, and application of an ultra-performance liquid chromatography–sector field inductively coupled plasma mass spectrometry method for simultaneous

determination of six organotin compounds in human serum. *Talanta* **2015,** *140*, 115-121.

43. Golub, M.; Doherty, J., Triphenyltin as a potential human endocrine disruptor. *Journal of toxicology and environmental health. Part B, Critical reviews* **2004,** *7*, (4), 281-95.

44. Sonak, S., Implications of organotins in the marine environment and their prohibition. *Journal of environmental management* **2009,** *90 Suppl 1*, S1-3.

45. Union, E., Regulation (EC) No 782/2003 of the European parliament and of the council of 14 April 2003 on the prohibition of organotin compounds on ships. *Off J Eur Union L* **2003,** *115*, 1-8.

46. Union, E., Communication from the Commission to the Council and the European Parliament - Community strategy for endocrine disrupters - A range of substances suspected of interfering with the hormone systems of humans and wildlife /* COM/99/0706 final */. **1999**.

47. Contaminant Candidate List (CCL) and Regulatory Determination (Chemical Contaminants - CCL 4). In EPA, Ed. 2016.

48. Shiraishi, H.; Soma, M., Triphenyltin compounds in mussels in Tokyo Bay after restriction of use in Japan. *Chemosphere* **1992,** *24*, (8), 1103-1109.

49. Reregistration Eligibility Decision (RED): Triphenyltin Hydroxide (TPTH). In EPA, Ed. National Service Center for Environmental Publications (NSCEP): 1999.

50. Veltman, K.; Huijbregts, M. A. J.; van den Heuvel-Greve, M. J.; Vethaak, A. D.; Hendriks, A. J., Organotin accumulation in an estuarine food chain: Comparing

field measurements with model estimations. *Marine Environmental Research* **2006,** *61*, (5), 511-530.

51. Blunden, S. J.; Chapman, A. H., The environmental degradation of organotin compounds — A review. *Environmental Technology Letters* **1982,** *3*, (1-11), 267-272.

52. Moran, M. A.; Zepp, R. G., Role of photoreactions in the formation of biologically labile compounds from dissolved organic matter. *Limnology and Oceanography* **1997,** *42*, (6), 1307-1316.

53. Hopanna, M.; Kelly, L.; Blaney, L., Photochemistry of the Organoselenium Compound Ebselen: Direct Photolysis and Reaction with Active Intermediates of Conventional Reactive Species Sensitizers and Quenchers. *Environmental Science & Technology* **2020**.

54. Schewe, T., Molecular actions of Ebselen—an antiinflammatory antioxidant. *General Pharmacology: The Vascular System* **1995,** *26*, (6), 1153-1169.

55. Jin, Z.; Du, X.; Xu, Y.; Deng, Y.; Liu, M.; Zhao, Y.; Zhang, B.; Li, X.; Zhang, L.; Peng, C.; Duan, Y.; Yu, J.; Wang, L.; Yang, K.; Liu, F.; Jiang, R.; Yang, X.; You, T.; Liu, X.; Yang, X.; Bai, F.; Liu, H.; Liu, X.; Guddat, L. W.; Xu, W.; Xiao, G.; Qin, C.; Shi, Z.; Jiang, H.; Rao, Z.; Yang, H., Structure of Mpro from SARS-CoV-2 and discovery of its inhibitors. *Nature* **2020,** *582*, (7811), 289-293.

56. Mishra, B.; Priyadarsini, K. I.; Mohan, H.; Mugesh, G., Horseradish peroxidase inhibition and antioxidant activity of ebselen and related organoselenium compounds. *Bioorganic & Medicinal Chemistry Letters* **2006,** *16*, (20), 5334-5338.

57. Masumoto, H.; Kissner, R.; Koppenol, W. H.; Sies, H., Kinetic study of the reaction of ebselen with peroxynitrite. *Federation of European Biochemical Societies Letters* **1996,** *398*, (2-3), 179-82.

58. Azad, G. K.; Balkrishna, S. J.; Sathish, N.; Kumar, S.; Tomar, R. S., Multifunctional ebselen drug functions through the activation of DNA damage response and alterations in nuclear proteins. *Biochemical Pharmacology* **2012,** *83*, (2), 296-303.

59. Miorelli, S. T.; Rosa, R. M.; Moura, D. J.; Rocha, J. C.; Carneiro Lobo, L. A.; Pêgas Henriques, J. A.; Saffi, J., Antioxidant and anti-mutagenic effects of ebselen in yeast and in cultured mammalian V79 cells. *Mutagenesis* **2008,** *23*, (2), 93-99.

60. Simmons, D. B. D.; Wallschla ger, D., A critical review of the biogeochemistry and ecotoxicology of selenium in lotic and lentic environments. *Environmental toxicology and chemistry* **2005,** *24 6*, 1331-43.

61. Lemly, A. D., Aquatic selenium pollution is a global environmental safety issue. *Ecotoxicology and environmental safety* **2004,** *59*, (1), 44-56.

62. Aquatic life ambient water quality criterion for selenium in freshwater. In Environmental Protection Agency, (EPA-HQ-OW-2004-0019); (www.epa.gov/wqc/aquatic-life-criterion-selenium): 2016.

63. Hopanna, M.; Mangalgiri, K.; Ibitoye, T.; Ocasio, D.; Snowberger, S.; Blaney, L., Chapter 8 - UV-254 transformation of antibiotics in water and wastewater treatment processes. In *Contaminants of Emerging Concern in Water and Wastewater*, Hernández-Maldonado, A. J.; Blaney, L., Eds. Butterworth-Heinemann: 2020; pp 239-297.

64. Chu, C.; Stamatelatos, D.; McNeill, K., Aquatic indirect photochemical transformations of natural peptidic thiols: impact of thiol properties, solution pH, solution salinity and metal ions. *Environmental Science: Processes & Impacts* **2017,** *19*, (12), 1518-1527.

65. Remucal, C. K., The role of indirect photochemical degradation in the environmental fate of pesticides: a review. *Environmental Science: Processes & Impacts* **2014,** *16*, (4), 628-653.

66. McConville, M. B.; Mezyk, S. P.; Remucal, C. K., Indirect photodegradation of the lampricides TFM and niclosamide. *Environmental Science: Processes & Impacts* **2017,** *19*, (8), 1028-1039.

67. Criado, S.; Bertolotti, S. G.; García, N. A., Kinetic aspects of the rose bengal-sensitized photo-oxygenation of tryptophan alkyl esters. Ground state and photopromoted dye-tryptophan derivative interactions. *Journal of Photochemistry and Photobiology B: Biology* **1996,** *34*, (1), 79-86.

68. Ludvikova, L.; Fris, P.; Heger, D.; Sebej, P.; Wirz, J.; Klan, P., Photochemistry of rose bengal in water and acetonitrile: a comprehensive kinetic analysis. *Physical chemistry chemical physics : PCCP* **2016,** *18*, (24), 16266-73.

69. Lee, P. C.; Rodgers, M. A., Laser flash photokinetic studies of rose bengal sensitized photodynamic interactions of nucleotides and DNA. *Photochemistry and photobiology* **1987,** *45*, (1), 79-86.

70. Stathis, A. A.; Hendrickson-Stives, A. K.; Kahan, T. F., Photolysis kinetics of toluene, ethylbenzene, and xylenes at ice surfaces. *The Journal of Physical Chemistry A* **2016,** *120*, (34), 6693-6697.

71. Davis, C. A.; Erickson, P. R.; McNeill, K.; Janssen, E. M. L., Environmental photochemistry of fenamate NSAIDs and their radical intermediates. *Environmental Science: Processes & Impacts* **2017,** *19*, (5), 656-665.

72. Neckers, D. C.; Jenks, W. S.; Wolff, T., *Advances in Photochemistry*. Wiley, 2007: Hoboken, N.J., 2007; Vol. 29.

73. Moor, K. J.; Schmitt, M.; Erickson, P. R.; McNeill, K., Sorbic acid as a triplet probe: Triplet energy and reactivity with triplet-state dissolved organic matter via $^1O_2$ phosphorescence. *Environmental Science & Technology* **2019,** *53*, (14), 8078-8086.

74. Packer, J. L.; Werner, J. J.; Latch, D. E.; McNeill, K.; Arnold, W. A., Photochemical fate of pharmaceuticals in the environment: Naproxen, diclofenac, clofibric acid, and ibuprofen. *Aquatic Sciences* **2003,** *65*, (4), 342-351.

75. Bolton, J. R.; Stefan, M. I.; Shaw, P.-S.; Lykke, K. R., Determination of the quantum yields of the potassium ferrioxalate and potassium iodide–iodate actinometers and a method for the calibration of radiometer detectors. *Journal of Photochemistry and Photobiology A: Chemistry* **2011,** *222*, (1), 166-169.

76. Appiani, E.; Ossola, R.; Latch, D. E.; Erickson, P. R.; McNeill, K., Aqueous singlet oxygen reaction kinetics of furfuryl alcohol: effect of temperature, pH, and salt content. *Environmental Science: Processes & Impacts* **2017,** *19*, (4), 507-516.

77. Gligorovski, S.; Strekowski, R.; Barbati, S.; Vione, D., Environmental implications of hydroxyl radicals (• OH). *Chemical Reviews* **2015,** *115*, (24), 13051-13092.

78. Masumoto, H.; Sies, H., The reaction of ebselen with peroxynitrite. *Chemical research in toxicology* **1996,** *9*, (1), 262-7.

79. Haenen, G. R.; De Rooij, B. M.; Vermeulen, N. P.; Bast, A., Mechanism of the reaction of ebselen with endogenous thiols: dihydrolipoate is a better cofactor than glutathione in the peroxidase activity of ebselen. *Molecular pharmacology* **1990,** *37*, (3), 412-22.

80. Pi, Y.; Schumacher, J.; Jekel, M., Decomposition of aqueous ozone in the presence of aromatic organic solutes. *Water Research* **2005,** *39*, (1), 83-88.

81. Pi, Y.; Schumacher, J.; Jekel, M., The use of *para*-chlorobenzoic acid (*p*CBA) as an ozone/hydroxyl radical probe compound. *Ozone: Science & Engineering* **2005,** *27*, (6), 431-436.

82. ChemAxon https://chemicalize.com/ (February 20, 2018),

83. Sheraz, M. A.; Kazi, S. H.; Ahmed, S.; Mirza, T.; Ahmad, I.; Evstigneev, M. P., Effect of phosphate buffer on the complexation and photochemical interaction of riboflavin and caffeine in aqueous solution: A kinetic study. *Journal of Photochemistry and Photobiology A: Chemistry* **2014,** *273*, 17-22.

84. Ahmad, I.; Fasihullah, Q.; Vaid, F. H. M., Effect of phosphate buffer on photodegradation reactions of riboflavin in aqueous solution. *Journal of Photochemistry and Photobiology B: Biology* **2005,** *78*, (3), 229-234.

85. Di Mascio, P.; Martinez, G. R.; Miyamoto, S.; Ronsein, G. E.; Medeiros, M. H. G.; Cadet, J., Singlet molecular oxygen reactions with nucleic acids, lipids, and proteins. *Chemical Reviews* **2019,** *119*, (3), 2043-2086.

86. Rogers, J. E.; Kelly, L. A., Nucleic acid oxidation mediated by naphthalene and benzophenone imide and diimide derivatives: consequences for DNA redox chemistry. *Journal of the American Chemical Society* **1999,** *121*, (16), 3854-3861.

87. Abraham, B.; McMasters, S.; Mullan, M. A.; Kelly, L. A., Reactivities of carboxyalkyl-substituted 1,4,5,8-naphthalene diimides in aqueous solution. *Journal of the American Chemical Society* **2004,** *126*, (13), 4293-4300.

88. Apell, J. N.; Pflug, N. C.; McNeill, K., Photodegradation of fludioxonil and other pyrroles: the importance of indirect photodegradation for understanding environmental fate and photoproduct formation. *Environmental Science & Technology* **2019,** *53*, (19), 11240-11250.

89. Harbour, J. R.; Issler, S. L., Involvement of the azide radical in the quenching of singlet oxygen by azide anion in water. *Journal of the American Chemical Society* **1982,** *104*, (3), 903-905.

90. Allen, M. T.; Lynch, M.; Lagos, A.; Redmond, R. W.; Kochevar, I. E., A wavelength dependent mechanism for rose bengal-sensitized photoinhibition of red cell acetylcholinesterase. *Biochimica et Biophysica Acta (BBA) - General Subjects* **1991,** *1075*, (1), 42-49.

91. McNeill, K.; Canonica, S., Triplet state dissolved organic matter in aquatic photochemistry: reaction mechanisms, substrate scope, and photophysical properties. *Environmental science: processes & impacts* **2016,** *18*, (11), 1381-1399.

92. Schöneich, C.; Narayanaswami, V.; Asmus, K.-D.; Sies, H., Reactivity of ebselen and related selenoorganic compounds with 1, 2-dichloroethane radical cations and halogenated peroxyl radicals. *Archives of biochemistry and biophysics* **1990,** *282*, (1), 18-25.

93. Dell'Arciprete, M. L.; Santos-Juanes, L.; Arques, A.; Vercher, R. F.; Amat, A. M.; Furlong, J. P.; Mártire, D. O.; Gonzalez, M. C., Reactivity of neonicotinoid pesticides with singlet oxygen. *Catalysis Today* **2010,** *151*, (1), 137-142.

94. Wang, J. F.; Komarov, P.; Sies, H.; de Groot, H., Inhibition of superoxide and nitric oxide release and protection from reoxygenation injury by Ebselen in rat Kupffer cells. *Hepatology* **1992,** *15*, (6), 1112-1116.

95. Araki, T.; Kitaoka, H., The mechanism of reaction of ebselen with superoxide in aprotic solvents as examined by cyclic voltammetry and ESR. *Chemical and pharmaceutical bulletin* **2001,** *49*, (5), 541-545.

96. Van Hemmen, J. J.; Meuling, W. J. A., Inactivation of biologically active DNA by γ-ray-induced superoxide radicals and their dismutation products singlet molecular oxygen and hydrogen peroxide. *Biochimica et Biophysica Acta (BBA) - Nucleic Acids and Protein Synthesis* **1975,** *402*, (2), 133-141.

97. Samuel, E. L. G.; Marcano, D. C.; Berka, V.; Bitner, B. R.; Wu, G.; Potter, A.; Fabian, R. H.; Pautler, R. G.; Kent, T. A.; Tsai, A.-L.; Tour, J. M., Highly efficient conversion of superoxide to oxygen using hydrophilic carbon clusters. *Proc Natl Acad Sci U S A* **2015,** *112*, (8), 2343-2348.

98. Chen, Y.; Zhang, X.; Feng, S., Contribution of the excited triplet state of humic acid and superoxide radical anion to generation and elimination of phenoxyl radical. *Environmental Science & Technology* **2018,** *52*, (15), 8283-8291.

99. Kamrul, H. S. M.; Schiraldi, A.; Cosio, M. S.; Scampicchio, M., Food and ascorbic scavengers of hydrogen peroxide. *Journal of Thermal Analysis and Calorimetry* **2016,** *125*, (2), 729-737.

100. Rochelle, G. T.; Owens, D. R.; Chang, J. C. S.; Bma, T. G., Thiosulfate as an oxidation inhibitor in flue gas desulfurization processes: a review of R&D results. *Journal of the Air Pollution Control Association* **1986,** *36*, (10), 1138-1146.

101. Miura, T.; Muraoka, S.; Fujimoto, Y., Lipid peroxidation induced by indomethacin with horseradish peroxidase and hydrogen peroxide: involvement of indomethacin radicals. *Biochemical Pharmacology* **2002,** *63*, (11), 2069-2074.

102. Rodríguez-López, J. N.; Lowe, D. J.; Hernández-Ruiz, J.; Hiner, A. N. P.; García-Cánovas, F.; Thorneley, R. N. F., Mechanism of reaction of hydrogen peroxide with horseradish peroxidase: identification of intermediates in the catalytic cycle. *Journal of the American Chemical Society* **2001,** *123*, (48), 11838-11847.

103. Long, L. H.; Halliwell, B., Artefacts in cell culture: Pyruvate as a scavenger of hydrogen peroxide generated by ascorbate or epigallocatechin gallate in cell culture media. *Biochemical and Biophysical Research Communications* **2009,** *388*, (4), 700-704.

104. Schöne, L.; Herrmann, H., Kinetic measurements on the reactivity of hydrogen peroxide and ozone towards small atmospherically relevant aldehydes, ketones and organic acids in aqueous solution. *Atmospheric Chemistry & Physics Discussions* **2013,** *13*, 25537-25566.

105. Maiorino, M.; Roveri, A.; Coassin, M.; Ursini, F., Kinetic mechanism and substrate specificity of glutathione peroxidase activity of ebselen (PZ51). *Biochemical Pharmacology* **1988,** *37*, (11), 2267-71.

106. Morgenstern, R.; Cotgreave, I. A.; Engman, L., Determination of the relative contributions of the diselenide and selenol forms of ebselen in the mechanism of its

glutathione peroxidase-like activity. *Chemico-Biological Interactions* **1992,** *84*, (1), 77-84.

107. Sies, H., Ebselen, a selenoorganic compound as glutathione peroxidase mimic. *Free Radical Biology and Medicine* **1993,** *14*, (3), 313-323.
108. Grebel, J. E.; Pignatello, J. J.; Mitch, W. A., Sorbic acid as a quantitative probe for the formation, scavenging and steady-state concentrations of the triplet-excited state of organic compounds. *Water Research* **2011,** *45*, (19), 6535-6544.
109. Schwack, W.; Bourgeois, B.; Walker, F., Fungicides and photochemistry photodegradation of the dicarboximide fungicide procymidone. *Chemosphere* **1995,** *31*, (9), 4033-4040.
110. Roberts, J. E.; Wishart, J. F.; Martinez, L.; Chignell, C. F., Photochemical Studies on Xanthurenic Acid¶. *Photochemistry and photobiology* **2000,** *72*, (4), 467-471.
111. Huang, L.; St Denis, T. G.; Xuan, Y.; Huang, Y.-Y.; Tanaka, M.; Zadlo, A.; Sarna, T.; Hamblin, M. R., Paradoxical potentiation of methylene blue-mediated antimicrobial photodynamic inactivation by sodium azide: role of ambient oxygen and azide radicals. *Free radical biology & medicine* **2012,** *53*, (11), 2062-2071.
112. Kasimova, K. R.; Sadasivam, M.; Landi, G.; Sarna, T.; Hamblin, M. R., Potentiation of photoinactivation of Gram-positive and Gram-negative bacteria mediated by six phenothiazinium dyes by addition of azide ion. *Photochemical and Photobiological Sciences* **2014,** *13*, (11), 1541-8.
113. Nobumasa, K.; Hirokazu, I.; Akira, I.; Michio, K., Photochemical Reaction of 2-Aryl-1,2-benzisoselenazol-3(2H)-ones. *Bulletin of the Chemical Society of Japan* **1986,** *59*, (7), 2179-2183.

114. Chen, S.; Blaney, L.; Chen, P.; Deng, S.; Hopanna, M.; Bao, Y.; Yu, G., Ozonation of the 5-fluorouracil anticancer drug and its prodrug capecitabine: Reaction kinetics, oxidation mechanisms, and residual toxicity. *Frontiers of Environmental Science & Engineering* **2019,** *13*, (4), 59.

115. Hu, J.; Zhang, Z.; Wei, Q.; Zhen, H.; Zhao, Y.; Peng, H.; Wan, Y.; Giesy, J. P.; Li, L.; Zhang, B., Malformations of the endangered Chinese sturgeon, Acipenser sinensis, and its causal agent. *Proceedings of the National Academy of Sciences* **2009,** *106*, (23), 9339-9344.

116. Mahanty, S.; Raghav, D.; Rathinasamy, K., In vitro evaluation of the cytotoxic and bactericidal mechanism of the commonly used pesticide triphenyltin hydroxide. *Chemosphere* **2017,** *183*, 339-352.

117. Yi, A. X.; Leung, K. M.; Lam, M. H.; Lee, J. S.; Giesy, J. P., Review of measured concentrations of triphenyltin compounds in marine ecosystems and meta-analysis of their risks to humans and the environment. *Chemosphere* **2012,** *89*, (9), 1015-25.

118. Saurina, J.; Leal, C.; Compañó, R.; Granados, M.; Tauler, R.; Prat, M. D., Determination of triphenyltin in sea-water by excitation–emission matrix fluorescence and multivariate curve resolution. *Analytica Chimica Acta* **2000,** *409*, (1), 237-245.

119. Batista-Andrade, J. A.; Caldas, S. S.; Batista, R. M.; Castro, I. B.; Fillmann, G.; Primel, E. G., From TBT to booster biocides: Levels and impacts of antifouling along coastal areas of Panama. *Environmental Pollution* **2018,** *234*, 243-252.

120. U.S. Environmental Protection Agency, R.E.D. FACTS: triphenyltin hydroxide(TPTH). In 738-R-99-010, E., Ed. Office of Prevention, Pesticides and Toxic Substances: 1999.

121. Rantakokko, P.; Hallikainen, A.; Airaksinen, R.; Vuorinen, P. J.; Lappalainen, A.; Mannio, J.; Vartiainen, T., Concentrations of organotin compounds in various fish species in the Finnish lake waters and Finnish coast of the Baltic Sea. *Science of the total environment* **2010,** *408*, (12), 2474-2481.

122. Hu, J.; Zhen, H.; Wan, Y.; Gao, J.; An, W.; An, L.; Jin, F.; Jin, X., Trophic magnification of triphenyltin in a marine food web of Bohai Bay, North China: Comparison to tributyltin. *Environmental science & technology* **2006,** *40*, (10), 3142-3147.

123. Gao, J.-M.; Wu, L.; Chen, Y.-P.; Zhou, B.; Guo, J.-S.; Zhang, K.; Ouyang, W.-J., Spatiotemporal distribution and risk assessment of organotins in the surface water of the Three Gorges Reservoir Region, China. *Chemosphere* **2017,** *171*, 405-414.

124. Harino, H.; Yamamoto, Y.; Eguchi, S.; Kawai, S. c.; Kurokawa, Y.; Arai, T.; Ohji, M.; Okamura, H.; Miyazaki, N., Concentrations of Antifouling Biocides in Sediment and Mussel Samples Collected from Otsuchi Bay, Japan. *Archives of Environmental Contamination and Toxicology* **2006,** *52*, (2), 179.

125. Midorikawa, S.; Arai, T.; Harino, H.; Ohji, M.; Duc Cu, N.; Miyazaki, N., Concentrations of organotin compounds in sediment and clams collected from coastal areas in Vietnam. *Environmental Pollution* **2004,** *131*, (3), 401-408.

126. Murai, R.; Sugimoto, A.; Tanabe, S.; Takeuchi, I., Biomagnification profiles of tributyltin (TBT) and triphenyltin (TPT) in Japanese coastal food webs elucidated by stable nitrogen isotope ratios. *Chemosphere* **2008,** *73*, (11), 1749-1756.

127. Chen, C.; Chen, L.; Huang, Q.; Chen, Z.; Zhang, W., Organotin contamination in commercial and wild oysters from China: Increasing occurrence of triphenyltin. *Science of The Total Environment* **2019,** *650*, 2527-2534.

128. Xiao, Y.; Jiang, J.; Hu, W.; Zhao, Y.; Hu, J., Toxicity of triphenyltin on the development of retinal axons in zebrafish at low dose. *Aquatic Toxicology* **2017,** *189*, 9-15.

129. Schulte-Oehlmann, U.; Tillmann, M.; Markert, B.; Oehlmann, J.; Watermann, B.; Scherf, S., Effects of Endocrine Disruptors on Prosobranch Snails (Mollusca: Gastropoda) in the Laboratory. Part II: Triphenyltin as a Xeno-Androgen. *Ecotoxicology* **2000,** *9*, (6), 399-412.

130. Yuan, J.; Zhang, X.; Yu, L.; Sun, Z.; Zhu, P.; Wang, X.; Shi, H., Stage-specific malformations and phenotypic changes induced in embryos of amphibian (Xenopus tropicalis) by triphenyltin. *Ecotoxicology and environmental safety* **2011,** *74*, (7), 1960-1966.

131. Yi, A. X.; Han, J.; Lee, J.-S.; Leung, K. M. Y., Ecotoxicity of triphenyltin on the marine copepod Tigriopus japonicus at various biological organisations: from molecular to population-level effects. *Ecotoxicology* **2014,** *23*, (7), 1314-1325.

132. Arnold, C. G.; Weidenhaupt, A.; David, M. M.; Müller, S. R.; Haderlein, S. B.; Schwarzenbach, R. P., Aqueous Speciation and 1-Octanol−Water Partitioning of

Tributyl- and Triphenyltin: Effect of pH and Ion Composition. *Environmental Science & Technology* **1997,** *31*, (9), 2596-2602.

133. Barnes, R. D.; Bull, A. T.; Poller, R. C., Studies on the persistence of the organotin fungicide fentin acetate (triphenyltin acetate) in the soil and on surfaces exposed to light. *Pesticide Science* **1973,** *4*, (3), 305-317.
134. Ye, J.; Yin, H.; Peng, H.; Bai, J.; Xie, D.; Wang, L., Biosorption and biodegradation of triphenyltin by Brevibacillus brevis. *Bioresource Technology* **2013,** *129*, 236-241.
135. Soderquist, C. J.; Crosby, D. G., Degradation of triphenyltin hydroxide in water. *Journal of Agricultural and Food Chemistry* **1980,** *28*, (1), 111-117.
136. Blunden, S.; Chapman, A., The environmental degradation of organotin compounds—a review. *Environmental Technology* **1982,** *3*, (1-11), 267-272.
137. Antes, F. G.; Krupp, E.; Flores, E. M. M.; Dressler, V. L.; Feldmann, J., Speciation and Degradation of Triphenyltin in Typical Paddy Fields and Its Uptake into Rice Plants. *Environmental Science & Technology* **2011,** *45*, (24), 10524-10530.
138. Cai, Y.; Apell, J. N.; Pflug, N. C.; McNeill, K.; Bollmann, U. E., Photochemical fate of medetomidine in coastal and marine environments. *Water Research* **2021,** *191*, 116791.
139. Wasswa, J.; Driscoll, C. T.; Zeng, T., Photochemical characterization of surface waters from lakes in the adirondack region of New York. *Environmental science & technology* **2020,** *54*, (17), 10654-10667.
140. Carena, L.; Puscasu, C. G.; Comis, S.; Sarakha, M.; Vione, D., Environmental photodegradation of emerging contaminants: A re-examination of the importance of

triplet-sensitised processes, based on the use of 4-carboxybenzophenone as proxy for the chromophoric dissolved organic matter. *Chemosphere* **2019,** *237*, 124476.

141. Mamatha Hopanna, K. H., Carsten Prasse, and Lee Blaney Photochemical fate of triphenyltin pesticides in engineered water systems: Reaction kinetics, transformation products, and residual toxicity. *Water Research* **2021**.
142. Rogers, J. E.; Kelly, L. A., Nucleic acid oxidation mediated by naphthalene and benzophenone imide and diimide derivatives: consequences for DNA redox chemistry. *Journal of the American Chemical Society* **1999,** *121*, (16), 3854-3861.
143. De Laurentiis, E.; Prasse, C.; Ternes, T. A.; Minella, M.; Maurino, V.; Minero, C.; Sarakha, M.; Brigante, M.; Vione, D., Assessing the photochemical transformation pathways of acetaminophen relevant to surface waters: Transformation kinetics, intermediates, and modelling. *Water Research* **2014,** *53*, 235-248.
144. Bodrato, M.; Vione, D., APEX (Aqueous Photochemistry of Environmentally occurring Xenobiotics): a free software tool to predict the kinetics of photochemical processes in surface waters. *Environmental Science: Processes & Impacts* **2014,** *16*, (4), 732-740.
145. Marchetti, G.; Minella, M.; Maurino, V.; Minero, C.; Vione, D., Photochemical transformation of atrazine and formation of photointermediates under conditions relevant to sunlit surface waters: laboratory measures and modelling. *Water Res* **2013,** *47*, (16), 6211-22.
146. Fabbri, D.; Minella, M.; Maurino, V.; Minero, C.; Vione, D., Photochemical transformation of phenylurea herbicides in surface waters: A model assessment of

persistence, and implications for the possible generation of hazardous intermediates. *Chemosphere* **2015,** *119*, 601-607.

147. Vione, D.; Maddigapu, P. R.; De Laurentiis, E.; Minella, M.; Pazzi, M.; Maurino, V.; Minero, C.; Kouras, S.; Richard, C., Modelling the photochemical fate of ibuprofen in surface waters. *Water Research* **2011,** *45*, (20), 6725-6736.
148. Photochemical Fate of Amicarbazone in Aqueous Media: Laboratory Measurement and Simulations. *Environmental Engineering Science* **2015,** *32*, (8), 730-740.
149. Zhou, H.; Yan, S.; Lian, L.; Song, W., Triplet-state photochemistry of dissolved organic matter: triplet-state energy distribution and surface electric charge conditions. *Environmental Science & Technology* **2019,** *53*, (5), 2482-2490.
150. Gerecke, A. C.; Canonica, S.; Müller, S. R.; Schärer, M.; Schwarzenbach, R. P., Quantification of Dissolved Natural Organic Matter (DOM) Mediated Phototransformation of Phenylurea Herbicides in Lakes. *Environmental Science & Technology* **2001,** *35*, (19), 3915-3923.
151. Janssen, E. M.; Marron, E.; McNeill, K., Aquatic photochemical kinetics of benzotriazole and structurally related compounds. *Environmental Science: Processes & Impacts* **2015,** *17*, (5), 939-946.
152. Wojnárovits, L.; Takács, E., Rate coefficients of hydroxyl radical reactions with pesticide molecules and related compounds: A review. *Radiation Physics and Chemistry* **2014,** *96*, 120-134.
153. Vione, D.; Falletti, G.; Maurino, V.; Minero, C.; Pelizzetti, E.; Malandrino, M.; Ajassa, R.; Olariu, R.-I.; Arsene, C., Sources and sinks of hydroxyl radicals upon

irradiation of natural water samples. *Environmental science & technology* **2006,** *40*, (12), 3775-3781.

154. Minella, M.; Rapa, L.; Carena, L.; Pazzi, M.; Maurino, V.; Minero, C.; Brigante, M.; Vione, D., An experimental methodology to measure the reaction rate constants of processes sensitised by the triplet state of 4-carboxybenzophenone as a proxy of the triplet states of chromophoric dissolved organic matter, under steady-state irradiation conditions. *Environmental science: processes & impacts* **2018,** *20*, (7), 1007-1019.
155. Wenk, J.; Eustis, S. N.; McNeill, K.; Canonica, S., Quenching of Excited Triplet States by Dissolved Natural Organic Matter. *Environmental Science & Technology* **2013,** *47*, (22), 12802-12810.
156. Cory, R. M.; McKnight, D. M., Fluorescence spectroscopy reveals ubiquitous presence of oxidized and reduced quinones in dissolved organic matter. *Environmental science & technology* **2005,** *39*, (21), 8142-8149.
157. Maddigapu, P. R.; Bedini, A.; Minero, C.; Maurino, V.; Vione, D.; Brigante, M.; Mailhot, G.; Sarakha, M., The pH-dependent photochemistry of anthraquinone-2-sulfonate. *Photochemical & Photobiological Sciences* **2010,** *9*, (3), 323-330.
158. Avetta, P.; Fabbri, D.; Minella, M.; Brigante, M.; Maurino, V.; Minero, C.; Pazzi, M.; Vione, D., Assessing the phototransformation of diclofenac, clofibric acid and naproxen in surface waters: Model predictions and comparison with field data. *Water Research* **2016,** *105*, 383-394.

159. Burrows, H. D.; Santaballa, J.; Steenken, S., Reaction pathways and mechanisms of photodegradation of pesticides. *Journal of photochemistry and photobiology B: Biology* **2002,** *67*, (2), 71-108.

160. Gornik, T.; Carena, L.; Kosjek, T.; Vione, D., Phototransformation study of the antidepressant paroxetine in surface waters. *Science of The Total Environment* **2021,** *774*, 145380.

161. Dalrymple, R. M.; Carfagno, A. K.; Sharpless, C. M., Correlations between dissolved organic matter optical properties and quantum yields of singlet oxygen and hydrogen peroxide. *Environmental Science & Technology* **2010,** *44*, (15), 5824-5829.

162. McKay, G.; Huang, W.; Romera-Castillo, C.; Crouch, J. E.; Rosario-Ortiz, F. L.; Jaffé, R., Predicting reactive intermediate quantum yields from dissolved organic matter photolysis using optical properties and antioxidant capacity. *Environmental Science & Technology* **2017,** *51*, (10), 5404-5413.

163. Partanen, S. B.; Erickson, P. R.; Latch, D. E.; Moor, K. J.; McNeill, K., Dissolved Organic Matter Singlet Oxygen Quantum Yields: Evaluation Using Time-Resolved Singlet Oxygen Phosphorescence. *Environmental Science & Technology* **2020,** *54*, (6), 3316-3324.

164. Carena, L.; Vione, D., Modelling the photochemistry of imazethapyr in rice paddy water. *Science of The Total Environment* **2018,** *644*, 1391-1398.

165. Arnold, C. G.; Weidenhaupt, A.; David, M. M.; Müller, S. R.; Haderlein, S. B.; Schwarzenbach, R. P., Aqueous speciation and 1-octanol− water partitioning of

tributyl-and triphenyltin: effect of pH and ion composition. *Environmental science & technology* **1997,** *31*, (9), 2596-2602.

166. Harbison, R. D.; Johnson, D. R., Tin. *Hamilton & Hardy's Industrial Toxicology* **2015**, 247-252.
167. Navio, J. A.; Cerrillos, C.; Marchena, F. J.; Pablos, F.; Pradera, M. A., Photoassisted degradation of n-butyltin chlorides in air-equilibrated aqueous TiO2 suspension. *Langmuir* **1996,** *12*, (8), 2007-2014.
168. Horie, Y.; Watanabe, H.; Takanobu, H.; Shigemoto, Y.; Yamagishi, T.; Iguchi, T.; Tatarazako, N., Effects of triphenyltin on reproduction in Japanese medaka (Oryzias latipes) across two generations. *Aquatic Toxicology* **2017,** *192*, 16-23.
169. Kannan, K.; Lee, R. F., Triphenyltin and its degradation products in foliage and soils from sprayed pecan orchards and in fish from adjacent ponds. *Environmental Toxicology and Chemistry* **1996,** *15*, (9), 1492-1499.
170. Navio, J. A.; Cerrillos, C.; Pradera, M. A.; Morales, E.; Gómez-Ariza, J. L., UV-photoassisted degradation of phenyltin(IV) chlorides in water. *Journal of Photochemistry and Photobiology A: Chemistry* **1997,** *108*, (1), 59-63.
171. Palm, W. U.; Kopetzky, R.; Ruck, W., OH-radical reactivity and direct photolysis of triphenyltin hydroxide in aqueous solution. *Journal of Photochemistry and Photobiology A: Chemistry* **2003,** *156*, (1), 105-114.
172. Shu, Z.; Bolton, J. R.; Belosevic, M.; El Din, M. G., Photodegradation of emerging micropollutants using the medium-pressure UV/H2O2 advanced oxidation process. *Water Research* **2013,** *47*, (8), 2881-2889.

173. Snowberger, S.; Adejumo, H.; He, K.; Mangalgiri, K. P.; Hopanna, M.; Soares, A. D.; Blaney, L., Direct Photolysis of Fluoroquinolone Antibiotics at 253.7 nm: Specific Reaction Kinetics and Formation of Equally Potent Fluoroquinolone Antibiotics. *Environmental Science & Technology* **2016,** *50*, (17), 9533-9542.
174. Lin, H.; Pang, K.; Ma, Y.; Hu, J., Photodegradation of fluazaindolizine in water under simulated sunlight irradiation: Identification of transformation products and elucidation of transformation mechanism. *Chemosphere* **2019,** *214*, 543-552.
175. Zhang, Y.-n.; Zhao, J.; Zhou, Y.; Qu, J.; Chen, J.; Li, C.; Qin, W.; Zhao, Y.; Peijnenburg, W. J. G. M., Combined effects of dissolved organic matter, pH, ionic strength and halides on photodegradation of oxytetracycline in simulated estuarine waters. *Environmental Science: Processes & Impacts* **2019,** *21*, (1), 155-162.
176. Li, Y.; Qiao, X.; Zhang, Y.-n.; Zhou, C.; Xie, H.; Chen, J., Effects of halide ions on photodegradation of sulfonamide antibiotics: Formation of halogenated intermediates. *Water Research* **2016,** *102*, 405-412.
177. Ahmed, S.; Mustaan, N.; Sheraz, M. A.; Nabi, S. A. A. U.; Ahmad, I., Validation of a UV Spectrometric Method for the Assay of Tolfenamic Acid in Organic Solvents. *J Pharm (Cairo)* **2015,** *2015*, 216249-216249.
178. Al Mohaimeed, R. M.; Ansari, A. A.; Aldwayyan, A., The Role of Solvent Environment on the Optical Behavior of Chemically Synthesized Silicon Nanoparticles. *Journal of Spectroscopy* **2018,** *2018*, 6870645.
179. Sero, R.; Vidal, M.; Bosch, J.; Rodríguez, P.; Galceran, M.; Moyano, E., Desorption electrospray ionization-high resolution mass spectrometry for the analysis of unknown materials: The phytosanitary product case. *Talanta* **2019,** *194*, 350-356.

180. Liu, Y.; He, X.; Fu, Y.; Dionysiou, D. D., Degradation kinetics and mechanism of oxytetracycline by hydroxyl radical-based advanced oxidation processes. *Chemical Engineering Journal* **2016,** *284*, 1317-1327.

181. Sharpless, C. M.; Linden, K. G., Experimental and model comparisons of low- and medium-pressure Hg lamps for the direct and H2O2 assisted UV photodegradation of N-nitrosodimethylamine in simulated drinking water. *Environmental Science & Technology* **2003,** *37*, (9), 1933-1940.

182. Gligorovski, S.; Strekowski, R.; Barbati, S.; Vione, D., Environmental implications of hydroxyl radicals (•OH). *Chemical Reviews* **2015,** *115*, (24), 13051-13092.

183. Erickson, P. R.; Moor, K. J.; Werner, J. J.; Latch, D. E.; Arnold, W. A.; McNeill, K., Singlet oxygen phosphorescence as a probe for triplet-state dissolved organic matter reactivity. *Environmental Science & Technology* **2018,** *52*, (16), 9170-9178.